DEVELOPMENT OF WIDE-BAND GAP InGaN SOLAR CELLS FOR HIGH-EFFICIENCY PHOTOVOLTAICS

A Dissertation
Presented to
The Academic Faculty

By

Omkar K. Jani

In Partial Fulfillment
Of the Requirements for the Degree
Doctor of Philosophy in the
School of Electrical and Computer Engineering

Georgia Institute of Technology
August, 2008

DEVELOPMENT OF WIDE-BAND GAP InGaN SOLAR CELLS FOR HIGH-EFFICIENCY PHOTOVOLTAICS

Approved by:

Dr. Christiana B. Honsberg, Advisor
Electrical and Computer Engineering
University of Delaware

Dr. Ian T. Ferguson, Co-advisor
Electrical and Computer Engineering
Georgia Institute of Technology

Dr. Ajeet Rohatgi
Electrical and Computer Engineering
Georgia Institute of Technology

Dr. David S. Citrin
Electrical and Computer Engineering
Georgia Institute of Technology

Dr. Benjamin D. B. Klein
Electrical and Computer Engineering
Georgia Institute of Technology

Dr. Robert L. Snyder
Material Science and Engineering
Georgia Institute of Technology

Date Approved: April 28, 2008

To my father, Kujad,

for his love, support and sacrifices…

ACKNOWLEDGEMENTS

I am deeply grateful to my advisor, Prof. Christiana Honsberg, for her invaluable academic guidance and keen support. I am also grateful to my co-advisor, Prof. Ian Ferguson, for his accommodation and especially, his administrative guidance.

I would like to thank the members of the Solid State Lighting group at Georgia Tech including Dr. Hongbo Yu, Dr. Vincent Woods, Dr. Shenjie Wang, Shalini Gupta, Nola Li, Will Fenwick, Tahir Zaidi, and Andrew Melton; and the past members including Ali Asghar, Dr. June O Song, Dr. Hun Kang, Dr. David Nicol, Dr. Matthew Kane, Dr. Adam Payne, and Yong Huang for their strong team-support. I also appreciate the help from members of the Solar Power Center at the University of Delaware, including Prof. Allen Barnett, Dr. Nikolai Faleev for his insight on crystalline perfection, Mohit Mehta for his modifications on the PC1D source code, Balakrishnam Jampana for help with fabrication, and Michael 'Qbear' Levy for the constructive arguments on various technical issues. I am grateful to Dr. Stuart Bowden of the Institute of Energy Conversion (IEC) for his insight on technical and commercial aspects of photovoltaics.

I would like to thank Dr. Alan Doolittle for his technical insight, and Elaissa Trybus and Walter Henderson for their hands-on support. I would also like to thank Dr. Ajeet Rohatgi, Dr. Dongseop Kim, Dr. Abasifreki Ebong, Dr. Vijay Yelundur, Manav Sheoran, Ajay Upadhyaya and Alan Ristow of the University Center for Excellence in Photovoltaic Research and Education (UCEP) at Georgia Tech for my initial education in silicon

photovoltaics and their support. The discussions with Dr. David Citrin and Dr. Jing Bai have been extremely helpful in confirming and modeling optical data. The staff at the Microelectronic Research Center (MiRC) including Gary Spinner, Charlie Suh and Brandon Harrington has been extremely helpful with their facility and prompt technical support for cleanroom processing and solar cell fabrication.

This research was partially funded by DARPA/ARO Agreement No.: W911NF-05-9-0005 monitored by Dr. Douglas Kirkpatrick. This work was also supported by U.S. D.O.E., the National Renewable Energy Laboratories, monitored by Dr. Robert McConnell and Dr. Martha Symko-Davies, and the Office of Naval Research, monitored by Dr. Colin Wood. I would also like to acknowledge Dr. Sarah Kurtz, Dr. Tom Moriarty and Dr. Miles Steiner for their help with device characterization.

I am deeply grateful to my family, especially my wife, Kinjal, and father, Kujad; Bapuji, Mudra and Manish for their patience and undeviating emotional support. Support from my roommates – Vishal (Papad), Rahul (Baja), Paras (Chinka), Gurashish (Ramu), Prashant (Sukkhad), Saurav (Lalaji), Rohan (Dude), and Vikrant (Tau), especially in preparing tea to keep me up during late hours has been invaluable. Finally, I am honored to be imparted the physical and mental strength, and the realization "Winners never quit, quitters never win", which has kept me focused on my work over the past couple of years, by Renshi Michael Mobley and the Avengers Dantai.

TABLE OF CONTENTS

LIST OF TABLES

LIST OF FIGURES

LIST OF SYMBOLS and ABBREVIATIONS

(Symbol)	(Unit)	(Description)
α	cm^{-1}	absorption coefficient
α_o	$(eV^{1/2})/cm$	absorption coefficient fitting parameter
ε	-	strain
ε_x	-	strain in direction of basal a-plane of wurtzite crystal
ε_z	-	strain perpendicular to basal a-plane of wurtzite crystal
η	%	efficiency
λ	μm, nm	wavelength
μ	$cm^2/V\bullet s$	mobility of electron or hole
σ_P	C/m^2	polarization-induced charge density
τ	s, ms, μs, ns	minority carrier lifetime
Φ	eV	work-function
φ_n	V	electron quasi-fermi potential
φ_p	V	hole quasi-fermi potential
χ	eV	electron affinity
ψ	V	electrostatic potential
2DEG	-	two-dimensional electron gas
2DHG	-	two-dimensional hole gas
a	Å	lattice constant of unit cell
a_e	Å	lattice constant 'a' of epilayer
a_e'	Å	strained lattice constant 'a' of epilayer
a_s	Å	lattice constant 'a' of substrate
b	(variable)	bowing factor (used during interpolation of band gap, polarization, etc.)
c	Å	lattice constant of unit cell
C_{11}	GPa	elastic constant
C_{13}	GPa	elastic constant
D	C/m^2	electric flux density
E	V/cm	electric field
e_{31}	C/m^2	piezoelectric constant
e_{33}	C/m^2	piezoelectric constant
E_C	eV	conduction band energy level
E_F	eV	semiconductor fermi energy level
EG	eV	band gap
E_i	eV	semiconductor intrinsic energy level
E_V	eV	valence band energy level
FF	%	fill factor

$In_xGa_{1-x}N$	-	indium gallium nitride with indium composition of 'x' and gallium composition of '1-x' ($0 \leq x \leq 1$)
IQE	%	internal quantum efficiency
I_{SC}	A	short-circuit current
J_{SC}	A/cm^2	short-circuit current density
MBE	-	molecular beam epitaxy
MOCVD	-	metal-organic chemical vapor deposition
n_s	m^{-2}	surface carrier concentration
P	C/m^2	polarization
P_{PZ}	C/m^2	piezoelectric polarization
P_{SP}	C/m^2	spontaneous polarization
QE	%	quantum efficiency
R	-	interface relaxation factor ($0<R<1$)
RC	μm	strain relaxation coefficient
V_{bi}	V	built-in potential
V_{OC}	V	open-circuit voltage
x	m	thickness

SUMMARY

Main objective of the present work is to develop wide-band gap InGaN solar cells in the 2.4 – 2.9 eV range that can be an integral component of photovoltaic devices to achieve efficiencies greater than 50%. The III-nitride semiconductor material system, which consists of InN, GaN, AlN and their alloys, offers a substantial potential in developing ultra-high efficiency photovoltaics mainly due to its wide range of direct-band gap, and other electronic, optical and mechanical properties. However, this novel InGaN material system poses challenges from theoretical, as well as technological standpoints, which are further extended into the performance of InGaN devices. In the present work, these challenges are identified and overcome individually to build basic design blocks, and later, optimized comprehensively to develop high-performance InGaN solar cells. One of the major challenges from the theoretical aspect arises due to unavailability of a suitable modeling program for InGaN solar cells. As spontaneous and piezoelectric polarization can substantially influence transport of carriers in the III-nitrides, these phenomena are studied and incorporated at a source-code level in the PC1D simulation program to accurately model InGaN solar cells. On the technological front, InGaN with indium compositions up to 30% (2.5 eV band gap) are developed for photovoltaic applications by controlling defects and phase separation using metal-organic chemical vapor deposition. InGaN with band gap of 2.5 eV is also successfully doped to achieve acceptor carrier concentration of 10^{18} cm^{-3}. A robust

fabrication scheme for III-nitride solar cells is established to increase reliability and yield; various schemes including interdigitated grid contact and current spreading contacts are developed to yield low-resistance Ohmic contacts for InGaN solar cells. Preliminary solar cells are developed using a standard design to optimize the InGaN material, where the band gap of InGaN is progressively lowered. Subsequent generations of solar cell designs involve an evolutionary approach to enhance the open-circuit voltage and internal quantum efficiency of the solar cell. The suitability of p-type InGaN with band gaps as low as 2.5 eV is established by incorporating in a solar cell and measuring an open-circuit voltage of 2.1 V. Second generation InGaN solar cell design involving a 2.9 eV InGaN p-n junction sandwiched between p- and n-GaN layers yields internal quantum efficiencies as high as 50%; while sixth generation devices utilizing the novel n-GaN strained window-layer enhance the open circuit voltage of a 2.9 eV InGaN solar cell to 2 V. Finally, key aspects to further InGaN solar cell research, including integration of various designs, are recommended to improve the efficiency of InGaN solar cells. These results establish the potential of III-nitrides in ultra-high efficiency photovoltaics.

1. INTRODUCTION AND RESEARCH OBJECTIVES

1.1 THE STRUGGLE FOR 'POWER'

Our history is directed by countless struggles for power, and the victorious, always glorified. Till the last millennium, power, which leads to the notion of supremacy, was appropriately glorified analogous to pseudo-significance of gold. Gold, although signifies prosperity, is ultimately just a shiny chunk of metal – beautiful to gaze at, but has no practical functionality! With the dawn of the new millennium rose the realization of a more specific and practical form of power. This time, prosperity was realized in the form of black-gold, or crude oil. This is now the new form of power, which not only dominates world politics, but also directly supports the grass-root activity of the society and has the potential to uplift human standards of living. However, this era of new power does not come without a new set of challenges – degradation of the environment, long-term sustainability and national security issues. Hence, our struggle for power persists as we explore alternate ways to secure our future.

1.1.1 Consequences of burning oil

Power form natural resources such as coal and crude oil produce greenhouse gases as a byproduct. As a result and owing to human activities, global atmospheric concentrations of carbon dioxide, methane and nitrous oxides have increased markedly since 1750, and now

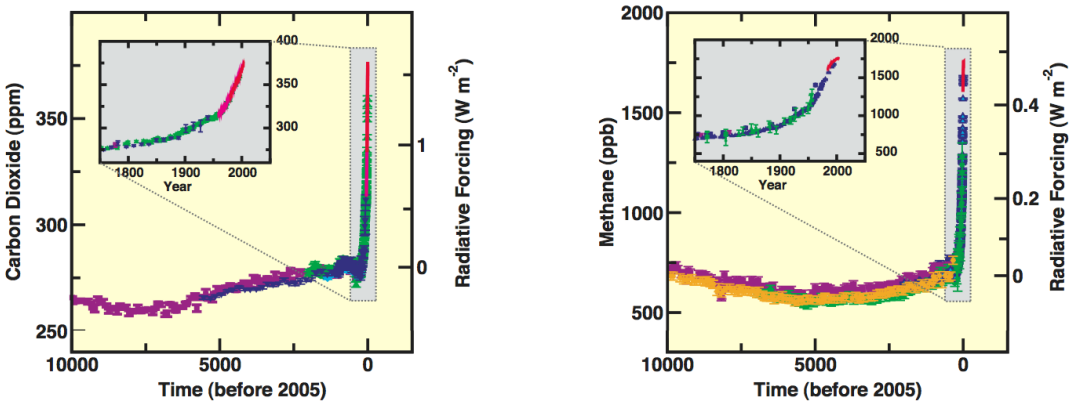

Figure 1.1: Historic perspective of global atmospheric concentrations of (a) carbon dioxide, and (b) methane.

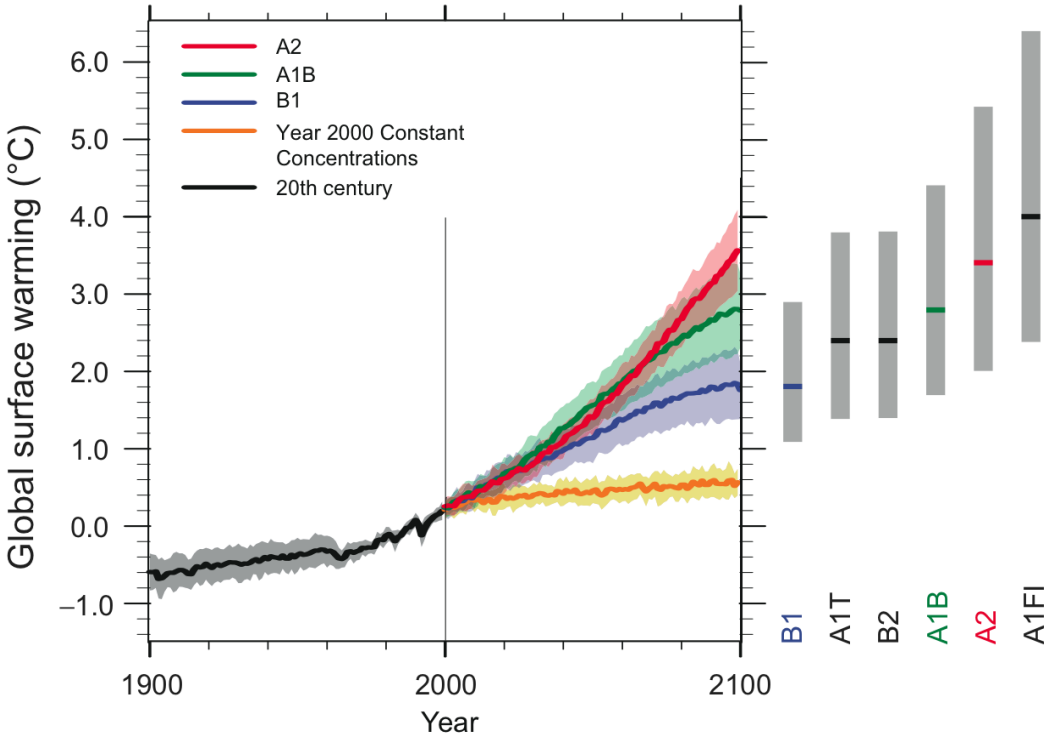

Figure 1.2: Multi-model averages and assessed ranges predicted for global warming.

far exceed pre-industrial values determined from ice cores spanning many thousands of years as indicated in Figure 1.1 [1]. Moreover, eleven of the last twelve years (1995 -2006) rank among the twelve warmest years in the instrumental record of global surface temperature (since 1850). This warming of the climate system, indicated in Figure 1.2, is unequivocal, as is now evident from observations of increases in global average air and ocean temperatures, widespread melting of snow and ice, and rising global average sea level. Burning conventional energy sources also has a direct impact on humans: each 1% loss of total ozone due to environmental pollution leads to a 3 – 5% increase in skin cancer cases [2]. While humans might manage to bite the bullet momentarily, the disruption in the ecological food chain will ultimately catch up to affect a healthy human life.

Our dependence on conventional energy resources has grown so much that it poses a question how well we will be able to cope in their absence. We have already become sensitive to the supply of oil as experienced through volatile petroleum prices. According to

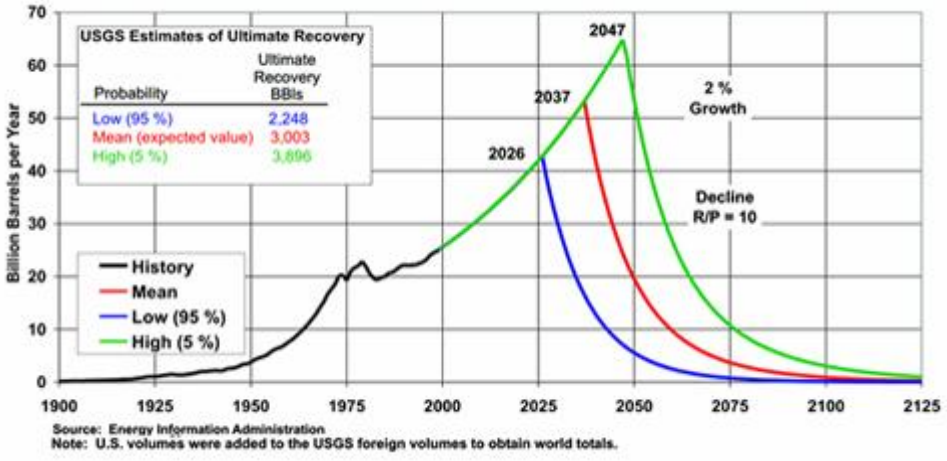

Figure 1.3: Annual production scenarios of world crude oil production with 2% growth rates

the United States Geological Survey (USGS) mean resource estimate, conventional crude oil production would be expected to peak in 2037 as shown in Figure 1.3 [3]. While bio-fuels may seem to be a potential solution to the oil shortage, they also contribute to greenhouse gases. Hence, this is the right time to start transitioning our dependence on the correct choice of non-conventional energy.

Finally, domestic and international conflicts for oil, like the civil wars in Africa and the 'Iraq situation', have become a routine segment in our news today. As nations realize that the cause of these tensions may also be motivated to amass energy resources, the necessity for self reliance for a prosperous and sustainable future becomes obvious. While we wander around gaping left and right, searching the corners of science for alternative energy, the solution lies directly on top of us – the Sun!

1.1.2 Harnessing the power of the Sun

The Sun is one of the most essential elements in nature required to sustain life. It has been recognized and worshipped for centuries, starting with the Harappan, Greek and Aztec civilizations, for its light, energy and cleansing powers. Today we recognize additional functionality of the Sun for processes such as photosynthesis and formation of fossil fuels. Among the various options for alternative sources of energy, the Sun poses to be appealing due to its essentially infinite and omnipresent nature. In fact, the solar energy resource is much greater than all other renewable and fossil-fuel based energy resources combined [4]. Sunlight reaching the earth's surface is almost 6,000 times the average power consumed by humans. These figures encourage us to look for ways to harness solar energy and convert it into other convenient forms.

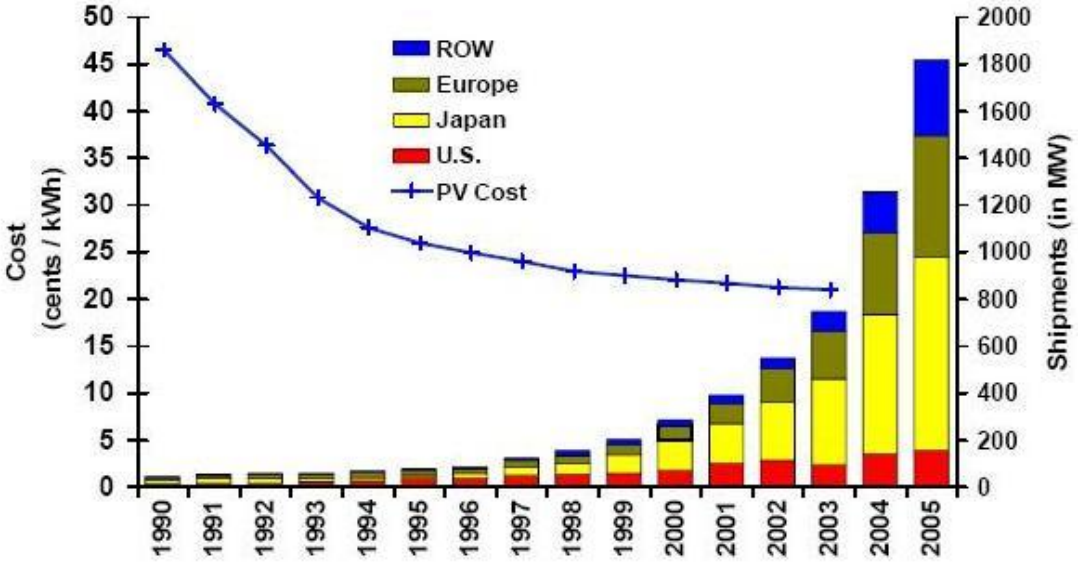

Figure 1.4: World PV cell/module

Photovoltaics (PV) is the direct process of converting sunlight into electricity. This process is highly reliable; easy to install; thrives on low operation cost; very safe; generally has no moving parts; while PV systems can be stand-alone, grid-connected, as well as modular. Moreover, this process does not involve any combustion or greenhouse-gas emission, thus making it safe for the environment.

1.1.3 High efficiency for economic viability

The global solar electricity market is currently more than $10 billion/year, and the industry is growing at more than 30% per annum [5][6] as indicated in Figure 1.4. In spite of this steady growth of the PV market, the current total global PV installed capacity is about 9 GWP [7], which accounts for only 0.04% of the world energy usage. While the current

generation cost of solar electricity in the United States is around $0.20/kWh [8] (prior to receiving subsidies), it still is about four times greater than its fossil-based competitor. This high price of solar-generated electricity compared to other conventional energy sources is primarily due to high manufacturing and installing costs; on the other hand, challenges such as system reliability, system integration and storage are continually being improved.

To economically reach its most competitive long-term position, it is argued that PV must push towards ever-increasing energy conversion efficiency while retaining low areal processing costs [9]. This leads to the concept of "third-generation" PV, which has a performance potential beyond that of single junction cells, while retaining the areal cost advantage of "second-generation" thin-film solar cells. This third-generation PV has the potential to achieve beyond the $1/W target as shown in Figure 1.5, which is equivalent to the price of fossil-based electricity.

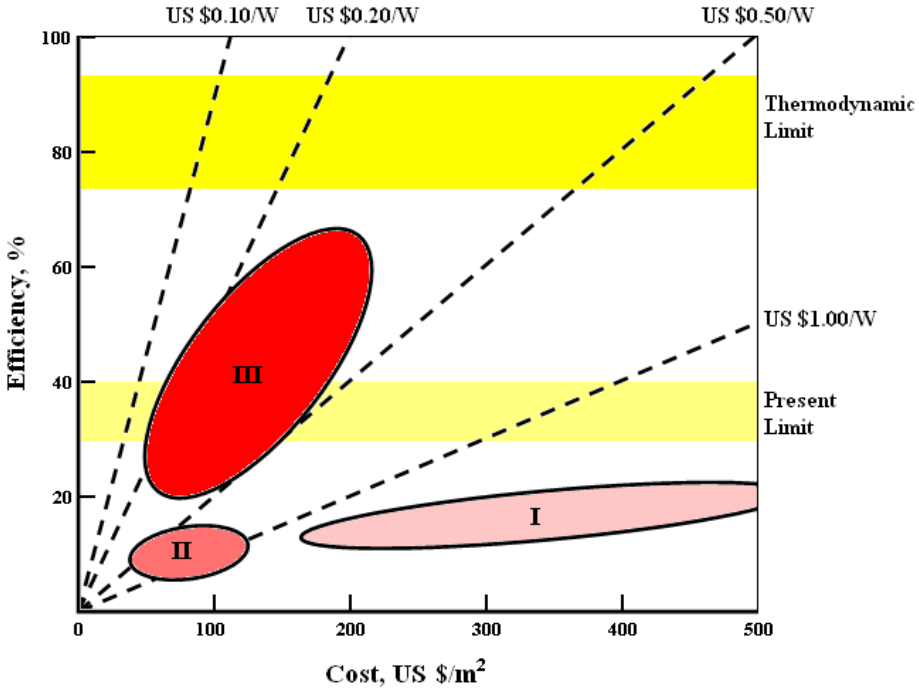

Figure 1.5: Efficiency and cost projections for first, second and third generation PV [9].

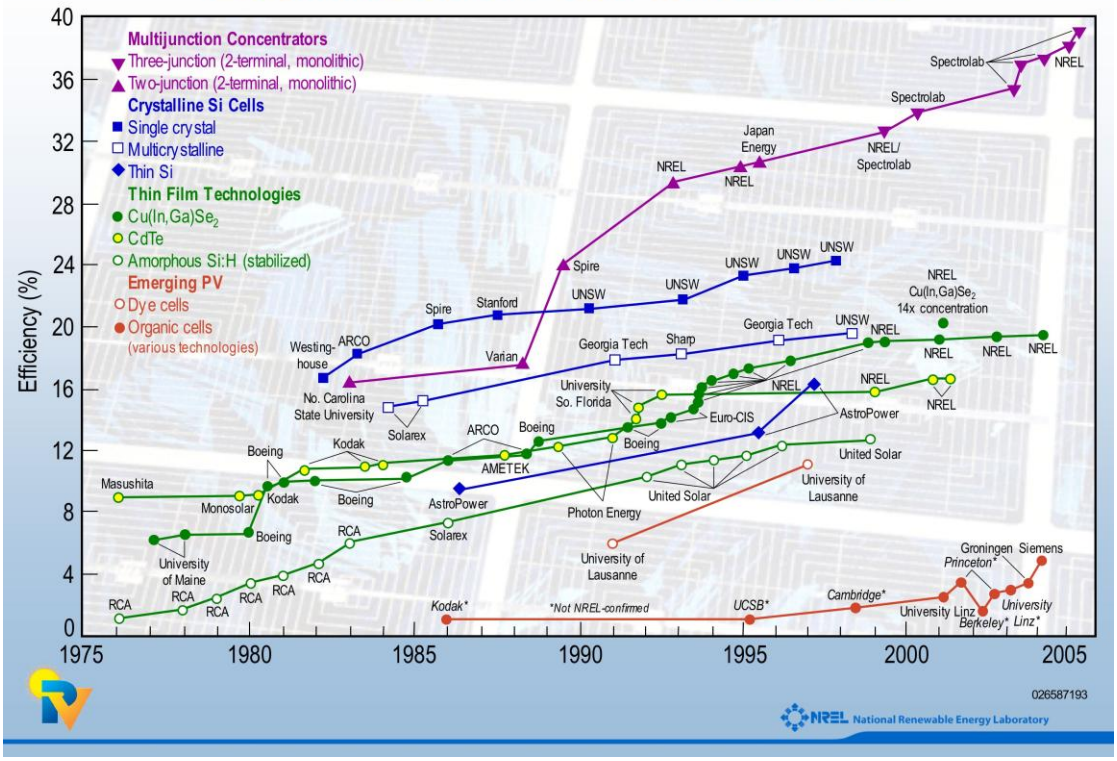

Figure 1.6: Best research-cell efficiencies [10].

The progressive development of record-efficiency solar cells is summarized in Figure 1.6 [10], where the emerging multi-junction concentrator solar cell efficiencies have clearly dominated over other technologies. The current efficiency record is held by a triple-junction tandem solar cell at 40.7% [11][12]; however, modeling results indicate that such structures are approaching their theoretical efficiency limits.

Overcoming the 50% efficiency barrier demands exploration of new material systems and probably novel solar cell architectures. The Indium Gallium Nitride (InGaN) material system, although in its rudimentary stages of development, demonstrates the versatility and promise as a successful high-efficiency photovoltaic material.

1.1.4 VHESC – An ultra-high efficiency approach

One potential application of an InGaN photovoltaic device is in the Very High Efficiency Solar Cell, which targets an efficiency of greater than 50% [13]. High efficiency modules are being developed based on the co-design of the optics, interconnects and solar cells as shown in Figure 1.7. This architecture significantly increases the design space for high performance photovoltaic modules in terms of materials, device structures and manufacturing technology. It allows multiple benefits, including increased theoretical efficiency, new architectures which circumvent existing material/cost trade-offs, improved performance from non-ideal materials, device designs that can more closely approach ideal performance limits, reduced spectral mismatch losses and increased flexibility in material choices. An integrated optical/solar cell allows efficiency improvements while retaining low area costs, and hence expands the applications for photovoltaics. It allows a design approach which focuses first on performance, enabling the use of existing state-of-the-art photovoltaic

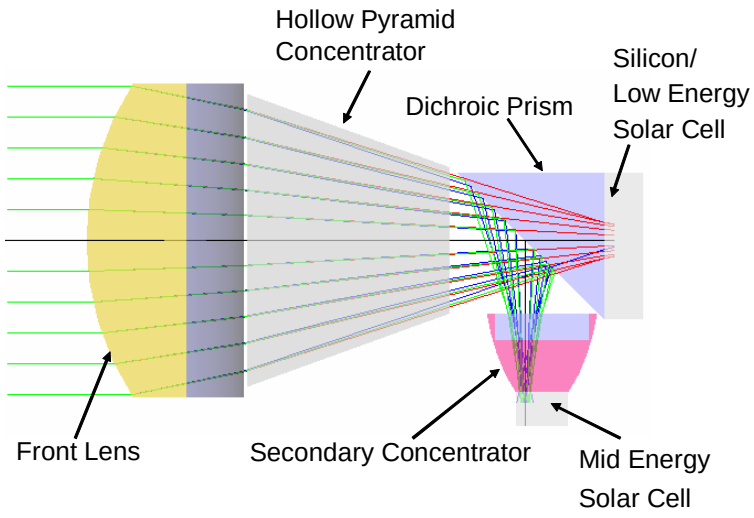

Figure 1.7: Schematic of the architecture of VHESC.

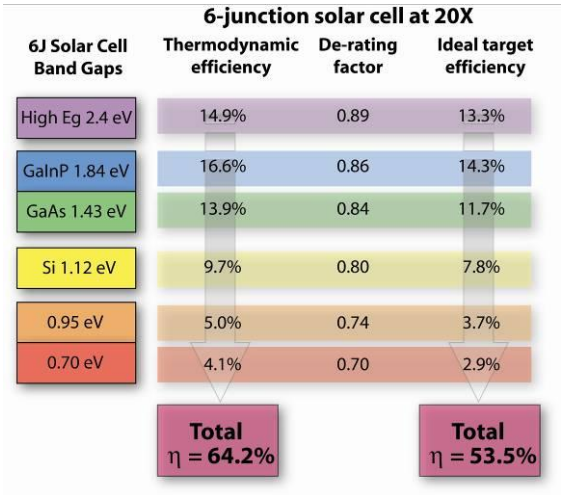

Figure 1.8: Predicted contributions of each solar cell in the proposed VHESC design.

technology to design high performance, low cost multiple junction III-Vs for the high and low energy photons and a new silicon solar cell for the mid-energy photons, all while circumventing existing cost drivers through novel solar cell architectures and optical elements.

Figure 1.8 breaks down the predicted efficiency contribution at each energy level of the VHESC to reach a practical efficiency of greater than 50%. InGaN is one of the few material systems that can provide band gaps of 2.4 eV or greater, which is critical to reach the 50% target as seen from the figure. Thus, it is vital to explore InGaN for photovoltaic applications.

1.2 SPECIFIC RESEARCH OBJECTIVES

Due to the multi-faceted challenges in the InGaN material system, which will be briefly discussed with respect to each task and elaborately in Chapter 2, it is imperative to

take an iterative approach addressing these challenges simultaneously to successfully develop high-performance InGaN solar cells. This iterative process is further divided into the following tasks, most of which are to be pursued simultaneously.

1.2.1 Task 1: Develop an accurate modeling tool for III-nitride solar cells

Preliminary studies indicate phenomena in the III-nitrides that are uncommon in semiconductors typically used for photovoltaic applications. Spontaneous and piezoelectric polarization in the III-nitrides tend to generate additional electric fields in the device [14][15]; InGaN may demonstrate instances of lower band gap phase separated alloys that have a direct effect on the performance of the solar cell [16][17]; it is a technological challenge to form low-resistance Ohmic contacts to a p-type III-nitride junction and the contact may demonstrate Schottky characteristics [18][19]. Typical solar cell modeling programs like PC1D [20] do not incorporate phenomena such as polarization, phase separation or Schottky contacts; while device modeling programs for the III-nitrides such as SiLENSe [21] are typically designed for Light Emitting Diodes (LED's) and Laser Diodes (LD's). Hence, it becomes imperative to develop a modeling tool to accurately design InGaN solar cells.

1.2.2 Task 2: Optimize MOCVD growth of InGaN for band gaps as low as 2.4 eV

Due to fundamental thermodynamic limitations during growth of InGaN, it is difficult to obtain high crystalline quality at indium-rich low band gaps. Phase separation [16][17], p-type doping [22][23] and high defect density [24]-[27] are commonly observed challenges in the III-nitrides at increasing indium compositions. While thin layers of wide-

band gap InGaN are commonly used in the LED industry to form quantum wells [28], lower band gap InGaN in the bulk form still remains an active area of research. As material quality directly affects the solar cell performance, it is important to understand and control each of theses aspects during epitaxial MOCVD growth. The target band gap of InGaN is determined to be 2.4 eV for the present work as it absorbs substantial sunlight for functioning in a potentially 50% efficient tandem cell.

1.2.3 Task 3: Develop efficient fabrication scheme for InGaN solar cells

The III-nitrides pose unique challenges in fabrication of solar cells particularly due to the high resistivity in the material and the unavailability of metals to naturally form an Ohmic contact to a p-type alloy. While the fabrication techniques for GaN based optoelectronic and power devices are currently explored elsewhere [28], fabrication of solar cells demands a unique of requirements as they have to be optimized for light absorption and minority carrier collection. Both p- and n-contacts are to be developed on the same side of the wafer as the substrates typically used for the III-nitride solar cells like sapphire are intrinsic. Metallurgical current spreading layer used in typical III-nitride optoelectronic devices can be detrimental to solar cell performance as they cause a substantial shading loss; moreover, theoretically optimized grid contacts also shade the solar cell by 50% due to high resistivity of the material. Formation of Schottky contacts can reduce the open-circuit voltage and collection efficiency of the solar cell. Moreover, a robust fabrication scheme is required to improve reliability and repeatability of the manufacturing process. Fabrication schemes of the solar cells may also be coupled with basic device design, which may involve band engineering to enhance the performance of the device.

1.2.4 Task 4: Understand loss mechanisms in InGaN solar cells due to material quality and fabrication issues

As mentioned earlier, phenomena such as polarization, phase separation and high defect density may complicate the identification of loss mechanisms and analysis of InGaN solar cells. Non-optimal contact may excessively absorb and reflect incident light, and form a Schottky barrier at the contacts. It is crucial to individually identify the implication of each phenomena occurring in the device to systematically design and enhance the performance of the solar cell as a whole.

1.2.5 Task 5: Design efficient InGaN solar cell in the 2.4 – 2.9 eV range

The designing of efficient InGaN solar cells requires comprehending all the previous tasks and applying them to realize one or more types of devices. The design process has to take into account material limitations due to technological challenges and provide robustness to account for error during modeling. Band engineering is a useful tool that can be used to compensate for the losses due to limitations in fabrication technology of the solar cell. Such challenges may even call for investigation into novel device structures. Thus, efficient InGaN solar cells in the 2.4 – 2.9 eV range can be realized by systematically achieving the given tasks.

1.3 SUMMARY

The increasing demand and limited supply of energy poses a grave threat not only to the extravagant desires but also to basic necessities of today's society. Photovoltaics is an advantageous and viable alternative to satisfy this energy demand. InGaN is a novel material

system that offers substantial potential for high-efficiency photovoltaics, through which solar energy costs can be driven lower. The aim of this work is to develop a high-performance InGaN solar cell in the 2.4 – 2.9 eV range. The development process requires an iterative approach which is broken down into specific tasks involving modeling, design, growth, and fabrication and analysis.

2. InGaN FOR HIGH-EFFICIENCY PHOTOVOLTAICS

2.1 EFFICIENCY LIMITS IN A SINGLE JUNCTION SOLAR CELL

As explained in the previous chapter, high-efficiency solar cells are desirable for long-term economic viability. The bulk of the solar cells commercially available are based on single- and multi-crystalline single junction silicon technology. The maximum photovoltaic efficiency for a single junction band gap of 1.1eV illuminated by a blackbody at 6000K as predicted by Shockley and Queisser using detailed balance modeling is 31% [29]. The

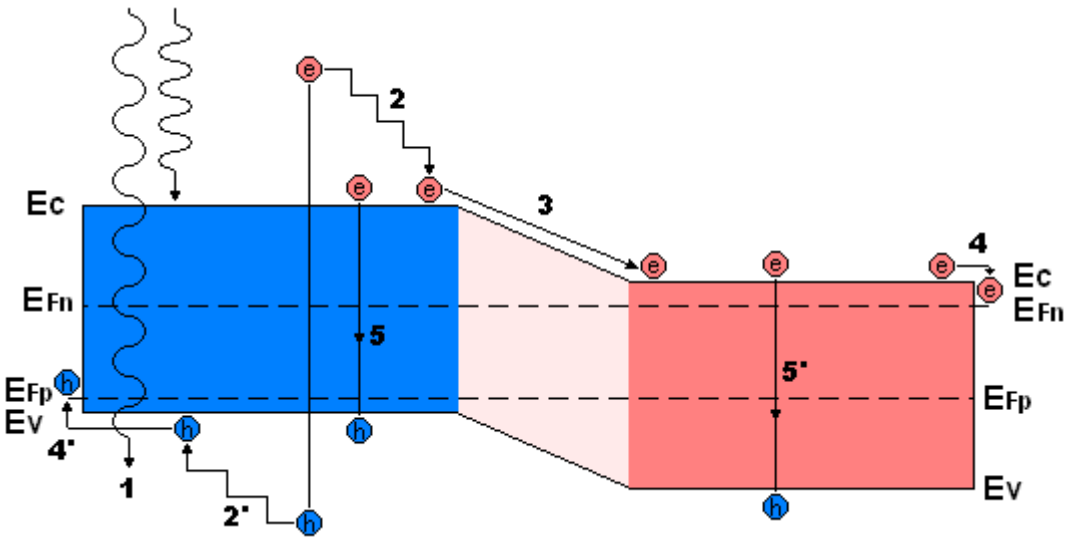

Figure 2.1: Major loss processes in a single-junction solar cell under forward bias: (1) Transmission of low energy photons, (2) Thermalization loss, (3) Junction voltage loss, (4) Contact voltage loss, and (5) recombination Loss.

thermodynamic efficiency limit of single-junction solar cells is 31% at one sun and 41% at maximum concentration compared to an infinite stack tandem or an equivalent solar cell at 86.8% [30], which is in agreement with the detailed balance efficiency limit [31]. However, the highest efficiency recorded in silicon solar cells is 24.7% (PERL) [32], while majority of the modules available in the market range around 13-17% due to losses associated with them.

The major loss mechanisms in a standard solar cell are shown in Figure 2.1. One of the major loss mechanisms (1) is the transmission of long-wavelength low-energy photons. If the energy of photons is less than that of the constituent semiconductor band gap, then such photons are not absorbed at all and are transmitted through the solar cell. This loss mechanism cuts down the single-junction silicon solar cell efficiency by 23%.

Another major loss mechanism, thermalization loss (2), is caused when the photo-excited electron-hole pair quickly loses its energy in access of the semiconductor band gap due to absorption of a high-energy photon. Hence, a low-energy red photon would only be as effective as a high-energy blue photon. This process cuts down the solar cell efficiency by 38%.

Voltage losses occur due to the fact that the output voltage of a cell is less than the potential equivalent to its band gap energy. Voltage losses can be caused by losses at the diode junction or external contacts. In case of silicon, the band gap corresponds to about 1.1V, while its maximum achievable output voltage is only 0.785V.

Recombination loss is another loss mechanism that may prove to be detrimental for cell performance if the material quality is not considered. Here, the electrons and holes recombine instead of migrating to their respective junctions and thus, are wasted. Recombination accounts for about 5% loss in present day conventional cells. Other loss

mechanisms include diode curve factor losses (14%), material and contact resistance losses (5%), and reflection and shading losses (5%) [33].

2.2 HIGH-EFFICIENCY APPROACHES

While evolutionary methods such as reducing the thickness of the wafers, buried contacts to reduce shading [34] and surface texturing to reduce reflection [32] are used mainly to improve single-junction silicon solar cell efficiencies, revolutionary concepts are studied to drive the high-efficiency solar cells towards their ultimate thermodynamic limit. The most successful method in achieving high efficiencies today is a comparatively simpler and intuitive design – the tandem solar cell [35][36]. The triple-junction GaInP-GaInAs-Ge tandem currently holds the efficiency record of 40.7% at 240 suns [12]. Also nanoelectronic concepts like quantum-wells [37][38] and intermediate bands [39] can be incorporated in solar cells to increase the number of effective band gaps.

2.2.1 Tandem solar cells

The major loss processes of thermalization and non-absorption can be largely eliminated if the energy of the absorbed photon is marginally higher than the band gap of the cell material. This leads to the concept of the tandem cell [35][36], where multiple cells are used with different band gaps, each cell converting a narrow range of photon energies close to its band gap as shown in Figure 2.2.

The high-gap cells are stacked on the top, which efficiently absorb the high-energy photons, transmitting the lower energy photons to the cells with lower band gaps. Earlier tandem cells used in space applications were mechanically stacked and individually probed.

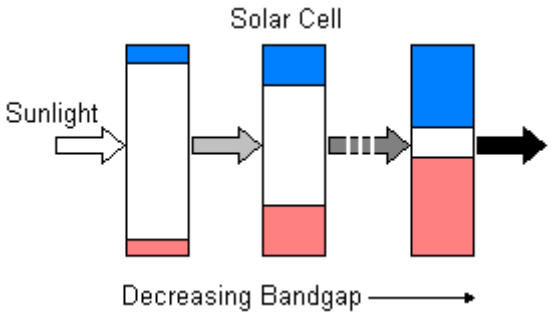

Figure 2.2: Concept of tandem cell.

With the improvement in growth technology, individual cells are monolithically grown on top of each other. Such devices function in series with only two probes for external connection, while they are internally connected through tunnel-junctions, which display Ohmic characteristics. Performance of a tandem increases as the number of cells in the stack increases, with a direct sunlight conversion efficiency of 86.8% calculated for an infinite stack of independently operated cells under maximum concentration. However, increasing the number of stacks adds complications and makes the tandem sensitive to the irradiating spectrum as these individual cells have to be connected in series with low Ohmic contact resistance and have to be current matched.

2.2.2 Quantum-well solar cells

A multiple-energy gap structure, similar to tandem solar cells, can also be achieved using the Quantum-Well Solar Cell (QWSC) structure was proposed by Keith Barnham's group in 1991 [37][38]. In its simplest form, the QWSC consists of a p-i-n solar cell with a Multi-Quantum-Well (MQW) system added to the Intrinsic (i) region as shown in Figure 2.3. The i-region extends the field bearing region of the p-n junction. Thin alternate layers, in

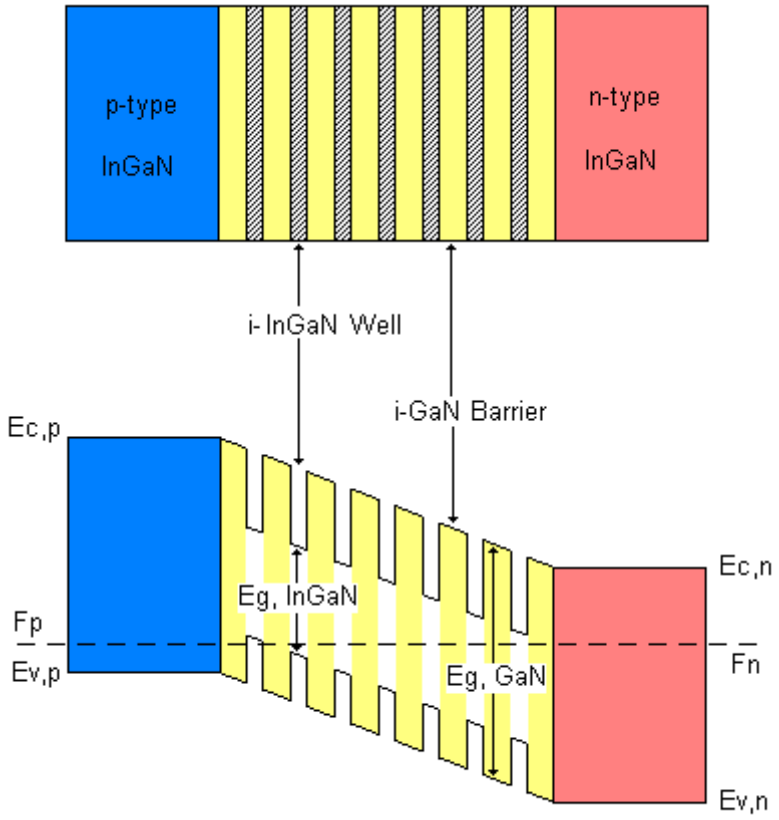

Figure 2.3: Quantum-well solar cell structure and band diagram.

orders of a few nanometers, of a lower band gap material are grown within the i-region. These low-band gap materials appear as wells in the energy-band diagram.

The quantum wells (QW's) generate quantized energy levels within the well corresponding to the band gap and dimensions of the well. Such a MQW system or super-lattice behaves as a superposition of semiconductors with band gaps equivalent to the difference in these energy levels. This super-lattice absorbs photons of energy less than the band gap of the bulk or barrier material, which would otherwise have been wasted in the PV conversion process. This additional absorption increases the photo-generated current boosting the net efficiency of the solar cell. The output voltage of the

cell lies between that of the conventional cell comprised of the material of the well and one comprised of the barrier material. The absorption properties of QW solar cells can be altered by tailoring the number and size of the QW and barriers and thus, reach an optimum. In this way, QW solar cells incorporate the principles of tandem solar cells and can theoretically achieve equivalent efficiencies.

2.2.3 Other high-efficiency concepts

The Intermediate Band Solar Cell (IBSC) also follows a multi-band approach like tandems and QWSC's, where the additional band is incorporated within the single junction solar cell [39]. Such solar cells behave as a superposition of three band gaps and theoretically less sensitive to spectral variations compared to tandems. Intermediate bands are practically realized via mid-gap impurities or quantum dots. Thus, the efficiency of IBSC's is enhanced by 'up conversion' of low energy photons.

Hot carrier solar cells work on the principle that photogenerated carriers must not relax to band edges by interaction with absorber lattice [40]. For peak efficiency, radiative recombination must be faster than such relaxation. This is not a trivial requirement, but such structures can be obtained through low dimensional and molecular systems. Such devices offer a substantial spectral tolerance.

Contrary to combining two low-energy photons to obtain a high-energy electron-hole pair, a high energy photon can be used to yield multiple low-energy electron-hole pairs. This process can be realized through impact ionization in low-band gap structures. The generation of at least 3 electron-hole pairs per incident photons has been demonstrated in

quantum dots of PbSe and PbS [41][42]. This process was enhanced by the discretization of energies caused by confinement in quantum dots.

2.3 THE INGAN MATERIAL SYSTEM

Optimum values for band gaps of multijunction or equivalent solar cells calculated through detailed balance modeling are presented in Table 2.1 [29][43]. It is observed that mature photovoltaic technologies are typically able to achieve about 80% efficiencies of their thermodynamic limit. For example, the PERL cell developed by the University of New South Wales holds the efficiency in silicon at 24.7% (AM1.5) [32] and the best gallium arsenide cell records 25.1% (AM1.5) [44] compared to their limit at 31% (AM0); while the best triple-junction efficiency available today is 40.7% [12] compared to its detailed balance limit at 56%. Hence, to achieve practical photovoltaic efficiencies greater than 50%, solar cells consisting of five or more band gaps are required. Moreover, it can be seen that such solar cells also require band gaps greater than 2.4 eV to reach this 50% target.

Table 2.1: Detailed balance calculations of band gaps and achievable efficiencies of 3 to 8 stack tandem solar cells under black body radiation at 6000K, 500x.

n	Values of Band Gap								η (%)	$0.8 \cdot \eta$ (%)
3	0.7	1.37	2						*56*	*44.8*
4	0.6	1.11	1.69	2.48					*62*	*49.6*
5	0.53	0.95	1.4	1.93	2.68				*65*	*52*
6	0.47	0.84	1.24	1.66	2.18	2.93			*67.3*	*53.84*
7	0.47	0.82	1.191	1.56	2	2.5	3.21		*68.9*	*55.12*
8	0.44	0.78	1.09	1.4	1.74	2.14	2.65	3.35	*70.2*	*56.16*

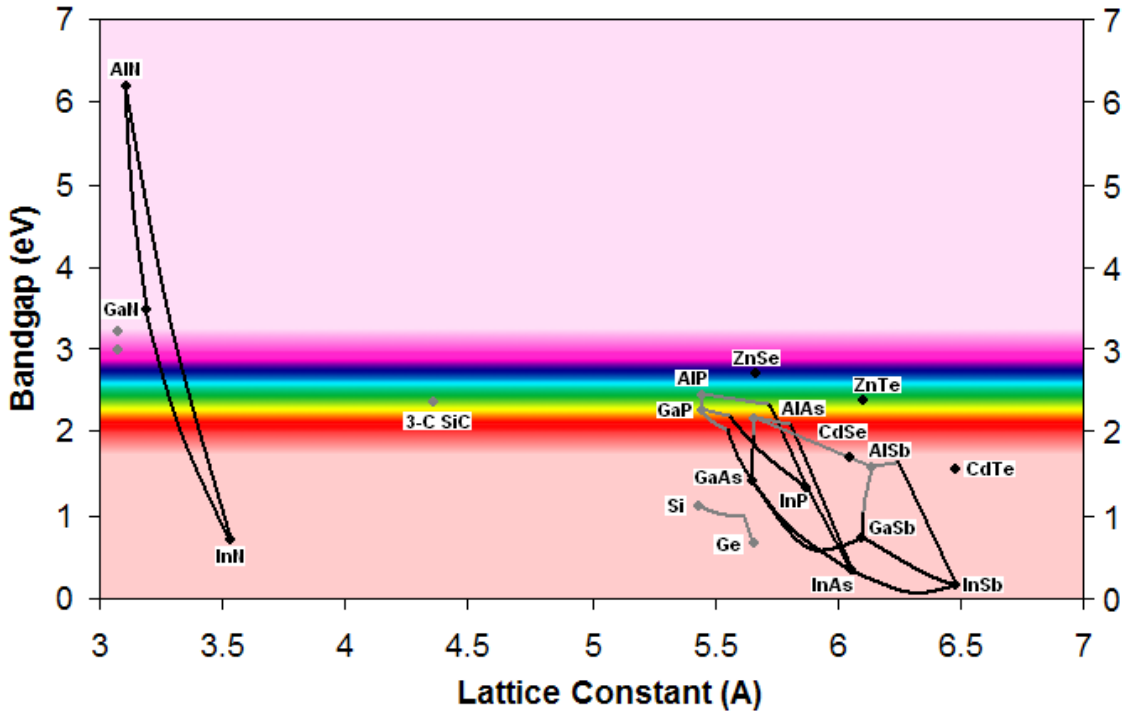

Figure 2.4: Band gap Vs. lattice constant of common semiconductor materials.

It is seen from Figure 2.4 that the III-V nitride material system, which consists of InN, GaN, AlN and its alloys, are among the few materials that can provide band gaps greater than 2.4 eV. The indium-lean, wide-band gap end of the InGaN material system, typically grown my Metal-Organic Chemical Vapor Deposition (MOCVD), is extensively used in blue Light Emitting Diodes (LED's) and Laser Diodes (LD's) [28]. While the band gap of the blue LED's at 3.4 eV is higher than the optimal range of solar cells, the recently emerging green LED's are useful for wide-band gap InGaN solar cells that can be used in tandems with five or greater junctions.

Moreover, the InGaN material system offers a substantial potential to develop ultra-high efficiency solar cells. With the recent revision of the band gap of In at around 0.65eV

[45]-[47], the band gap of the InGaN material system ranges the bulk of the solar spectrum including the visible region. A continuum of band gaps can be obtained by changing the compositions of indium and gallium making it relatively easier for MOCVD and Molecular Beam Epitaxy (MBE) growth processes limiting the number of material sources compared to other III-V materials. InGaN also has an apparent insensitivity to high dislocation densities as the polarization and piezoelectric properties [14][15] of the material introduce electric fields and surface diploes that may counter the effect of dislocations. Additional advantages include low effective mass of electrons and holes, high mobilities, high peak and saturation velocities, high absorption coefficients and radiation tolerance [48].

2.4 CHALLENGES IN THE INGAN TECHNOLOGY

As the III-nitride material system is still in its developing stages, there are some technological challenges to be overcome. The challenges can be generalized under two main classifications: (1) material quality, and (2) device design. The issues concerning lack of suitable substrate, high dislocation density, thermodynamic non-equilibrium during growth, phase separation, and p-type doping have a direct impact on material quality; while challenges pertaining to Ohmic contacts to p-type material and suitable transparent contact have additional consequences on device performance. The present work addresses all these challenges in order to establish InGaN as a high-performance photovoltaic material.

2.4.1 Substrates and crystalline quality

Growth of III-nitride epitaxial layers has been intensively studied due to fundamental challenges associated with obtaining material of high crystallinity. Crystalline perfection of

Table 2.2: Lattice mismatch and thermal expansion coefficient mismatch of GaN with common substrates.

Substrate	Lattice mismatch	Thermal Expansion Coefficient mismatch
Sapphire	16%	-34%
SiC	3%	+25%
ZnO	2%	-14%
Si	17%	+100%

epitaxial structures is one of the main factors that affect the electrical and physical parameters of the material, and consequently, limit their applications.

The III-nitrides typically crystallize in a wurtzite crystal structure, unlike Si, Ge, and GaAs, which crystallize in a diamond or zinc-blend structure. Sapphire is the most commonly used substrate for the growth of wurtzite GaN. However, due to the large lattice mismatch (16% for GaN on sapphire and 29% for InN on sapphire) and thermal mismatch (-34% for GaN on sapphire and -100% for InN on sapphire) between sapphire and III-Nitrides, epitaxial films on sapphire result in high dislocation densities. Other substrates are SiC and ZnO, which provide better lattice match, but nevertheless have similar dislocation densities and Thermal Expansion Coefficient (TEC) mismatch as shown in Table 2.2.

Crystalline defects originate as point defects at the growing surface due to the mismatch strain at the growth temperature and imperfect stoichiometry. Point defects appear on the growth surface at the moment of coalescence of nucleus [49][50]. Diffusion of point defects and their structural transformation lead to the creation of clusters of point defects, stacking faults, dislocations, and dislocation accumulations (dislocation walls). High dislocation density in the 10^{7}-10^{10} cm^{-2} range has a significant influence on device applications and is still a major technological challenge [24]-[27].

As a result it becomes progressively difficult to incorporate higher indium compositions in InGaN. Moreover, in spite of the advances made in science today, due to unavailability of high quality material, the band gap of InN is still a topic of debate [51][52]. Consequently, it becomes more difficult to fabricate InGaN solar cells at higher indium compositions.

2.4.2 Phase separation

There exists of a solid phase miscibility gap in the InGaN alloy due to the large difference in the lattice constants between GaN and InN, which is also the probable cause of multiple phases and consequent multi-peak luminescence observed in the material [16][17]. The equilibrium solubility of InN in the bulk GaN is approximately 6% at typical growth temperatures used in MOCVD. However, the situation in thin InGaN films epitaxially deposited on GaN virtual substrates is significantly different. Theoretical calculations [53] based on a valence-force-field (VFF) model [16][54] predict that phase separation in InGaN

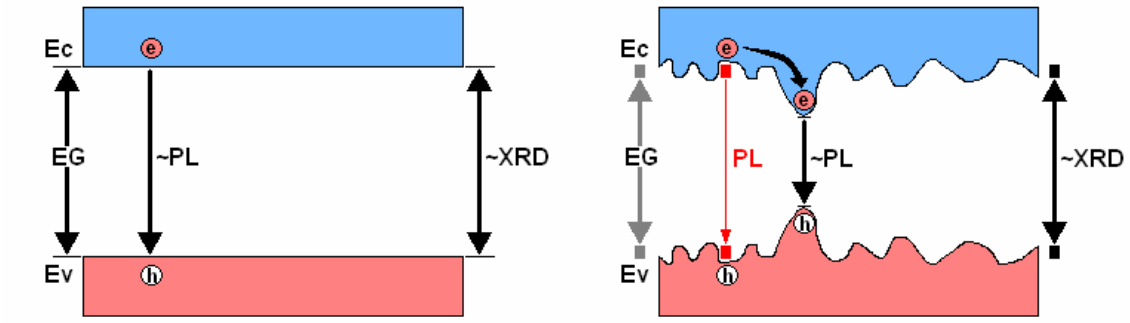

(a) (b)

Figure 2.5: Schematic comparison of band structures of (a) an ideal material, and (b) a phase separated material.

strongly depends not only on the temperature and In composition, but also on the strain state of the InGaN films. Thus, one or more indium-rich phases come into existence in the InGaN alloy layers during growth in an attempt to reach thermodynamic equilibrium during growth as shown in Figure 2.5. Phase separation is usually identified as secondary peaks in addition to the primary peak corresponding to the bulk material during photoluminescence and, while higher degrees of phase separation are also identified via X-ray diffraction (XRD).

In addition to acting as a recombination channel, it can be correlated from quantum-well solar cells that the lower-band gap phase separated material will also tend to pin down the open-circuit voltage (V_{OC}) of the solar cell. Hence, it becomes critical to understand the effects and control phase separation to fabricated successful InGaN solar cells.

2.4.3 P-type doping

Achieving p-type conductivity in InGaN alloys is difficult partly due to a high background concentration of donors that arise from native defects [22][23]. Moreover, relatively deep acceptor levels and a low activation efficiency result in low hole concentrations of Mg-doped III-nitride alloys at room temperature. The activation energy of Mg in GaN is around 204 meV [55][56], but decreases with the increase in indium composition [57][58]. As a result, it is theoretically possible to achieve higher acceptor concentrations at higher indium compositions. On the other hand, at very high indium compositions, the acceptor concentrations decrease due to degradation in crystal quality [59].

Achieving high acceptor levels in a material is important particularly in wide-band gap semiconductors to form p-n junctions with low series resistance and extract maximum V_{OC} out of the resultant solar cell by compensating for low minority carrier lifetimes.

Moreover, a lower resistance p-type material relaxes the constraints on grid spacing for the top contact in a solar cell reducing shading loss.

2.4.4 Ohmic contact to p-InGaN

One of the major implications of low acceptor concentrations in the III-nitrides is the challenge in achieving high-optoelectronic quality contacts to p-type material. In addition to high contact resistivity due to low acceptor concentrations, there is no readily available metal that can form an Ohmic contact to p-type InGaN due its high work-function. Figure 2.6 gives an idea of the work functions of metals commonly used to obtain Ohmic contacts with respect to conduction and valence band edges of InGaN ($0 \leq [In] \leq 0.5$) and vacuum level.

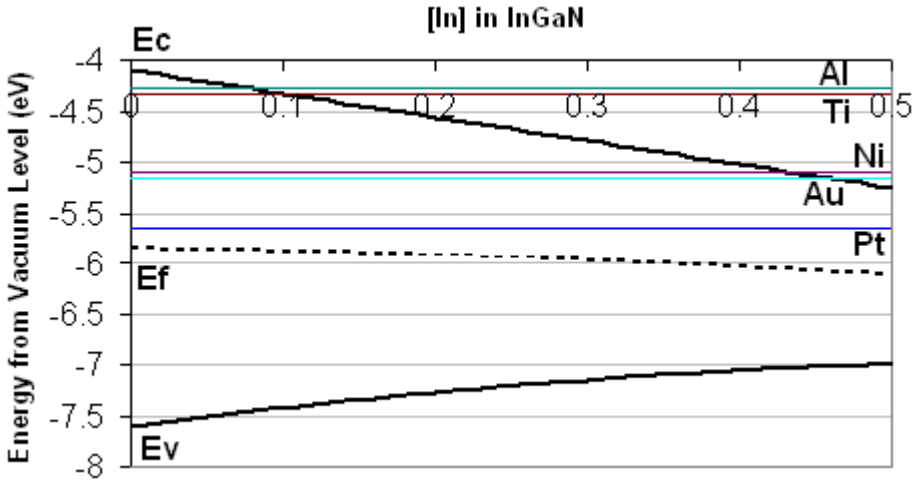

Figure 2.6: Work function of common metals used to obtain Ohmic contacts with respect to conduction and valence band energies of InxGa1-xN for $0<x<0.5$.

Metallization schemes involving high work functions such as Au [60][61], Ni [60][62], Pd [63], Pt [60],[64], Pt/Au [64][65], Cr/Au [66], Pd/Au [65][67], Pd/Pt/Au [64], Ni/Cr/Au [68], Ni/Pt/Au [69][70] and Pt/Ni/Au [70][71] have widely been investigated. However, such contacts fail to overcome the Schottky barrier at the p-type III-nitride interface or provide low Ohmic resistances, and hence are not preferred for practical applications. There have also been several attempts to reduce the contact resistance by surface treatment [72][73], and annealing.

Recently developed NiO_x metallurgical junctions have achieved specific contact resistances as low as 10^{-6} $\Omega \cdot cm^2$ [18][19]. Figure 2.7 illustrates the band diagrams of such contacts that justify the mechanism of the contact. It is seen in Figure 2.7(b) that a potential well for holes and a built-in potential are formed at the p-GaN/NiO_x surface. For very thin NiO_x layers, such contacts utilize tunneling of electrons through the Au/NiO_x interface barrier where they are injected into the notch to recombine with holes at the p-GaN surface as shown in Figure 2.7(c).

However, such NiO_x contacts tend to cover the entire top surface of the device that absorb light, and hence, decrease the efficiency of the solar cell. Other transparent conducting oxides such as Indium-Tin Oxide (ITO) yield better transparency [74], but form Schottky contact to p-type InGaN [75].

Alternative methods involving band gap engineering have also been investigated; a short-period superlattice (SPS) structure can be grown that combines the p-type layer with the well material using InN [76], InGaN [77] or AlGaN [78] to form an Ohmic contact. This kind of a structure is advantageous to solar cells as it also enhances lateral transport of the carriers improving collection probability.

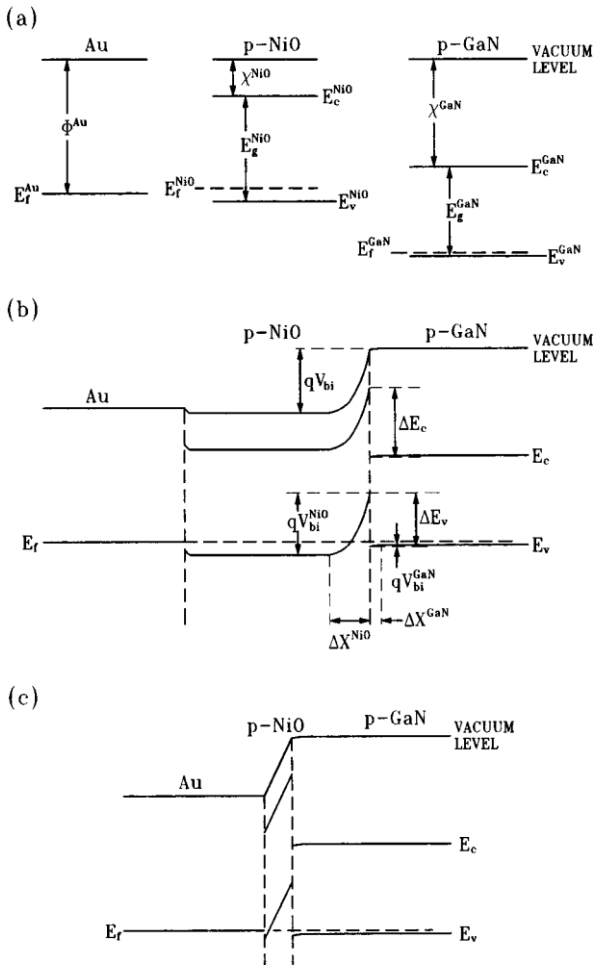

Figure 2.7: Equilibrium energy band diagram of (a) bulk Au, p-NiO, and p-GaN, (b) Au/thick p-NiO/p-GaN heterostructure, and (c) Au/thin p-NiO/p-GaN heterostructure.

2.5 SUMMARY

In summary, it is established that the loss mechanisms in a single junction solar cell limit its efficiency to about 25%. These loss mechanisms can be overcome using high efficiency concepts such as tandem and quantum-well solar cells. The novel InGaN material system, although in its rudimentary stages, offers substantial potential for fabricating such high-efficiency solar cells and in achieving practical efficiencies of greater than 50%.

Improvements on the fronts of crystalline perfection, phase separation, acceptor activation, and high-quality optoelectronic contacts are mandatory to develop high-performance III-nitride optoelectronic devices including solar cells. The study and optimization of all these aspects are addressed in the following chapters, which are consequently integrated to develop InGaN solar cells in the final chapters.

3. EXPERIMENTAL APPROACH AND DESIGN OF InGaN SOLAR CELLS

3.1 GENERAL SOLAR CELL DESIGN PRINCIPLES

Successful III-nitride solar cells are developed following the basic design principles, as these rules remain unchanged irrespective of the semiconductor material. Moreover, it becomes important to completely comprehend these principles for novel semiconductors like InGaN in order to explore new designs, as common designs may not be technologically viable. The four aspects considered while designing single-junction InGaN photovoltaic devices, just like any other solar cells, are:

1. Maximizing absorption in the solar cells to increase the number of photogenerated carriers,
2. Maximizing collection of the photogenerated carriers at the p- and n- junctions,
3. Minimizing the forward bias dark current, and
4. Minimizing resistive losses in the bulk as well as external contacts of the device.

3.1.1 Light absorption

The short-circuit current (I_{SC}) of the solar cells directly depends on amount of light absorbed by that device. Moreover, it is intended to maximize light absorption in the depletion region of the solar cell diode to improve the collection probability of the

photogenerated carriers. The following methods can be used to maximize light absorption in a solar cell:

1. **Increasing device thickness:** For a given material, where the band gap is not a variable, the most intuitive method for increasing light absorption is by increasing the thickness of the device. However, this method may not be viable beyond a certain limit for materials like InGaN, where phase separation and defects may increase at higher thicknesses and have a negative impact on device performance.
2. **Light trapping:** Alternatively, the effective thickness of solar cells can be increased by increasing the optical path length of light entering the device. Back surface mirrors involving metals or Bragg reflectors [79][80] can be used for this purpose. Such Bragg reflectors are investigated for GaN-based LED's and lasers, and can be integrated into InGaN solar cells [81].
3. **Anti-Reflection Coating (ARC):** While typically 30% of light is reflected off a smooth silicon surface, ARC's such as silicon nitride can drastically reduce this reflection [82] and are commonly used in solar cells. Such ARC's can also be deposited on III-nitride solar cells during the final steps of fabrication.
4. **Surface texturing:** Texturing of surface not only minimizes reflection from the solar cell surface, but also increases the optical path length of light entering the device by deviating the incoming light as shown in Figure 3.1 [83]. Such texturing can also be applied to substrates like sapphire, silicon carbide or zinc oxide, when illuminating the III-nitride solar cell from substrate-side.
5. **Minimizing top contact coverage:** Reflection due to top contact metal can be reduced by minimizing its coverage area. This method, however, increases the series resistance of the solar cell due to increased resistance of thin metal fingers and

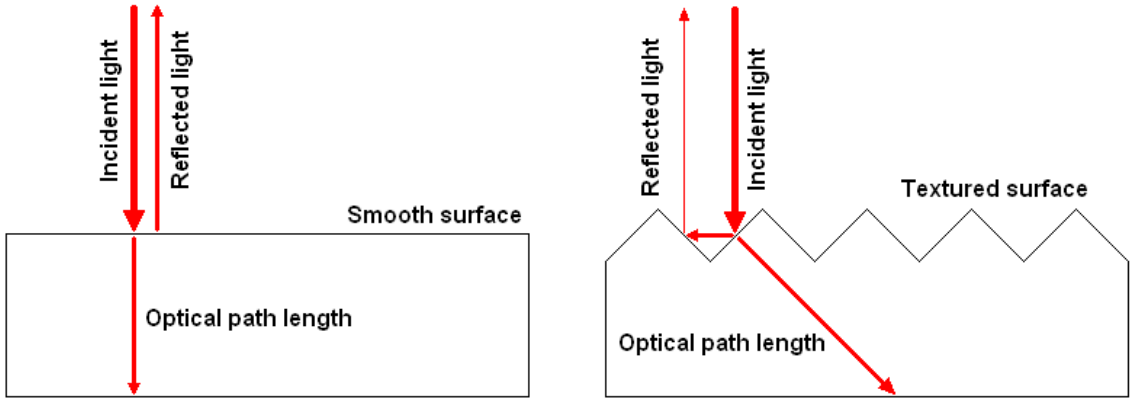

Figure 3.1: Geometrical comparison of (a) smooth surface, and (b) textured surface in solar cells indicating higher absorption for textured surface due to lower reflection and increase in optical path length.

busbars [84][85]. The buried-contact technology [34] is an innovative method to overcome this tradeoff, and similar methods can be investigated for the III-nitrides.

3.1.2 Collection efficiency

The minority carrier collection efficiency of a solar cell may decrease due to recombination of photogenerated carriers at the surface, in the junction or in the depletion region of the device. Recombination not only decreases the I_{SC} of the solar cell, but also decreases the open-circuit voltage (V_{OC}) due to increased leakage currents. While recombination is typically an artifact of material quality, this effect can be controlled in the final device using the following methods:

1. **Surface passivation:** Dangling bonds are formed at semiconductor surface due to unavailability of neighboring atoms to complete bonding in its outer shell. Such bonds act as recombination centers for minority carriers and hence, decrease the

collection efficiency of the solar cell. Typically, wide-band gap oxides or nitrides are formed or deposited on such surfaces to eliminate the dangling bonds [86]. However, oxides of gallium and indium spontaneously formed at the metal-semiconductor surface tend to increase contact resistance [87] and have to be addressed during fabrication of InGaN solar cells.

2. **Surface fields:** Front Surface Fields (FSF's) and Back Surface Fields (BSF's) can be formed at the semiconductor-metal interface by increasing the doping in the semiconductor near the surface. Such dopings not only reduce contact resistance, but also generate electric fields that repel minority carriers from the surface and prevent them from recombining at the surface as shown in Figure 3.2(a) [88]. The same principle can also be applied in InGaN solar cells by increasing the dopings close to p- and n-type surfaces.
3. **Band engineering:** A method similar to surface passivation is to deposit a wide-band gap semiconductor at the solar cell surface that bends bands to generate electric

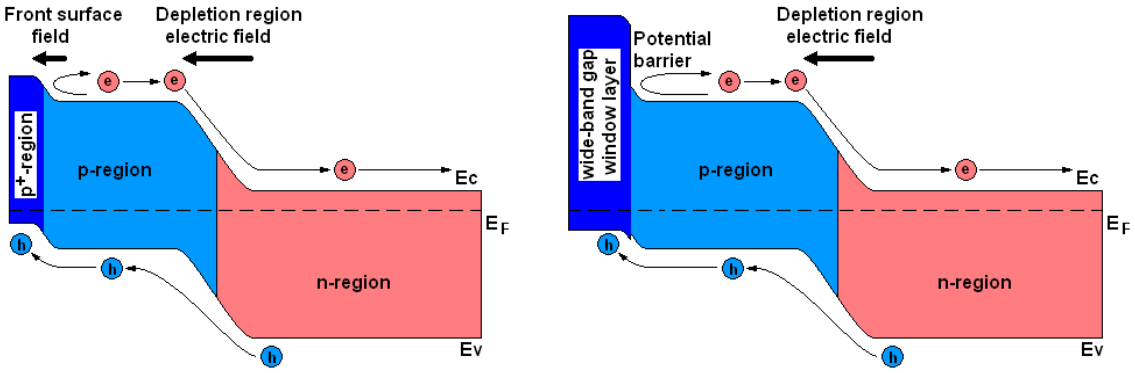

Figure 3.2: Role of (a) p+-region, and (b) window layer for generating front surface fields and passivation.

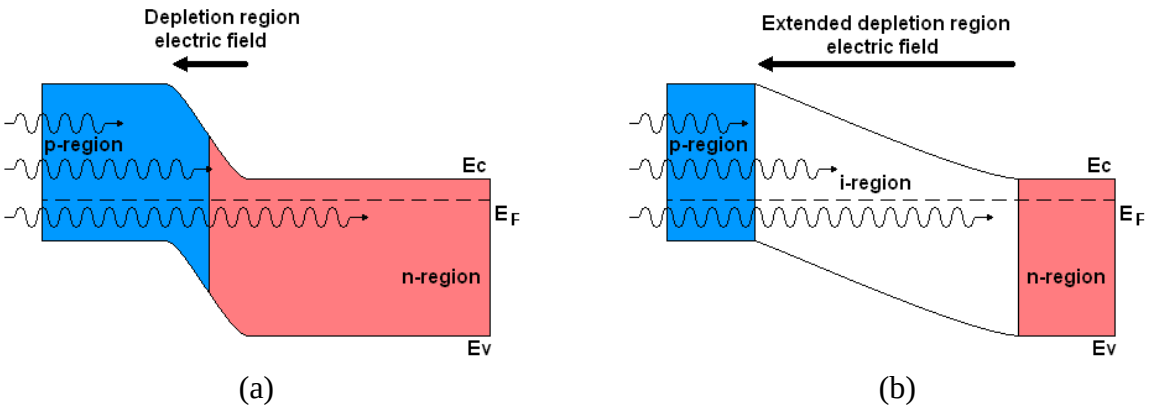

Figure 3.3: (a) A p-n solar cell compared to (b) a p-i-n solar cell illustrating extension of depletion region electric field.

fields. Such 'window layers', as shown in Figure 3.2(b), are widely used in III-V solar cell technology [44] due to relative ease of growth and advantages in fabrication. GaN and AlN window layers are investigated for their suitability for InGaN solar cells.

4. **Extending depletion region:** Photocarriers generated in the depletion region typically have a very high collection probability due to the presence of a high electric field. Hence, a solar cell can be designed to maximize absorption in the depletion region by increasing its thickness. This can practically be done by inserting an intrinsic i-region between the p- and n-junctions for InGaN and other semiconductors as shown in Figure 3.3, or grading the layer in terms of band gap or doping. However, it should be noted that an i-region of non-optimal thickness increases the series resistance of the solar cell.
5. **Gettering:** Crystalline imperfections such as point defects and dislocations are electrically active and act as recombination centers that decrease the collection

efficiency of the solar cell. Such defects can be passivated by bonding the incomplete bonds with hydrogen [89] through high-temperature annealing.

3.1.3 Open-circuit voltage

The recombination of minority carriers has a major influence on the V_{OC} of the solar cell as mentioned in the previous section. High recombination increases the forward-bias recombination current of the diode, which in turn decreases the V_{OC} of the solar cell. Hence, methods like surface and bulk passivation to decrease recombination are applicable to increase V_{OC} in addition to improving the I_{SC} of the solar cell. Another method to improve V_{OC} by reducing minority carrier recombination is by reducing the concentration of minority carriers itself. This is achieved by increasing the doping in junctions. Even though this method cannot be exploited directly in InGaN solar cells due technological limitations in doping, band engineering can be explored to increase the effective dopings at junction edges.

3.1.4 Resistance

The final condition to design a successful solar cell is to minimize parasitic resistive losses. While a low shunt resistance is typically caused due to processing error, series resistance is governed by junction resistance and contact design. Hence, it is desirable to increase junction doping not only to enhance the depletion region electric field, but also to increase junction conductivity. Contact resistance is typically reduced by increasing the dimensions and thickness of the busbars and contact fingers, and reducing finger spacing on the top surface of the solar cell. This, however, is done at the cost of increasing shading loss.

Innovative methods such as using Transparent Conducting Oxides (TCO's) and band engineering as explained in Section 2.4.4 are explored to overcome this tradeoff.

3.2 PRELIMINARY INGAN SOLAR CELL DESIGN

Preliminary InGaN solar cells are designed following a thorough study of III-nitride LED and photodetector structures due to their complementary functionality. A realistic range of material and device parameters as well as technological limitations become evident after close examination of such existing technologies. The test structures are then optimized using the design principles laid out for solar cells.

Due to the widespread use of p-i-n devices in III-nitrides, initial solar cells are formed as a p-i-n heterojunction diode, where an undoped test material is sandwiched between p-type and n-type GaN junctions. Due to the maturity in growth and fabrication of GaN junctions, the response of the test InGaN can be separated for that of the rest of the device during material and device characterization. The designed structures are modified to optimize light absorption instead of light emission as in LEDs; they are further optimized for carrier collection without any external bias unlike photodetectors that maximize carrier collection using an externally applied voltage. The p-type and n-type GaN junctions are consistently doped to obtain an acceptor carrier concentration of 5 x 10^{17} cm^{-3} and a donor concentration of 5 x 10^{18} cm^{-3}, respectively, to comply with optimized growth settings from previous LED experiments.

Literature indicates calculated [90] as well as measured [91][92] absorption coefficients as high as 10^5 cm^{-1} at the band edge for InGaN. For such values, the material absorbs more than 95% of the incident light within the first 300 nm and more than 99%

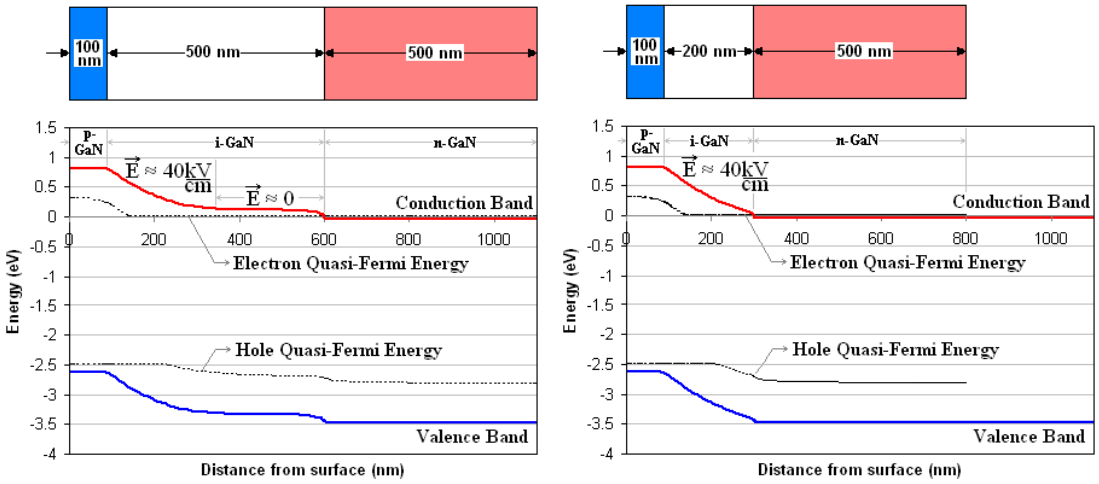

(a) (b)

Figure 3.4: Simulated band diagram of InGaN p-i-n solar cell with i-region thickness of (a) 500nm, and (b) thickness reduced to 200nm.

within the first 500 nm. Hence, the total thickness of the designed device is limited to 500 nm.

It seems intuitive to increase the thickness of the undoped InGaN region for maximum light absorption. On the other hand, an important design requirement is to maximize the electric field in this i-region to maximize the collection of photogenerated carriers. However, due to a background n-type concentration of 10^{16} cm^{-3} present in undoped III-nitrides, the electric field in the i-region is maintained only up to a certain distance from the p-GaN junction, after which, it effectively becomes zero. PC1D simulations of the device indicate that an effectively uniform electric field is maintained only within the first 200 nm of the i-region as shown in Figure 3.4(a). A 200 nm thick i-region yields an average electric field of about 40 kV/cm as shown in Figure 3.4(b). Hence, the thickness of the i-region of the test device is limited to 200 nm.

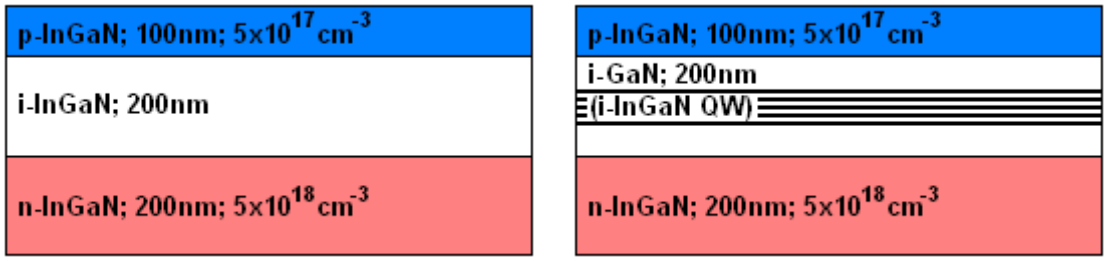

(a) (b)

Figure 3.5: Optimized structure of an InGaN (a) p-i-n solar cell, and (b) quantum-well solar cell.

Measured minority lifetimes up to 6.5ns for GaN have been reported [28][93], while electron and hole mobilities of 1000cm^2/V-s and 200cm^2/V-s have been calculated [94]. However, electron and hole respective mobilities of 400 cm^2/V-s and 10 cm^2/V-s had been achieved previously by samples grown in the lab with a recombination lifetime of 1-2ns. The calculated electron and hole diffusion lengths from these values are 1.44μm and 0.2μm respectively. The value of the hole diffusion length limits the thickness of the n-layer to 200nm, while there is enough leeway in the maximum thickness of the p-region. The p-region is intended to be as thin as possible to maximize absorption in the subsequent i-region, but at the same time be able to provide charge for the junction and the top metal contact. Hence, the thickness of the p-layer is restricted to 100nm. The resulting device structure is shown in Figure 3.5(a).

The test material can also be incorporated in the i-region in the form of a superlattice. Thin undoped InGaN layers can be grown alternating with undoped GaN layers in the i-region to ensure superior quality of the test material as they will be close to being pseudomorphic. Such structures are similar to quantum-well solar cells as shown in Figure 3.5(b).

3.3 SIMULATION OF INGAN SOLAR CELLS

The first step to checking the validity of the comprehensive design is through simulation. PC1D is a computer program written for IBM-compatible personal computers which solves the fully coupled nonlinear equations for the quasi-one-dimensional transport of electrons and holes in crystalline semiconductor devices, with emphasis on photovoltaic devices. While PC1D is typically used to model silicon, germanium and common III-V solar cells, it does not accommodate phenomena such as polarization, phase separation or Schottky contacts, which can potentially alter the performance of III-nitride solar cells. On the other hand, device modeling programs for the III-nitrides such as SiLENSe are typically designed for Light Emitting Diodes (LED's) and Laser Diodes (LD's) and do not incorporated absorption of incident spectrums. Since PC1D was first launched in 1985 to solve complete semiconductor device equations on a personal computer [95], it has undergone substantial improvements in terms of performance and capabilities. The emphasis in this program has been on reliable convergence for a broad range of doping profiles and boundary conditions. Its popularity is accredited to a user-friendly interface, versatility of feeding and extracting data, and an extensive comprehension of parameters to accurately model solar cells. Moreover, due to the accessibility to PC1D source code to further adapt it for III-nitrides, this program is used to pursue simulation of InGaN solar cells.

PC1D is modified to accurately model III-nitride solar cells in two steps:

1. **Development of III-nitride material files**, and

2. **Modification of PC1D source code** to incorporate unique phenomena such as polarization, which are not dominant in common semiconductors used for photovoltaics, and hence, not accommodated in PC1D. These phenomena and PC1D modifications are discussed in detail in Chapter 4.

3.3.1 PC1D files for III-nitrides

The first step to enable PC1D to simulate the III-nitrides is to develop database files associated with the relevant materials. The key files for PC1D consist of:

1. **Parameter file (*.prm):** This file contains information specific to the device design such as thickness of the device and junctions, doping profiles, lifetimes and recombination parameters. The parameter file calls material files associated to each material in the device.
2. **Material file (*.mat):** This file contain information about the electronic properties specific to the material such as band structure (band gap, electron affinity, etc.), intrinsic carrier concentrations, dielectric constant, carrier mobilities, and recombination parameters. The material files obtain optical information from the associated optical files.
3. Optical files: The following optical files are linked to the material files:
    a. **Absorption coefficient file (*.abs):** This file contains the absorption coefficient of the material as a function of incident photon wavelength.
    b. **Refractive index file (*.inr):** This file contains the refractive index of the material as a function of incident photon wavelength.

Details of the material files used for PC1D simulations are provided in Appendix A..

3.2.2 Simulation of test GaN/InGaN solar cell

The preliminary test GaN/InGaN device with an area of 1 cm^2 shown in Figure 3.6 is simulated in PC1D using the developed III-nitride material files. The thickness of the p-GaN, i-$In_{0.05}Ga_{0.95}N$ and n-GaN regions are fixed at 100 nm, 200 nm, and 500 nm, respectively. Uniform doping values for the p- and n- regions are set to 2 x 10^{17} cm^{-3} and 4 x 10^{18} cm^{-3}, respectively, while an n-type background impurity concentration in the i-region is set to 1 x 10^{16} cm^{-3}. The minority carrier lifetimes for all the materials are set to 2 ns, while the hole and electron mobilities are fixed at 10 $cm^2/V•s$ and 400 $cm^2/V•s$. The base resistance for this device is set to 0.015 Ω. The material files used for the simulation are also provided in Appendix A.

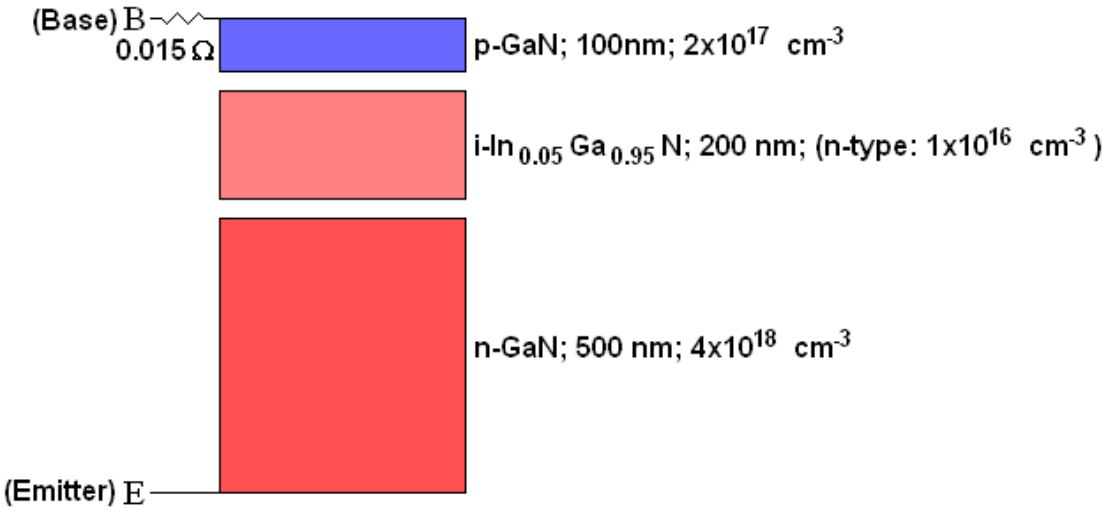

Figure 3.6: GaN/InGaN test device for PC1D.

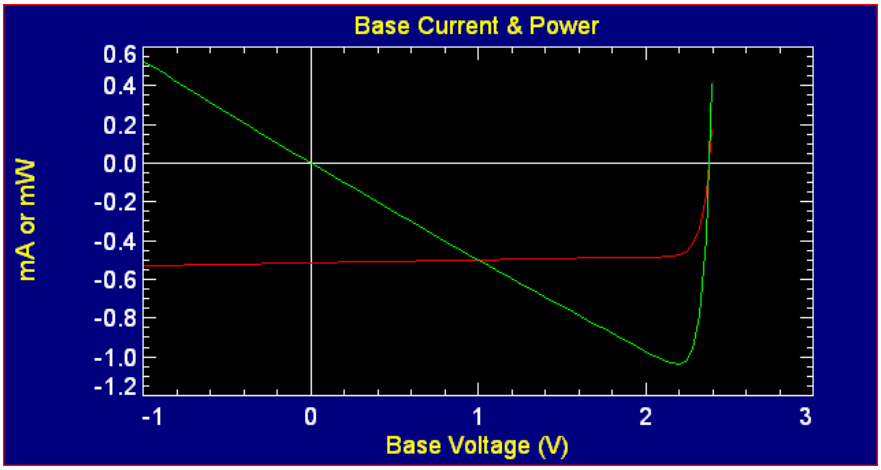

(a)

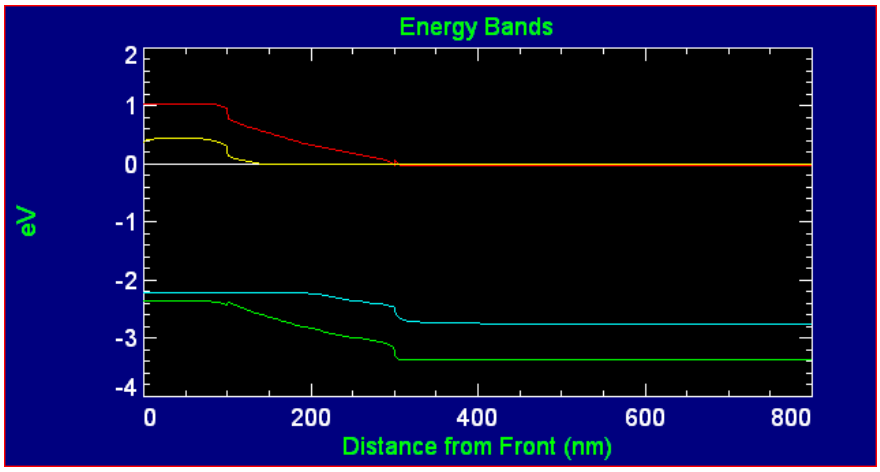

(b)

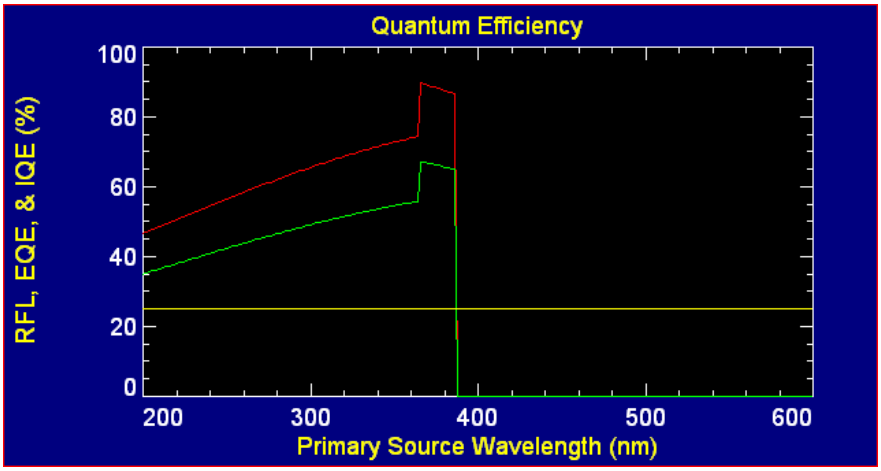

(c)

Figure 3.7: PC1D simulation results for test GaN/InGaN device indicating (a) I-V characteristics, (b) band diagram at maximum power, and (c) quantum efficiency.

The test device is simulated to obtain a Current-Voltage (I-V) response and as well as Quantum Efficiency (QE). The voltage for the I-V curve is swept from -1 V to 2.4 V, while the wavelength for QE simulation ranges from 200 nm to 600 nm.

The GaN/InGaN test device outputs a photovoltage with an expected V_{OC} of 2.378 V and I_{SC} of 0.514 mA. The Fill Factor (FF) of the test device is 85%, which results in a photovoltaic efficiency of 1.04%. Screenshots of the simulation results are provided in Figure 3.7. The Internal Quantum Efficiency (IQE) of carriers generated in the i-InGaN region is as high as 90%, while that of higher energy photons generated primarily in the top p-GaN region peaks at 74%. The main limitations in the performance these devices arise due to their limited minority carrier lifetimes. These simulation results provide a positive feedback to take the next step, i.e. to fabricate InGaN solar cells.

3.4 SUMMARY

General solar cell design principles are discussed, which involve maximizing photon absorption and photogenerated carrier collection while controlling dark currents and parasitic resistances. Initial GaN/InGaN test solar cells are designed based on such general design guidelines and technological limitations for the material. PC1D is used to simulate III-nitride solar cells by developing specific material files. Simulation of preliminary test GaN/InGaN devices yield encouraging results for III-nitrides as a successful photovoltaic material system. The accuracy of such simulations can further be improved by understanding and incorporating phenomena such as polarization in the program, which will be discussed in the next chapter.

4. POLARIZATION MODEL FOR InGaN SOLAR CELLS

4.1 THEORY OF POLARIZATION MODEL IN III-NITRIDES

One of the unique characteristics about the wurtzite III-nitrides is its polarization effects, which was only fully understood recently due to incomplete understanding of the polarization theory itself [96][97], as well as technological limitations in the III-nitrides to verify theoretical data [98][99]. Recent theoretical investigations have suggested that the macroscopic polarization in such III-nitrides has a major influence on the design criteria of heterojunctions and low dimensional nanostructures [15][100][101]. Some polarization constants are found to be up to ten times larger than in conventional III-V and II-VI semiconductor compounds, and comparable to those of ZnO [98]. The net polarization and consequent internal electric fields have been shown to be detrimental to the performance of optoelectronic devices [102]-[104]. Polarization discontinuities lead to potential barriers, band bending that can have undesired consequences on the device; electric fields with values as high as 1 MV/cm have been reported [105][106]. Polarization, however, can be utilized constructively by accommodating in the solar cell design to improve its performance. Thus, it becomes vital to successfully model this effect and incorporate it during device design.

Due to the unavailability of a suitable solar cell modeling program with polarization simulation capabilities, an in-house simulation model is developed. A detailed polarization sub-routine is incorporated into the source code of PC1D, which is a solar cell modeling

program typically used for silicon solar cells. The following subsections describe the detailed theory of polarization as incorporated in the polarization model.

4.1.1 Origin of polarization in the III-nitrides

Polarization is present in the III-nitrides as a consequence of the non-centrosymmetry of the wurtzite structure and the large ionicity of the covalent metal-nitrogen bonds. The GaN crystal exhibits two opposite sequences of atomic layering in the c-direction resulting in either a cation (Ga/In/Al)-face or an anion (N)-face GaN epitaxy.

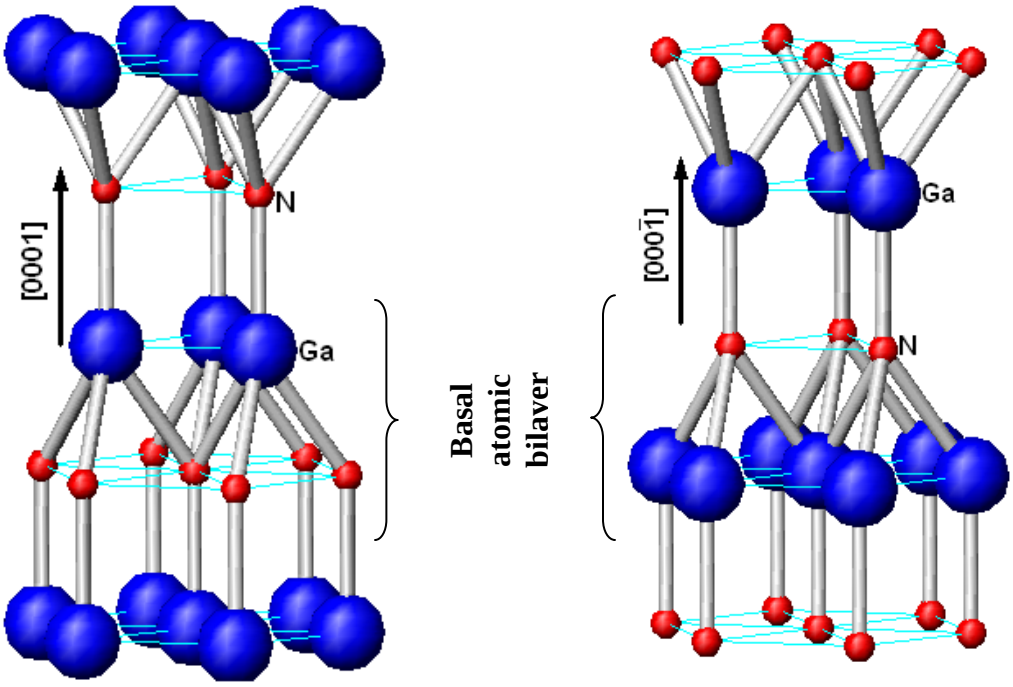

(a) (b)

Figure 4.1: (a) Ga-face, and (b) N-face GaN

In general, the, where the Ga cation can be replaced by In or Al. For simplicity, we will generalize the material as either Ga-face or N-face as shown in Figure 4.1. Ga-face GaN means that Ga is on the top position of the {0001} bilayer, corresponding to the [0001] polarity.

Polarization affects the semiconductor via the following equation:

$$\vec{D} = \in_o \in_r \vec{E} + \vec{P} \qquad \text{[Units: C/m}^2\text{]} \qquad \text{--- (4.1)}$$

where, $\vec{D}$ = Electric flux density (C/m^2),

$\vec{E}$ = Electric field (V/m),

$\vec{P}$ = Polarization (C/m^2)

Net polarization ($\vec{P}$) is composed of two parts:

i. Spontaneous polarization ($\vec{P}_{sp}$), which is intrinsic to the material, and

ii. Piezoelectric polarization ($\vec{P}_{pz}$), which is strain-induced.

$$\vec{P} = \vec{P}_{sp} + \vec{P}_{pz} \qquad \text{[Units: C/m}^2\text{]} \qquad \text{--- (4.2)}$$

4.1.2 Spontaneous polarization

Spontaneous polarization ($\vec{P}_{sp}$) exists due to the non-centrosymmetry of the crystal, where the crystal behaves like an electric dipole. In the III-nitrides, the direction of spontaneous polarization is from the N-atom to the closest metal atom, i.e. along the $\pm$c

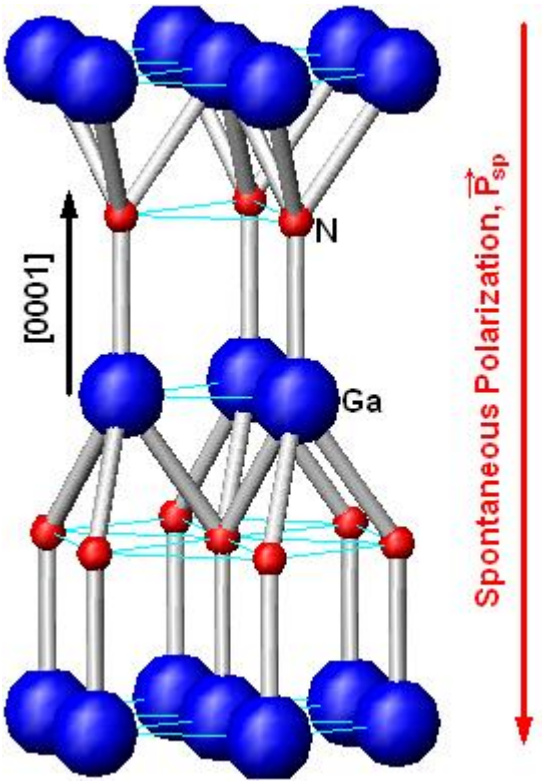

Figure 4.2: Direction of spontaneous polarization jn Ga-face GaN.

direction, which is also the typical MOCVD or MBE growth direction. Hence, in Ga-face GaN, spontaneous polarization is opposite to the [0001] direction, i.e. in the downward direction pointing towards the substrate as shown in Figure 4.2. Spontaneous polarization in ternary compounds can be calculated by interpolating the binary compounds using a bowing factor 'b' as shown in Equation 4.3.

$$P_{sp}^{ABN}(x) = P_{sp}^{AN}(x) + P_{sp}^{BN}(1-x) + bx(1-x) \qquad \text{[Units: C/m}^2\text{]} \qquad \text{--- (4.3)}$$

The spontaneous polarization coefficients for III-nitrides are summarized in Table 4.1 [107]. Note that the negative sign indicates polarization in the $[\bar{1}000]$ direction.

Table 4.1: Spontaneous polarization coefficients in III-nitrides.

Material	Spontaneous Polarization (C/m^2)
AlN	-0.09
GaN	-0.034
InN	-0.042
$Al_XGa_{1-X}N$	- 0.090x – 0.034(1-x) + 0.021x(1-x)
$In_XGa_{1-X}N$	- 0.042x – 0.034(1-x) + 0.037x(1-x)
$Al_XIn_{1-X}N$	- 0.090x – 0.042(1-x) + 0.070x(1-x)

Spontaneous polarization manifests itself at semiconductor surfaces or heterostructure interfaces by forming electric fields and accumulating a charge density equivalent to the difference in polarization coefficients of the respective surfaces.

4.1.3 Strain model and piezoelectric polarization

The direction of piezoelectric polarization is dependent on the polarity of the material as well as on the strain. Spontaneous and piezoelectric polarizations are parallel and add to each other when planar strain (perpendicular to c-axis) is tensile and are anti-parallel when planar strain is compressive.

In a perfectly pseudomorphic growth, the epilayer undergoes strain and assumes the lattice constant of its substrate. If the lattice constant 'a' of the epilayer is a_e and lattice constant of the substrate is a_s, then assuming a pseudomorphic epitaxial growth where the lattice constant of the substrate does not change, the strain in the epitaxial layer along the a-plane, ε, is given by:

$$\varepsilon = \frac{a_s - a_e}{a_e} \qquad \text{[Units: None]} \qquad \text{--- (4.4)}$$

It is assumed that the substrate does not deform due to strain arising from the epitaxial layer. Hence, only the first degree strain arising in the epitaxial layer is taken into account.

In practical scenarios, the epitaxy may not be pseudomorphic and there would be relaxation in the epitaxial layers. In that case, the epilayer at the interface would assume a lattice constant somewhere between its own original value and that of the substrate depending on the degree of relaxation. Thus, the calculation of piezoelectric polarization requires an additional strain relaxation model at the interfaces of active epitaxial layers of the solar cell. If the new strained lattice constant of GaN at the interface is a'_e, then the strain at this interface along the a-plane is given as:

$$\varepsilon_x = \frac{a'_e - a_e}{a_e} = \frac{a_s - a_e}{a_e}(1 - R) \qquad \text{[Units: None]} \qquad \text{--- (4.5)}$$

where, R = Relaxation Factor, $0 < R < 1$

For an ideal pseudomorphic case ($a'_e = a_s$) R = 0, while for a completely relaxed epilayer, R = 1, and strain at the interface is zero ($\varepsilon_x = 0$). This relaxation factor can be determined experimentally. The resultant strain in GaN at the interface in z-direction is given by:

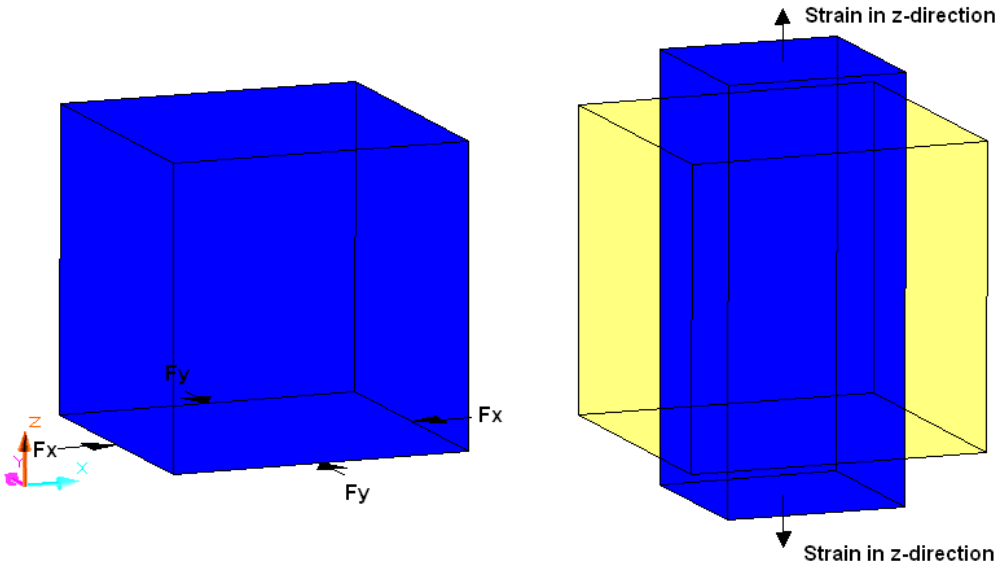

Figure 4.3: Schematic representation of (a) biaxial strain in the basal plane on a crystal, and (b) resultant deformation.

$$\varepsilon_z = -2\left(\frac{C_{13}}{C_{33}}\right)\varepsilon_x \qquad \text{[Units: None]} \qquad \text{--- (4.6)}$$

where, C_{13} and C_{33} are elastic coefficients.

Note that the '2' is present in the equation because strain in the basal plane is biaxial and $\varepsilon_x = \varepsilon_y$ as illustrated in Figure 4.3.

There is also a gradual exponential strain-relaxation profile along the thickness of the epitaxial layer, which determines the piezoelectric polarization within the bulk of the material. The strain decays exponentially along the thickness of the epitaxial material with respect to the z-direction at a rate corresponding to the Strain Relaxation Constant (RC). This RC is specific to the material as well as the conditions under which it was grown.

$$\varepsilon_z(z) = \varepsilon_{z,z=0} e^{-\frac{z}{RC}} \qquad \text{[Units: None]} \qquad \text{--- (4.7)}$$

where, $\varepsilon_z(z)$ = strain in GaN in the z-direction as a function of distance (z) from the interface,

$\varepsilon_{z,z=0}$ = strain in GaN in z-direction at the interface,

RC = strain Relaxation Coefficient, μm

A sample strain relaxation profile of a GaN epilayer on AlN along the c-direction is shown in Figure 4.4, where (a) the epitaxy is pseudomorphic, i.e. there is no relaxation at the interface, and (b) the epitaxial GaN relaxes by 95% at the AlN interface.

The nonvanishing component of piezoelectric polarization caused by biaxial strain is along the c-axis, and is given by:

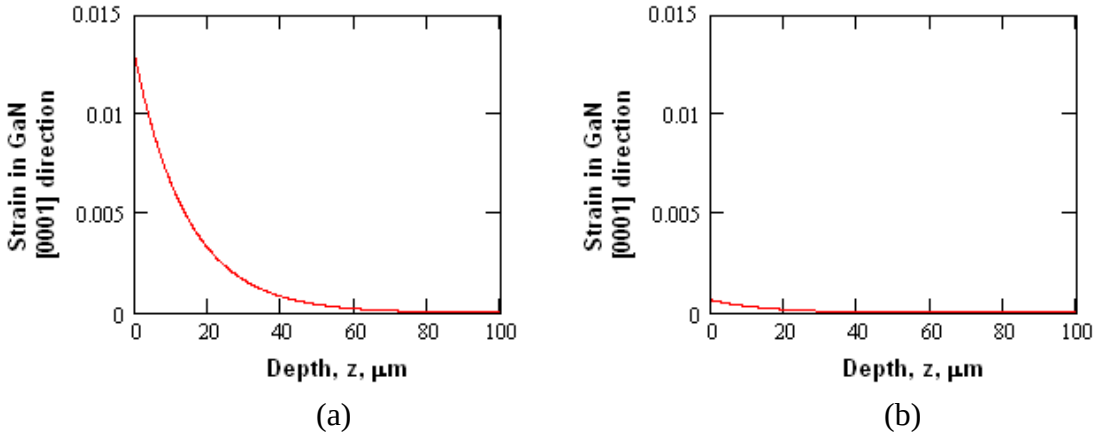

Figure 4.4: Strain relaxation profile of GaN on AlN template for (a) perfectly pseudomorphic epilayer, and (b) epilayer relaxed by 95%

$$P_{pz} = \varepsilon_x e_{31} + \varepsilon_y e_{32} + \varepsilon_z e_{33} \qquad \text{[Units: C/m}^2\text{]} \qquad \text{--- (4.8)}$$

where, $\varepsilon_x, \varepsilon_y, \varepsilon_z$ are strain components in the x, y, z direction,

e_{31}, e_{32}, e_{33} are piezoelectric constants (Table 4.2).

For the III-nitrides, $\varepsilon_x = \varepsilon_y$ and $e_{31} = e_{32}$. Hence, from Equations (4.6) and (4.8),

$$P_{pz} = 2\varepsilon_x \left(e_{31} - e_{33} \frac{C_{13}}{C_{33}} \right) \qquad \text{[Units: C/m}^2\text{]} \qquad \text{--- (4.9)}$$

Table 4.2: Coefficients pertaining to piezoelectric polarization III-nitrides.

	InN	**GaN**	**AlN**
Lattice Const, a (Å)	3.533	3.189	3.112
Lattice Const, c (Å)	5.693	5.186	4.982
Elastic Const, C_{13} (GPa)	92	103	108
Elastic Const, C_{33} (GPa)	224	405	373
Piezoelectric Const, e_{31} (C/m^2)	-0.57	-0.49	-0.60
Piezoelectric Const, e_{33} (C/m^2)	0.97	0.73	1.46

4.1.4 Effect of net polarization

The polarization-induced charge density with a gradient of polarization in space is given by:

$$\sigma_P = -\nabla P \qquad \text{[Units: C/m}^2\text{]} \qquad \text{--- (4.10)}$$

By analogy, the fixed charge density at an abrupt hetero-interface is given by:

$$\sigma_P = P(bottom) - P(top) \qquad \text{--- (4.11)}$$

$$= \{P_{sp}(bottom) + P_{pz}(bottom)\} - \{P_{sp}(top) + P_{pz}(top)\} \qquad \text{--- (4.12)}$$

This charge density induces an additional polarization-induced electric field component in the semiconductor. At low bias voltages, which are typical for solar cell operation, the polarization-induced surface carrier concentration, n_s, at a hetero-interface can be approximated as:

$$n_s = \frac{\sigma_P}{e} \qquad [\text{Units: } /\text{m}^2] \qquad \text{--- (4.13)}$$

This polarization-induced charge density or electric field is used as the starting point for the PC1D solving routine at a given hetero-interface. If the charge density at a hetero-interface is positive, it will tend to accumulate a 2-Dimensional Electron Gas (2DEG); similarly, a negative hetero-interface charge density will tend to form a 2-Dimensional Hole Gas (2DHG).

4.2 IMPLEMENTATION OF POLARIZATION IN PC1D

4.2.1 PC1D solver method

PC1D calculations are primarily based on the one-dimensional drift-diffusion model used for charge transport in semiconductors. PC1D solves fully coupled nonlinear

equations for the quasi-one-dimensional transport of electrons and holes in crystalline semiconductor devices, with emphasis on photovoltaic devices.

PC1D makes use of the finite-element method [108] approach to obtain rapid, accurate solutions of the semiconductor transport equations. The finite-element method used in PC1D calculates the numerical solution of the semiconductor equations by discretization of the device, both in time and space. The quasi-one dimensional model divides the device spatially into a finite set of 'M' elements along a solution dimension 'x', which typically follows the direction of current flow in the device. The dividing point between any two elements is called a node. The nodes are numbered from zero at the left boundary to M at the right. At each of the internal nodes, the three simultaneous non-linear equations (Poisson's equation and the electron and hole current transport equations) are solved for three solution variables: electrostatic potential (ψ), and the electron (φ_n) and hole quasi-fermi potentials (φ_p). Moreover, three equations are added at each boundary, which are based on (1) injected current density, (2) surface recombination, and (3) surface electrostatic potential. Hence, for M elements, there are a total of 3(M+1) equations for 3(M+1) unknowns.

These non-linear equations are solved using Newton's method [109], which iteratively solves a sequence of linearized approximations of the equations. A Jacobian matrix is generated using the derivatives of each equation in terms of ψ, φ_n and φ_p, each normalized by kT/q. At the end of each iteration, the solution variables ψ, φ_n and φ_p are updated. The iterations continue until a solution is reached; however, a convergence error is stated if the maximum change in these variables is greater than the user-supplied normalized error limit.

4.2.2 Incorporation of polarization parameters

A custom dialogue box is developed to input the polarization parameters into PC1D as shown in Figure 4.5 to make it user-friendly. This dialogue box can be accessed (1) by clicking on the 'Polarization Model Disabled' line in the 'Parameter View', (2) by selecting 'polarization…' under the 'Device' tab of the command bar, or (3) directly through the toolbar.

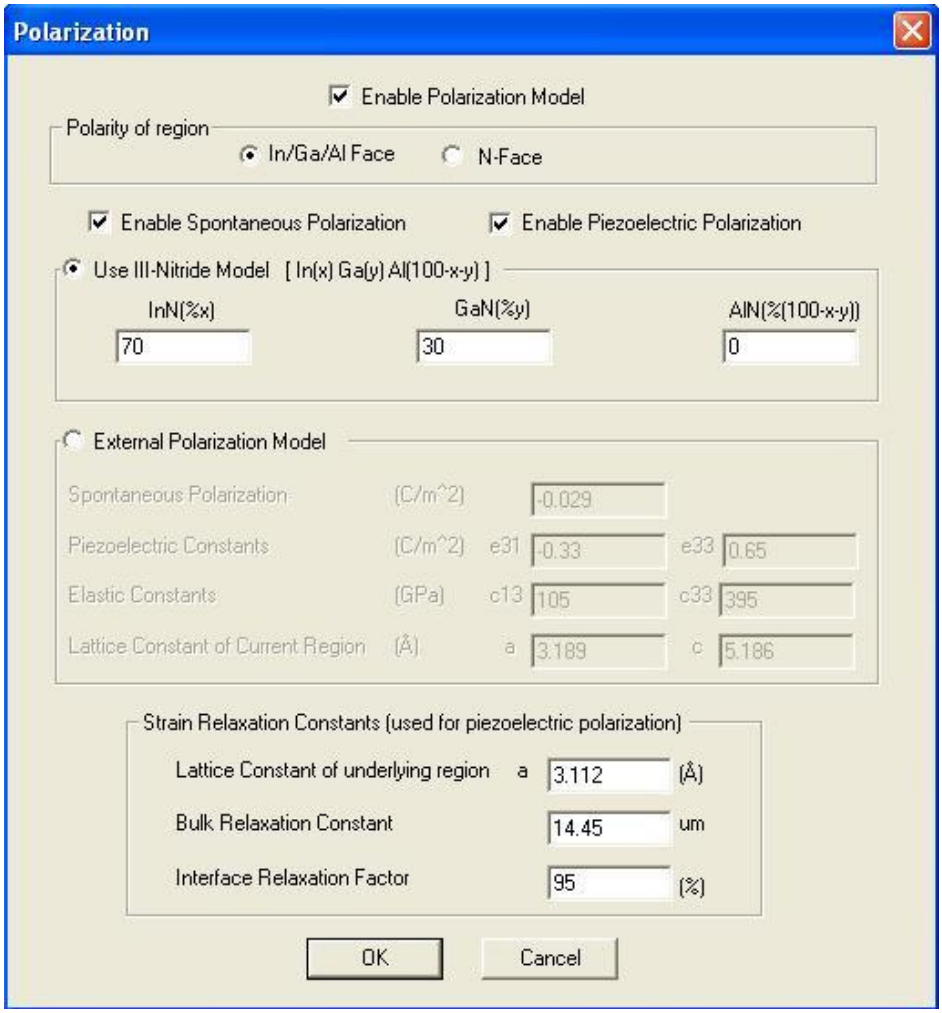

Figure 4.5: Polarization parameters dialogue box.

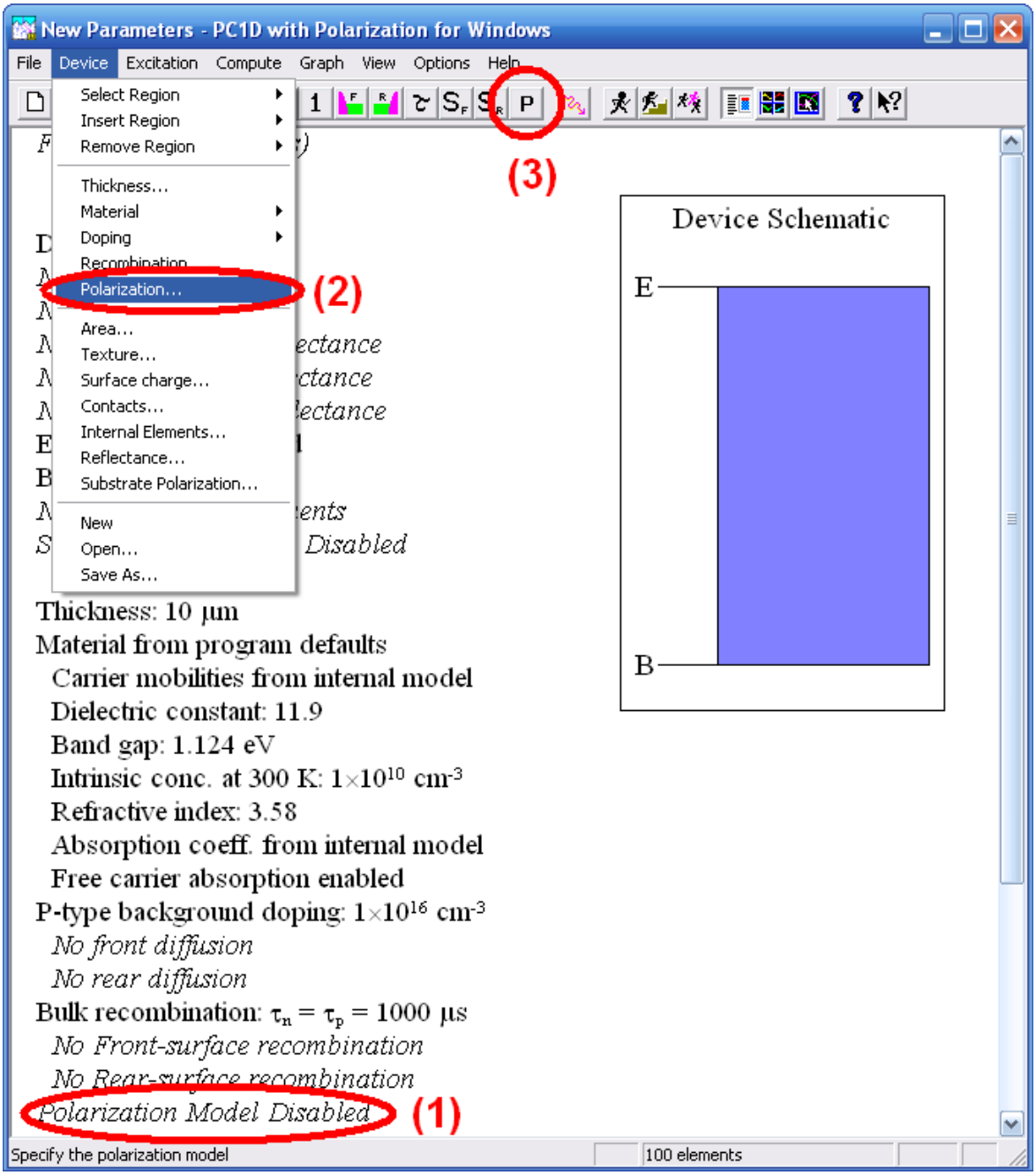

Figure 4.6: PC1D user interface identifying the three methods to access polarization model : (1) by clicking on the 'Polarization Model Disabled' line in the 'Parameter View', (2) by selecting 'polarization…' under the 'Device' tab of the command bar, or (3) directly through the toolbar.

The polarization parameters are specific to each layer or 'region' of test structure for simulation. The first option provided in this box is to enable the polarization model, as it turned off by default. Next, the polarity of the material is to be selected. The options of simulating either spontaneous, piezoelectric or both types of polarization are selected by enabling the respective check-boxes. Polarization parameters are fed into the program using either the internal model for the III-nitrides by selecting the compositions of indium, gallium and aluminum; or alternatively, they are entered manually, which avails this polarization model for other materials. In addition to the standard polarization constants, which include spontaneous, piezoelectric, elastic and lattice constants, additional constants specific to the strain relaxation model are also used. The strain profile within the [0001] direction of the region is determined using the lattice constant of the underlying region, interface relaxation factor and the bulk relaxation constant.

4.2.3 Modification of PC1D solver routine

Once the polarization and other regular parameters for each region are defined by the user, the next step is to incorporate these polarization parameters in the existing PC1D solver routine. As soon as the user clicks the 'Run' button to simulate the device, the polarization subroutine is initiated, where a profile of the gradient of strain is generated throughout the thickness of the device. This, in turn, calculates the polarization charge density throughout the thickness of the device as well as at all heterointerfaces. The polarization charge density is then discretized for each 'M+1' nodes, and added into the Poisson's equation for that node. This equation is then simultaneously solved with the electron and hole transport equations in the regular PC1D manner.

Thus, the polarization model is incorporated into PC1D at a source code-level. This modified PC1D is then used to test the effects of spontaneous and piezoelectric polarization on III-nitride structures and aid in further design of the solar cells.

4.3 SOME IMPORTANT POLARIZATION RESULTS

Potential barriers formed at hetero-interfaces impede carrier transport, lowering the collection efficiency, and thus, decrease the overall performance of the solar cell. Accumulation of 2DEG's and 2DHG's resulting from modulation doping tends to form triangular quantum wells with associated quasi fermi levels that act as carrier recombination centers The charge densities and electric fields generated due to polarization can either magnify such effects or reverse them due to their relatively high magnitude. Hence, it becomes vital to adjust the device design to ensure a positive influence of polarization on efficiency. Two realistic instances of InGaN solar cell design are investigated for influence of polarization in the following subsections.

4.3.1 Spontaneous polarization in InGaN/GaN p-i-n solar cell

The p-i-n InGaN/GaN design is a very basic solar cell design to test an InGaN material for its photoresponse. Such device structures are similar to those in other III-nitride optoelectronic devices, and offer an advantage due to the relative maturity of GaN technology compared to that of InGaN in terms of material quality, doping and Ohmic contacts. In this design, a 200 nm thick undoped test InGaN is sandwiched between 100nm p-type and 500nm n-type GaN as shown in Figure 4.7(a). The assumed direction of epitaxy is along the +c axis and the orientation of the crystal is Ga-face. Two cases, with and

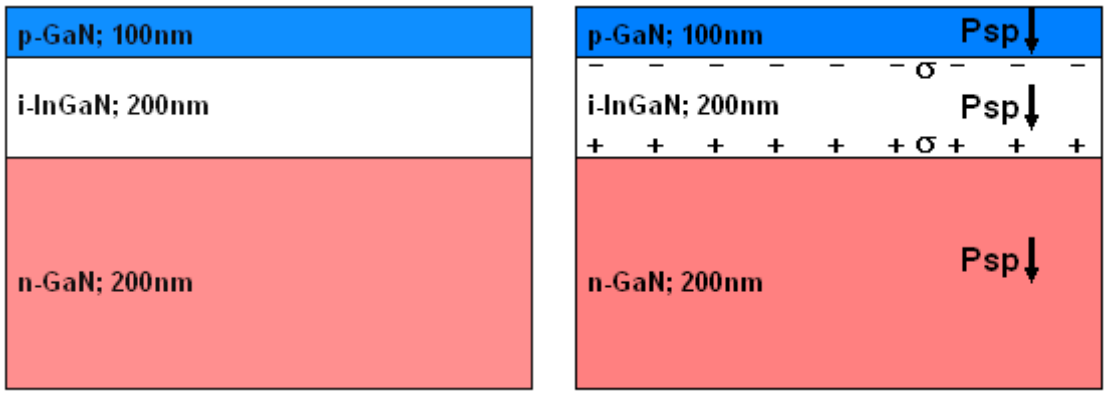

Figure 4.7: GaN/InGaN p-i-n test structure (a) without and (b) with spontaneous polarization effects.

without the effect of spontaneous polarization, are simulated to understand the impact on charge transport. Piezoelectric polarization is neglected under the assumption that thick epilayers, where the thickness is in the order of hundreds of nanometers, are completely relaxed, and hence, no strain is present.

The spontaneous polarization, which is in the downward direction, induces a sheet charge density at the InGaN/GaN interface as shown in Figure 4.7(b). The difference in spontaneous polarization of InGaN and GaN induces a negative sheet charge at the p-GaN/u-InGaN interface and a positive sheet charge at the u-InGaN/n-GaN interface. Each of these interfaces is simulated individually in the modified PC1D software for the two cases, with and without polarization, and their band diagrams, junction electric fields and carrier densities are studied.

Figure 4.8 compares a non-polar p-GaN/u-InGaN interface to one with spontaneous polarization. Theoretical calculations indicate that the difference in spontaneous polarization constants of GaN (-0.029 C/m^2) and $In_{0.2}Ga_{0.8}N$ (-0.0296 C/m^2)

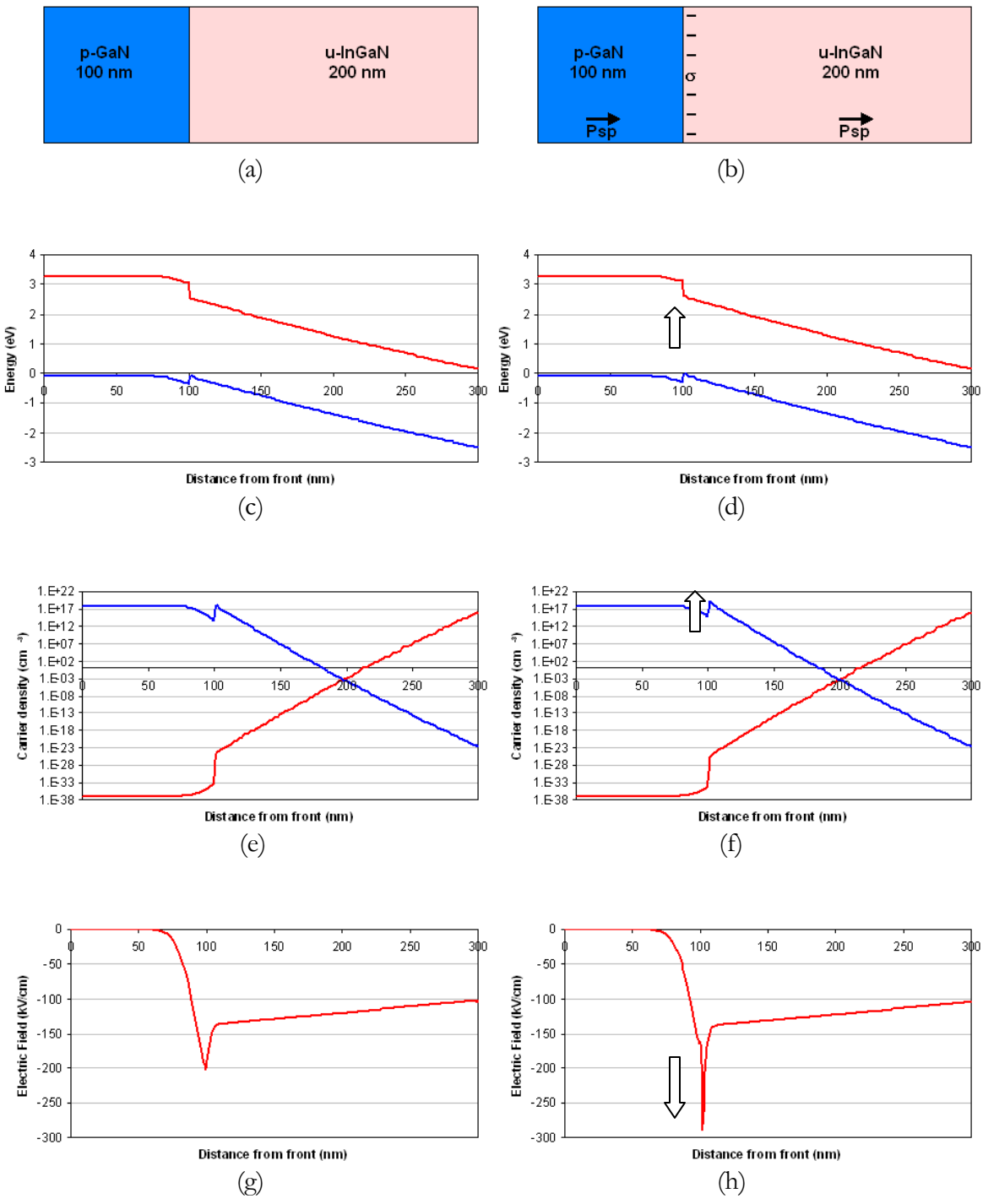

Figure 4.8: Comparison of p-GaN/u-InGaN interface for two cases, (a) without, and (b) with spontaneous polarization through their (c) and (d) band structures, (e) and (f) carrier densities, and (g) and (h) electric fields at zero bias calculated using the modified PC1D software.

will cause a negative sheet charge density of 6 x 10^{-8} C/cm^2. This negative sheet charge will cause an accumulation of holes and form a 2DHG at the interface bending the bands upwards. This upward band bending is observed in Figure 4.8(d), but is very weak due to the relatively small difference in spontaneous polarizations of GaN and $In_{0.2}Ga_{0.8}N$. A slight increase in hole density is also seen at the interface as shown in Figure 4.8(f). Figure 4.8(h) indicates the trend in electric field with increasing spontaneous polarization of InGaN. Here, the direction of the polarization-induced electric field, which is seen as an additional spike, is in the direction of the junction electric field, and hence, aids to the collection of carriers.

Similarly, Figure 4.9 compares the simulation results of non-polar p-GaN/u-InGan interface to one with spontaneous polarization. Again, theoretical calculations indicate that the difference in spontaneous polarization constants of $In_{0.2}Ga_{0.8}N$ (-0.0296 C/m^2) and GaN (-0.029 C/m^2) will cause a positive sheet charge density of 6 x 10^{-8} C/cm^2. This positive sheet charge will cause an accumulation of electrons and form a 2DEG at the interface bending the bands downwards. This downward band bending is observed in Figure 4.9(d), but is very weak due to the relatively small difference in spontaneous polarizations of GaN and $In_{0.2}Ga_{0.8}N$. A slight increase in electron density is also seen at the interface as shown in Figure 4.9(f). Figure 4.9(h) indicates the trend in electric field with increasing spontaneous polarization of InGaN. Here, again, the direction of the polarization-induced electric field, which is seen as an additional spike, is in the direction of the junction electric field, and hence, aids to the collection of carriers.

Simulation results of both the junction interfaces of the InGaN/GaN p-i-n solar cell indicate that spontaneous polarization aids to the transport of carriers through the i-region, and hence, will improve the collection efficiency of the solar cell. Even though the band gap of InGaN decreases with increasing indium compositions and the potential barrier to cross

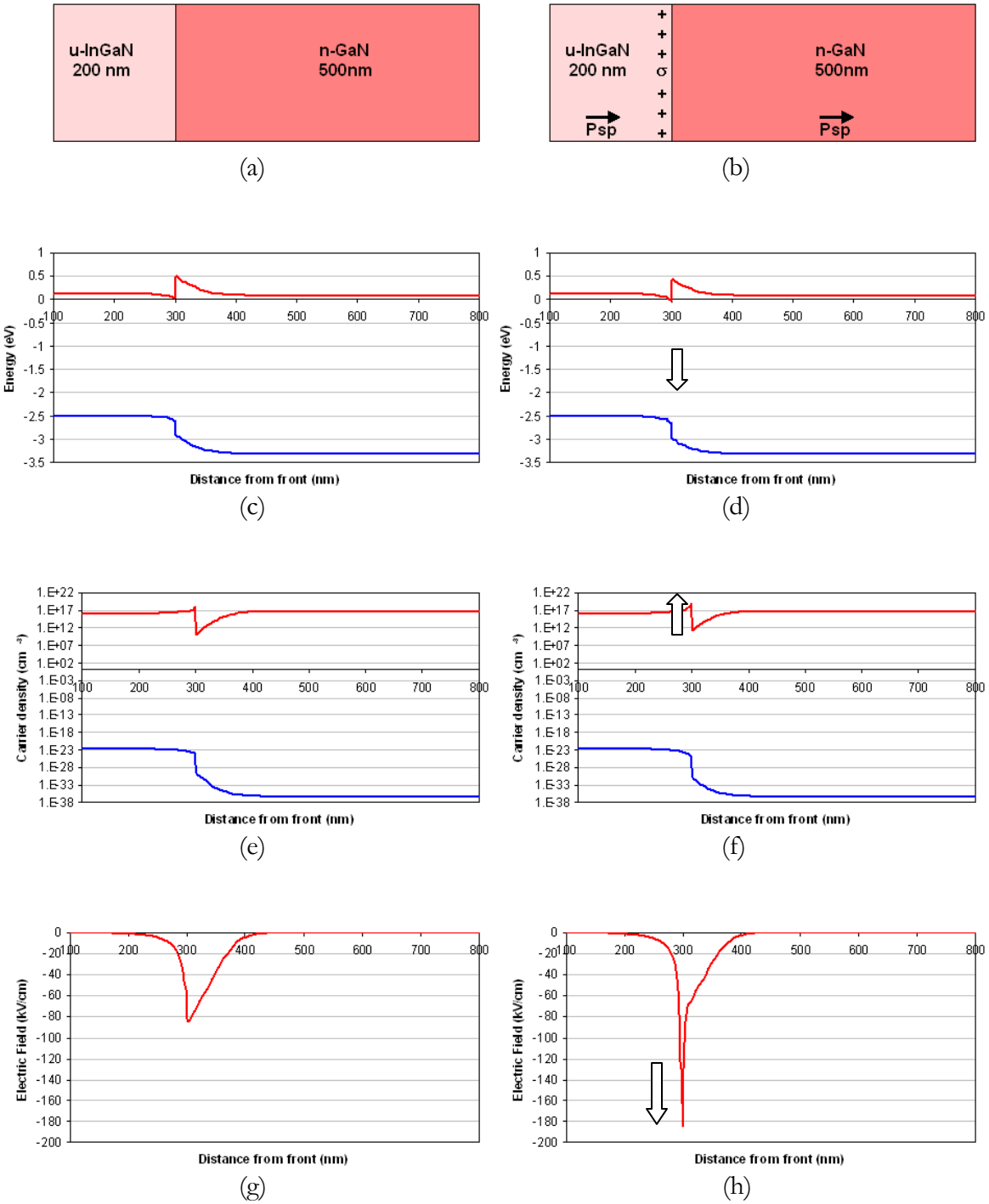

Figure 4.9: Comparison of u-InGaN/n-GaN interface for two cases, (a) without, and (b) with spontaneous polarization through their (c) and (d) band structures, (e) and (f) carrier densities, and (g) and (h) electric fields at zero bias calculated using the modified PC1D software.

from the u-InGaN to the GaN junction increases, spontaneous polarization tends to counter this effect by increasing the electric field at the junctions. Thus, spontaneous polarization should have a constructive effect on the performance of the InGaN/GaN p-i-n solar cell.

4.3.2 Piezoelectric polarization in GaN window layers

A higher band gap window layer is typically used in III-V solar cells to passivate the top surface [110] and generate a front-surface field [111] to minimize Front Surface Recombination (FSR). Hence, for a solar cell with a p-type InGaN junction at the top, it is intuitive to use a thin p-type GaN window layer as shown in Figure 4.10. However, thin GaN window layers, designed at an estimated thickness of 2 – 10 nm, may generate substantial piezoelectric polarization arising from strain due to lattice mismatch with the underlying p-InGaN layer. This polarization may generate fields that can potentially dominate the collection characteristics of the solar cell. Hence, it is important to study the effects of strained window layers in InGaN solar cells.

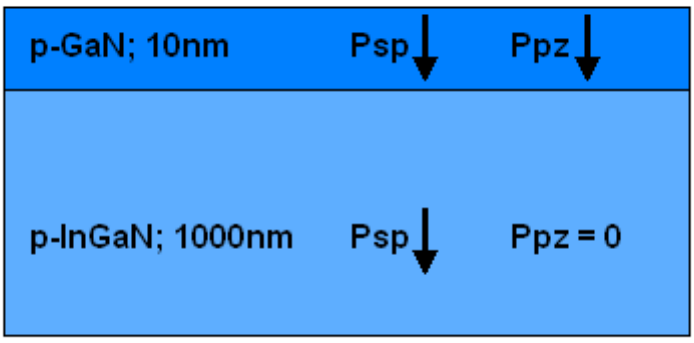

Figure 4.10: Schematic of a p-InGaN layer with a strained p-GaN cap layer indicating the direction of spontaneous and piezoelectric polarization.

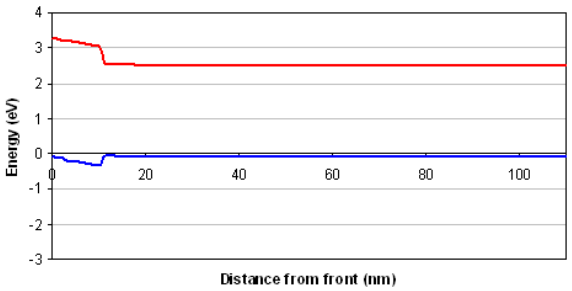

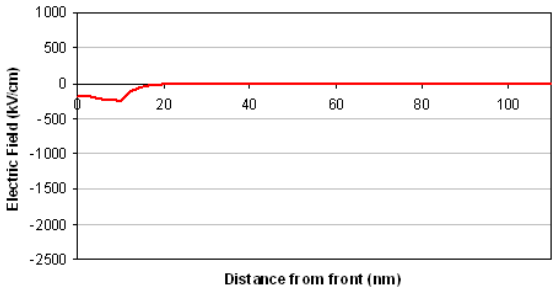

No polarization: (a) (b)

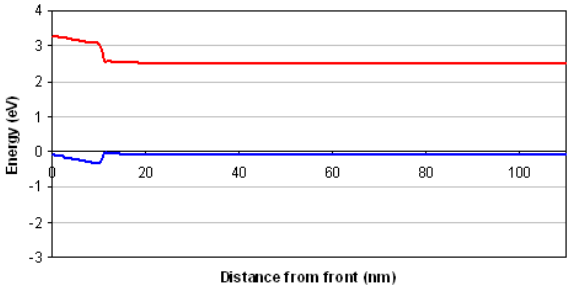

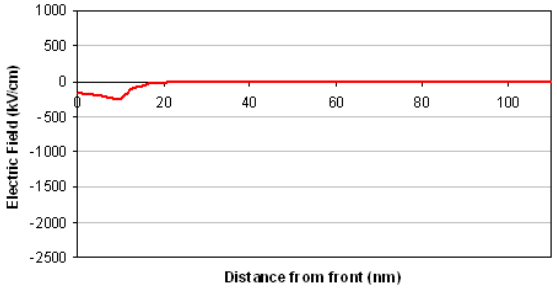

100% relaxed p-GaN: (c) (d)

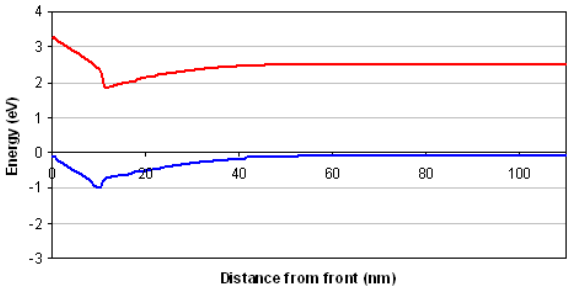

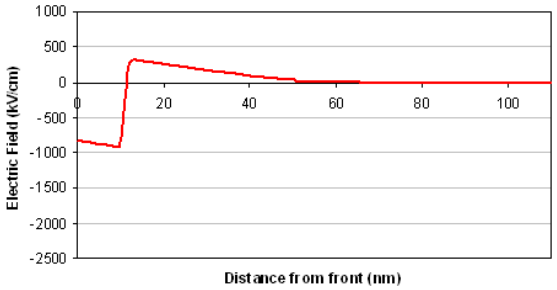

50% relaxed p-GaN: (e) (f)

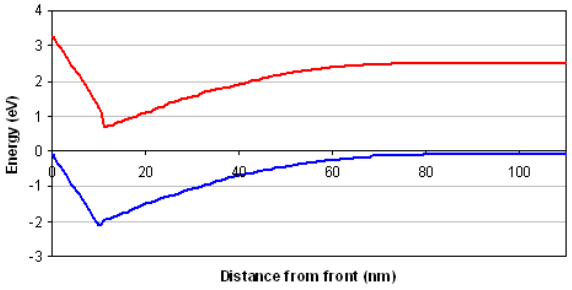

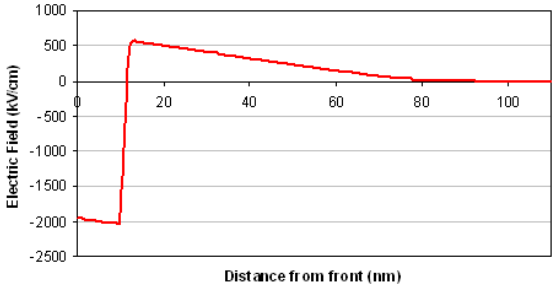

0% relaxed p-GaN: (g) (h)

Figure 4.11: Energy band and electric field diagram for p-GaN/p-InGaN heterostructure for p-GaN layer under variable strain relaxation.

A c-face p-InGaN/p-GaN heterojunction is simulated in the modified PC1D software to examine the behavior of the junction for variable degrees of strain relaxation in the p-GaN layer. The band diagrams and electric fields of this heterojunction are as shown in Figure 4.11; the cases considered are (a) without polarization, (b) 100% relaxed p-GaN, where piezoelectric polarization is zero and only spontaneous polarization is present, (c) 50% relaxed p-GaN, and (d) 0% relaxation, i.e. pseudomorphic case.

Comparing the band diagrams and electric fields for cases without polarization and without any strain (100% relaxed case), the structures functionally look similar as the spontaneous polarization-induced charge is very weak for this heterostructure. However, as strain in the p-GaN cap layer is increased, its piezoelectric component starts to dominate. As the p-GaN experiences biaxial tensile strain in the a-plane, the induced piezoelectric polarization points in the downward direction, i.e. – c direction, forming a positive sheet charge at the heterointerface. As a result, there is a formation of a 2DEG inducing an n-type junction at the heterointerface. As seen in Figures 4.11(f) and 4.11(h), the electric field developed in the p-InGaN opposes the transport of holes from p-InGaN to p-GaN.

Thus, a strained p-GaN cap layer may prove to be detrimental to the performance of an InGaN solar cell. This strain can be reduced by increasing the thickness of the p-GaN cap layer. Conversely, this strain induced n-type junction can be taken advantage of by using it to form a tunnel junction by replacing the thin p-type GaN cap layer with a thin n-type GaN cap layer, which will be investigated later.

4.4 SUMMARY

Thus, polarization is an important phenomenon that should be considered while designing III-nitride optoelectronic devices. The origin and effect of spontaneous and piezoelectric polarizations are discussed theoretically. A model for polarization is incorporated into the PC1D simulation program at the source code-level for accurate simulation of III-nitride solar cells and other materials where this phenomenon may alter transport characteristics of the device. Preliminary test simulations indicate that polarization fields induced due to spontaneous polarization at GaN/InGaN interfaces, even though marginal, aid carrier transport to improve the performance of conventional p-i-n InGaN/GaN solar cells. Moreover, strain in capping layers induces piezoelectric polarization, which may dominate over the effect of spontaneous polarization and have detrimental consequences on device performance. However, slight modifications can be made to the device design to constructively use the strong charge and inversions caused by piezoelectric polarization in InGaN solar cells. These polarization-oriented simulations provide additional design considerations before moving on to the next stage of InGaN solar cell development– growth and fabrication.

5. EPITAXIAL GROWTH AND FABRICATION OF InGaN SOLAR CELLS

The III-nitride material system poses practical challenges such as material crystallinity and defects, phase separation, p-type doping, Ohmic contacts, and grid design, as discussed in Chapter 2. It is important to understand and overcome these challenges individually before integrating the aspects to simplify the overall development of the solar cell. These challenges can be classified under two general topics, which are (1) epitaxial growth, and (2) device fabrication.

Metalorganic Chemical Vapor Deposition (MOCVD) is the most commonly used technique for growing III-V semiconductor based Light Emitting Diodes (LED's), Laser Diodes (LD's), photodetectors and solar cells. Consequently, most of the III-nitride based commercial devices are also grown by MOCVD. GaN is the most extensively studied material and has matured the most so far among the III-nitrides, while the lower band gap InGaN, which is more useful for photovoltaic application, it still a topic of fundamental research. Increasing the indium composition in InGaN during growth poses many challenges in controlling defect density, phase separation, and achieving p-type doping. Thus, a fundamental study of the growth of InGaN is carried out to yield high quality material suitable for optoelectronic applications.

In addition to growth, InGaN also demands a novel fabrication technique as typical fabrication schemes used in GaN-based LED's may not apply. The fabrication scheme of

InGaN solar cells involve grid patterns to maximize the light entering the device contrary to GaN-based LED's, where the entire top surface is covered by a current spreading contact and cause substantial shading. However, the high resistivity of p-type InGaN restrains the optimal grid spacing to result into about 50% shading. Moreover, challenges such as formation of Ohmic contacts have to be considered well in advance and overlap with the basic design and growth of the solar cell.

5.1 MOCVD GROWTH OF GaN TEMPLATES

5.1.1 MOCVD growth apparatus

The growths for InGaN solar cells are performed in an Emcore MOCVD D-125 rotating disk reactor with a short jar configuration shown in Figure 5.1. The configuration of Emcore's D-125 GaN system is ideal for growth of the high aluminum content layers critical for producing quality UV LEDs and HEMTs. Exceptional run-to-run repeatability is achieved for GaN/AlGaN layers through the use of a vertical chamber design that eliminates particle accumulation, a loadlock system that fully isolates the reactor from oxygen and water vapor, and a method for easy removal of platters for cleaning external to the growth area. In addition, all processes developed on the small-scale D-125 tool can later be seamlessly scaled up to mass production. An in-situ reflectometry monitoring system is installed to control the growth rate in real-time.

Trimethylgallium (TMGa) $\{(CH_3)_3Ga\}$, Triethylgallium (TEGa) $\{(C_2H_5)_3Ga\}$, Trimethylindium (TMIn) $\{(CH_3)_3In\}$and Trimethylaluminium (TMAl) $\{(CH_3)_3Al\}$are the common precursors to introduce metal into the MOCVD reactor. A carrier gas, usually H_2 and sometimes N_2, is used to transfer the precursors into the reactor as they have a high

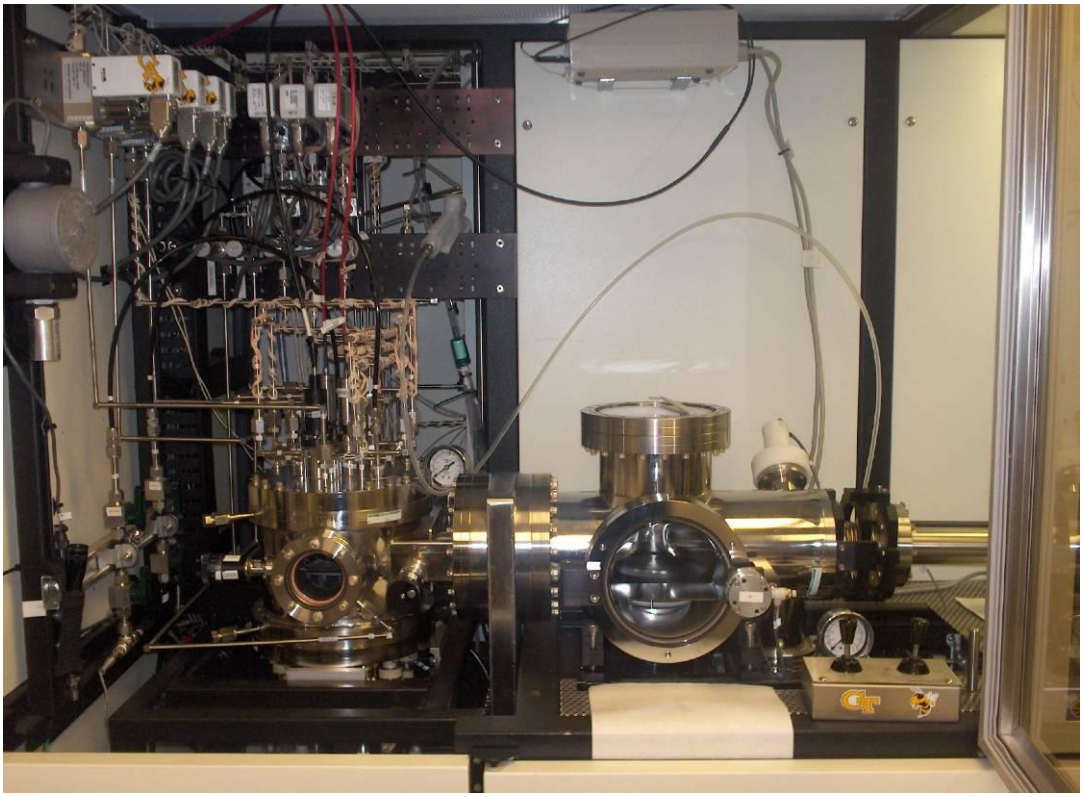

(a)

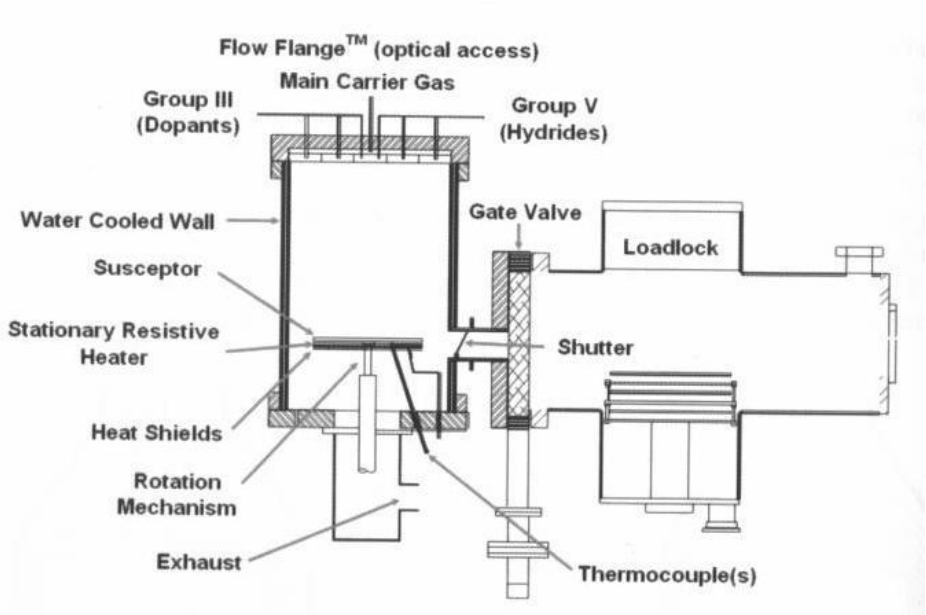

(b)

Figure 5.1: (a) Photograph, and (b) schematic of the Emcore MOCVD growth reactor.

vapor pressure at room temperature. Ammonia (NH_3) is used as the nitrogen source. Bis cyclopentadienyl magnesium (Cp_2Mg) {$(C_5H_5)_2Mg$}, is used to carry Mg, which is a p-type dopant, while silane {SiH_4}, is used to carry Si, which is the n-type dopant.

The precursor gases are introduced, mixed and catalyzed in the reactor chamber. Appropriate reactor temperature and pressure drives the pyrolysis of the precursor gases to yield the final III-V compound. A typical pyrolysis reaction of GaN is described in Equation 5.1.

$$(CH_3)_3Ga + NH_3 \rightarrow GaN + 3CH_4 \quad \text{--- (5.1)}$$

(TMGa) (Ammonia) (Methane)

Practical epitaxial MOCVD growth process commonly applied for GaN and other III-V semiconductors depends on factors such as thermodynamics, mass transport and kinetics of the reaction. Thermodynamics is the main force that drives this pyrolysis, where the precursors become unstable at high temperatures and react. Thermodynamics sets the maximum limit for growth rate, and the achieved growth rate depends on mass transport, which affects the thickness uniformity of the deposited film. Moreover, while thermodynamics governs the behavior of the system at equilibrium, kinetics controls the tendency of the system to move towards the equilibrium state under a given growth condition. Practical process conditions in MOCVD growth are under excess, uninterrupted, and non-stoichiometric group V species, nitrogen in our case, which improves the pyrolysis efficiency by compensating for the much greater volatility of the group V atoms in the desired epitaxy.

5.1.2 Epitaxy of GaN templates

As GaN substrates are not typically available, a GaN or AlN template is formed on foreign substrates before carrying forward the desired growth. A c-plane sapphire is the substrate of choice for III-nitride optoelectronic devices due to its superior thermal stability, mechanical and optical qualities.

A two-step process is used to grow GaN templates where a low-temperature buffer absorbs the defects arising due to lattice mismatch at the substrate, which is followed by a high-temperature growth to yield a superior crystalline quality layer. A typical two-step growth process is illustrated in Figure 5.2, which shows the chronological temperature profile of the epitaxy and the corresponding epitaxial surface quality as measured by in-situ reflectometry.

(1) First, a prebaking takes place, where the substrate is heated at 1100 °C for 3 – 4 minutes in hydrogen ambient to improve the surface quality followed by a nitridation by introducing ammonia into the reactor. (2) Then a low temperature buffer GaN of thickness around 20 – 40 nm is grown at 550 °C. (3) The buffer layer is then recrystallized by ramping the temperature to 1030 °C in ammonia ambient to decrease the defects arising due to lattice mismatch with the substrate. (4) A rough GaN is grown at a temperature lower than the main GaN growth temperature by 20 °C. (5) The main GaN layer is grown at 1050 °C and a growth rate of approximately 2 μm/hr to yield a high quality surface as indicated by the strong oscillations in the reflectometry reading. Such a template typically demonstrates a low dislocation density, in the 10^{7} – 10^{10} cm^{-2} range [24]-[27], limiting the n-type background concentration, which arises due to nitrogen vacancies, in the order of 10^{16} cm^{-3}.

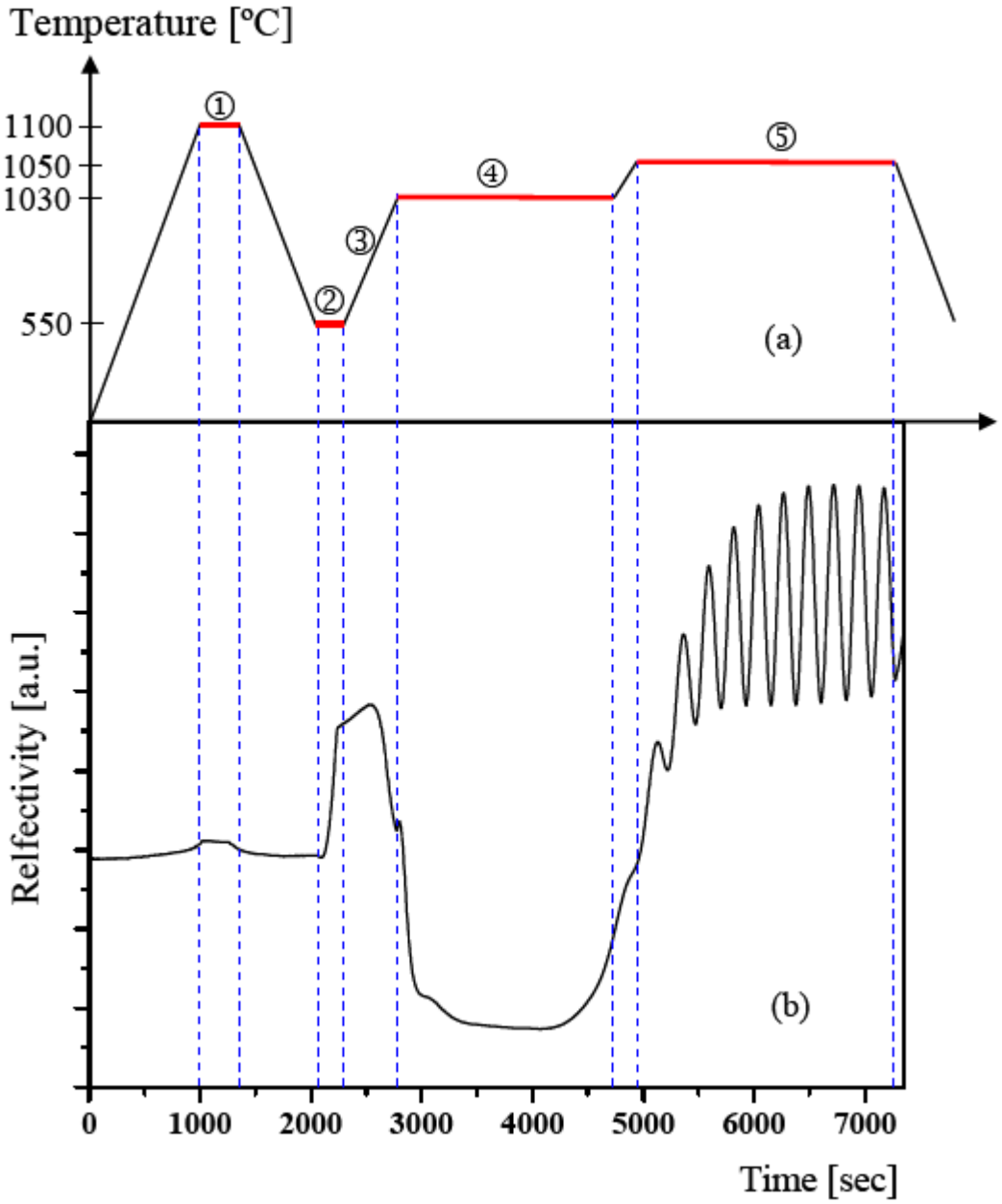

Figure 5.2: (a) Chronological temperature profile, and (b) in-situ reflectometry data for a typical two-step GaN template growth.

5.2 EPITAXY OF INGAN FOR SOLAR CELLS

5.2.1 Preliminary growth of InGaN

A systematic study of InGaN epitaxy by MOCVD is conducted for indium compositions ranging from 0 to 35%. The primary variables used to control the InGaN epitaxy are the precursor gas flow rates, which changes the III-V ratio and growth rate; temperature, which primarily governs the indium composition in the InGaN; and final epitaxial layer thickness. All the test InGaN layers are grown on a 2 μm thick GaN template. XRD data of the InGaN epilayers are represented on the same scale in Figure 5.3 for comparison. The XRD data indicates the composition and quality of constituent materials in the epitaxy.

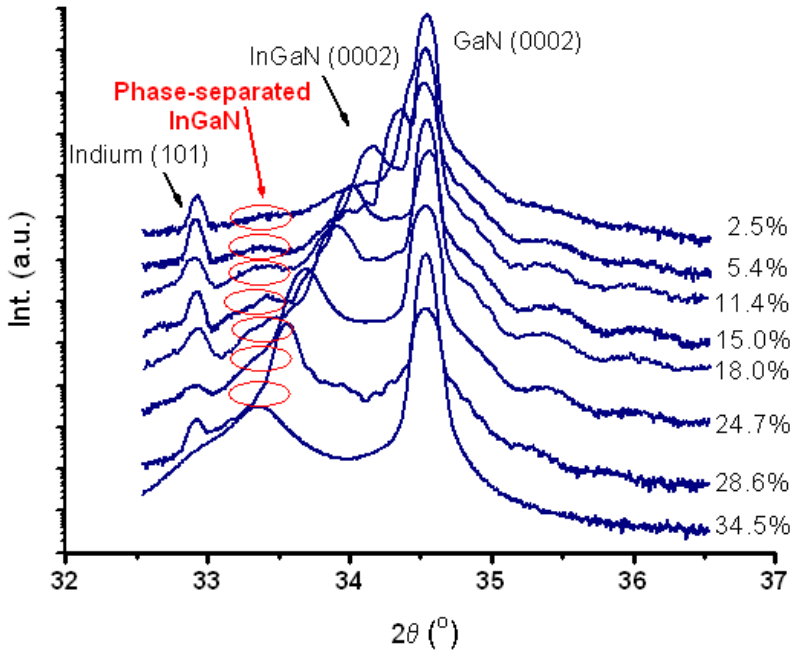

Figure 5.3: Summary of X-ray diffraction data for InGaN grown by MOCVD with indium composition ranging from 0 to 35%.

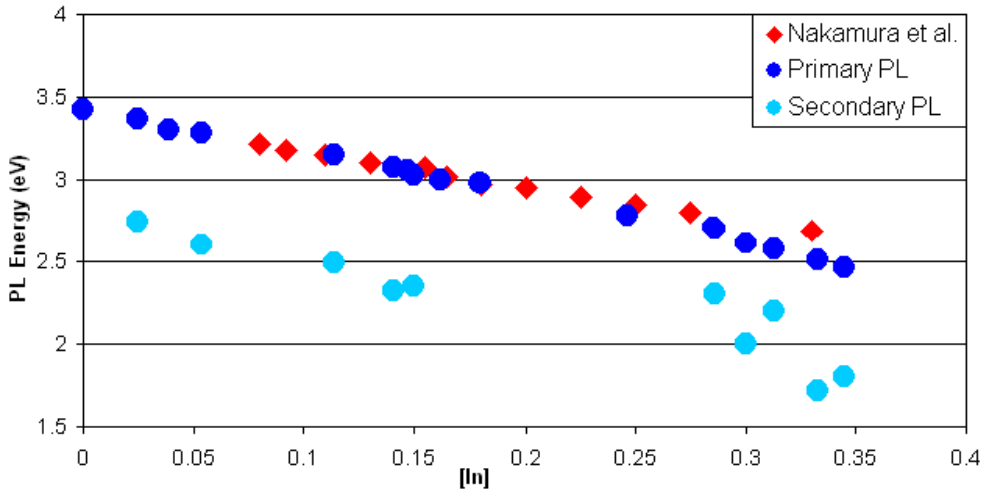

Figure 5.4: Photoluminescence vs. indium composition for InGaN grown by MOCVD.

A distinct GaN (0002) peak corresponding to the template is observed at $\theta = 17.28^{\circ}$, while the InGaN (0002) peaks indicate the respective indium compositions. Secondary InGaN peaks are also visible, which indicate the presence of a phase separated material. Additional indium (101) peaks are observed indicating a small amount of segregated indium droplets [112].

The material is further characterized for optical consistency and phase separation by PL. Figure 5.4 summarizes the optical band gaps, derived from PL peaks, for various indium compositions in InGaN, derived from XRD data. The primary PL peaks indicating the optical band gaps match closely to previously measured band gaps by Nakamura *et al* [113]. However, a few samples show secondary PL peaks indicating the presence of a phase-separated InGaN. The presence of phase separated InGaN is more evident at higher indium compositions as PL intensity for the secondary phase emission increases for these indium compositions.

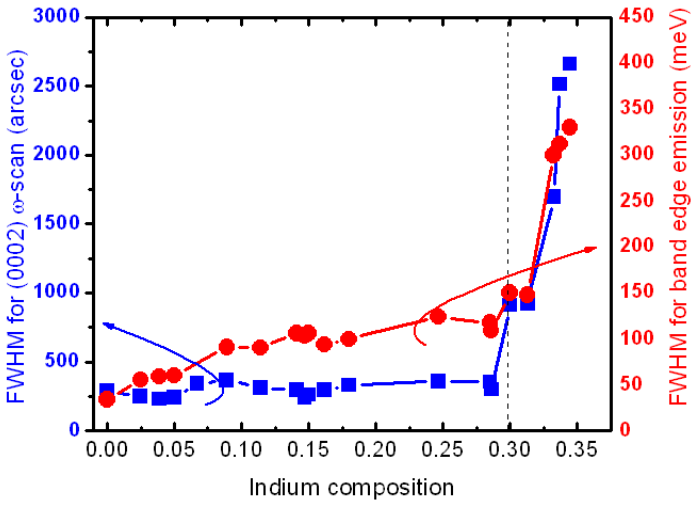

Figure 5.5: Summary of FWHM for (0002) ω-scan and PL for InGaN grown by MOCVD as a function of indium composition.

Figure 5.5 presents the comprehensive summary of the crystalline and optical quality of the grown InGaN. Here, the FWHM (Full Width Half Maximum) of both, XRD and PL, are presented as a function of indium composition. It is clearly seen that the quality of the material drastically deteriorates for indium compositions greater than 30%. Thus, InGaN solar cells with indium compositions up to 30% can be targeted with this state of material quality. However, it becomes imperative to study and suppress phase separation, which can potentially have detrimental effects of the solar cell performance.

5.2.2 Suppression of phase separation in InGaN

The TEGa flow rate is an important parameter in MOCVD that primarily governs the growth rate of GaN epitaxy. InGaN layers with variable TEGa flow rates are grown to study its influence on phase separation in InGaN. As illustrated in Figure 5.6, the composition of InGaN changes with varying TEGa flow rates. At high TEGa flow rates,

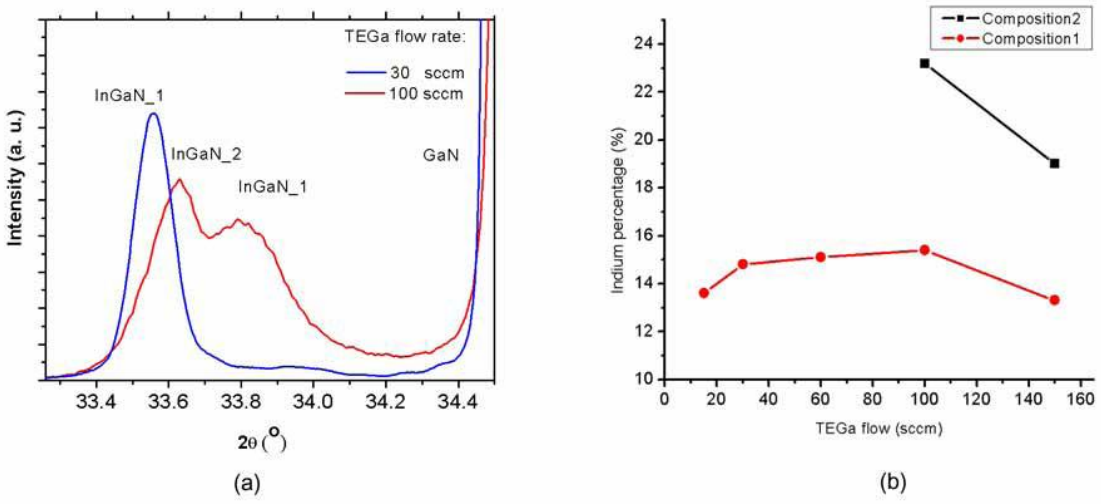

Figure 5.6: (a) XRD scans and (b) indium compositions for InGaN grown at variable TEGa flow rates.

the indium composition decreases and also a secondary phase-separated domain is generated. While the composition of the primary indium phase only changes slightly, the strain state in the material varies to a much greater extent due to the additional gallium species, giving rise to the secondary InGaN phase. This phenomenon is visible at a macroscopic level and clearly evident in XRD scans.

At a growth temperature of 720 °C and TEGa flow rate of 30 sccm, high crystalline quality InGaN layers with indium composition of 7% are repeatedly obtained. However, secondary PL emissions are generally observed from the phase-separated InGaN. This secondary peak progressively disappears as the TMIn flow rate increases from 30 sccm to 200 sccm, while emission from primary InGaN matrix stays constant at 3.1 eV as shown in Figure 5.7. Moreover, the secondary emission undergoes a red-shift as it disappears.

InGaN is also grown at the same growth conditions but with varying thickness to study the effect of epitaxial thickness on phase separation. As seen in Figure 5.8, PL

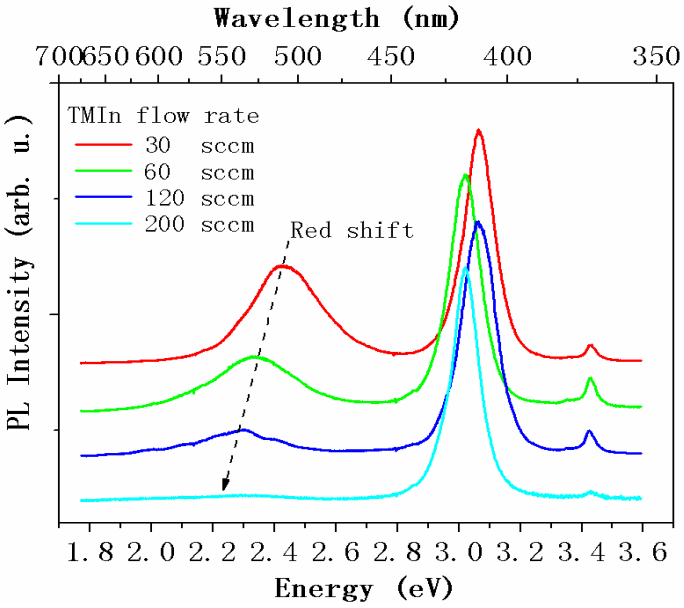

Figure 5.7: PL of $In_{0.07}Ga_{0.93}N$ grown at variable TMIn flow rates.

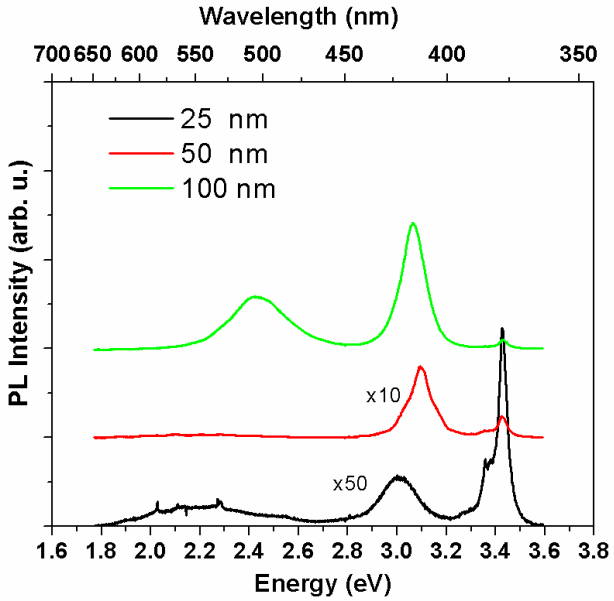

Figure 5.8: PL obtained for InGaN with variable thickness

emission from secondary InGaN phases are more prominent at higher thicknesses. Here, phase separation is caused due to strain relaxation at higher epitaxial thicknesses. Moreover, the material stays in the growth ambient for a longer time for higher thicknesses, where it has both, sufficient time as well as energy, to relax and form two phases. Thus, it is important to control the thickness of the epitaxial InGaN to indirectly control phase separation.

5.2.3 Absorption coefficient of InGaN

It is important to reconfirm the high absorption coefficient values of InGaN especially due to the insufficiency and discrepancy in reported literature [90]-[92], as well as predict values for InGaN with specific indium compositions, before designing a solar cell. Approximately 100 nm thick InGaN layers of variable indium compositions are grown on GaN templates by MOCVD for spectrometry measurements. Thin InGaN layers are used for absorption measurements as they incompletely absorb light, and hence, the fraction of light absorbed can be correlated to epitaxial thickness to accurately determine the absorption coefficients.

The main experimental setup for absorption measurement is based on the setup used to measure Quantum Efficiency (QE), with the QE sample replaced by a second photodiode that mounted beneath the test InGaN sample. The position of this transmission diode is adjusted for maximum signal over the full range of wavelengths and care is taken that for a baseline measurement, with no InGaN sample in place, the voltage measured on the reflectance diode is zero. With a sample in place, the two diodes are each adjusted so that light striking them is focused on the active area. Most of the data is taken at an incidence

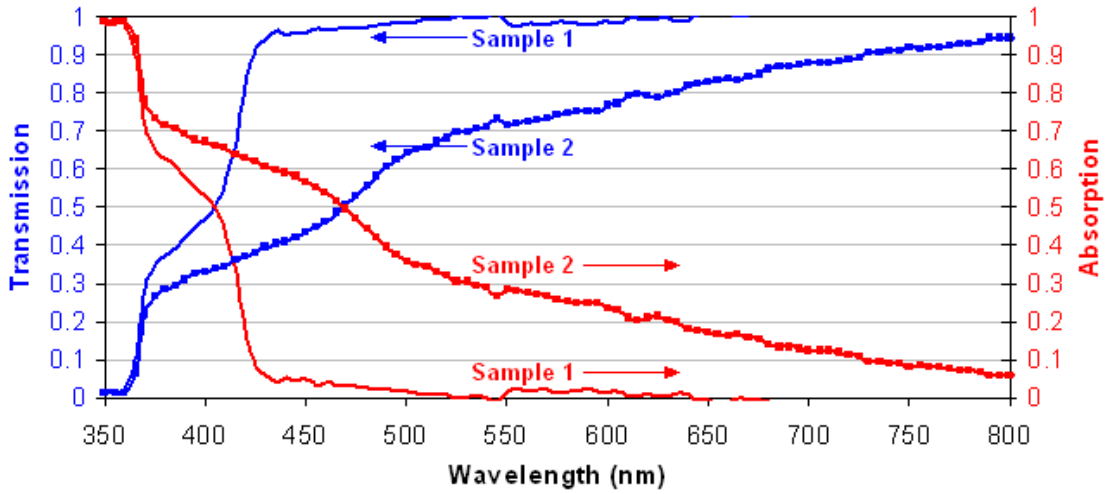

Figure 5.9: Measured transmission and absorption data for InGaN of band gap 2.95 eV (Sample 1) and 2.45 eV (Sample 2).

angle of 18 ± 2 degrees. This setup is only able to measure the specular reflection and transmission, and requires correction for diffusion caused by the unpolished side of the sapphire substrate, on which InGaN is epitaxially deposited. Some samples are also measured using a Perkin-Elmer Lambda-9 UV-visible-IR spectrophotometer, which uses an integrating sphere to account for diffused light.

The measured transmission – absorption curves for two InGaN samples of band gaps 2.95 eV (Sample 1) and 2.45 eV (Sample 2) are shown in Figure 5.9. The transmission data is corrected for both, scattering of diffused light as well as reflection. Shoulders are seen in the curves between 365 nm and wavelength equivalent to the band gap of the InGaN sample (420 nm for Sample 1 and 510 nm for Sample 2) due to incomplete absorption by the InGaN.

The absorption coefficients for InGaN can be extracted from transmission measurements using the following equation:

$$I_t(\lambda) = I_o(\lambda) \cdot e^{-\alpha(\lambda) \cdot x} \qquad \text{--- (5.2)}$$

where, $I_t(\lambda)$ = intensity of transmitted light as a function of wavelength λ,

$I_o(\lambda)$= intensity of incident light as a function of wavelength λ,

x = thickness of sample (cm), and

α (λ)= absorption coefficient as a function of wavelength λ (cm^{-1}).

The extracted absorption coefficient as a function of incident photon energy for the two samples is given in Figure 5.10. Sub-band gap absorption is observed for lower band gap samples (e.g. Sample 2) due to presence of lower band gap phases or defects in the material.

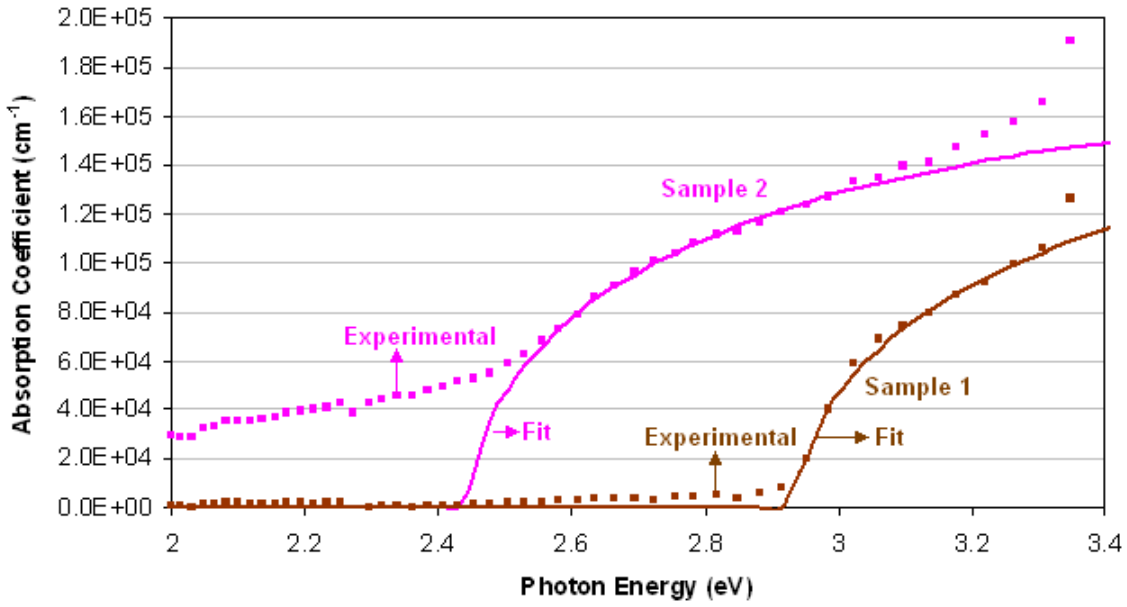

Figure 5.10: Measured absorption coefficient and theoretical fit for InGaN samples of band gap 2.95 eV (Sample 1) and 2.45 eV (Sample 2).

Table 5.1: Fitting parameters used for absorption coefficient of InGaN samples of band gap 2.95 eV (Sample 1) and 2.45 eV (Sample 2).

Parameter	**Sample 1**	**Sample 2**
α_o ($eV^{1/2}/cm$)	5.7×10^5	5.2×10^5
EG (eV)	2.95	2.45

A theoretical curve for absorption coefficient is fitted to the experimental data using Equation 5.3:

$$\alpha(E) = \alpha_o \cdot \frac{(E - EG)^{1/2}}{E} \qquad \text{--- (5.3)}$$

where, $\alpha(E)$ = absorption coefficient as a function of photon energy E,

α_o = fitting parameter ($eV^{1/2}/cm$), and

EG = band gap of semiconductor.

The fitting parameters used for the two samples are given in Table 5.1. These experiments confirm the high absorption coefficients in the InGaN, which are an order higher than other III-V semiconductors like GaAs [114][115]. The absorption coefficients of InGaN are in the order of 10^5 cm^{-1}. Materials with such high absorption coefficients absorb about 63% of light within the first 100 nm and 99% of light within the first 500 nm of its thickness.

5.3 FABRICATION OF INGAN SOLAR CELLS

5.3.1 Mg-activation in InGaN

Prior to device processing, the p-type III-nitride requires activation of the Mg dopant. While various anneal conditions are reported in the literature [116][117], the standard procedure used in the lab to activate p-GaN consists of a 4 minute anneal at 800 °C in a N_2 ambient in a Rapid Thermal Annealer (RTA). However, as InGaN is typically grown at lower temperatures (depending on the intended indium composition), such high temperature anneals are avoided to for possible complications like lattice rearrangement. Hence, the anneal temperature is kept at least 100 °C less than the growth temperature. However, the anneal time has to be increased at lower temperatures due to the high energy requirement for InGaN activation. Three optimized anneal conditions for InGaN are presented in Table 5.2. Acceptor concentrations up to 10^{19} cm^{-3} are achieved for indium compositions up to 15%.

5.3.2 Metal contact schemes

The three types of contacting schemes designed for the InGaN solar cells are shown

Table 5.2: Optimized anneal conditions for InGaN.

	Temperature	**Time**	**N_2 flow rate**
1	800 °C	4 minutes	2 Liters/minute
2	700 °C	20 minutes	2 Liters/minute
3	625 °C	30 minutes	2 Liters/minute

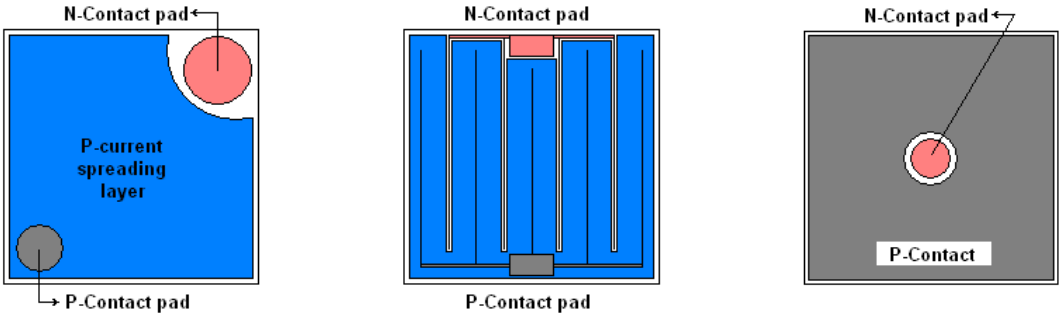

(a) (b) (c)

Figure 5.11: Contacting schemes used for InGaN solar cells that involve (a) top current spreading layer, (b) interdigitated grid contacts, and (c) solid opaque contacts.

in Figure 5.11. The first scheme (Figure 5.11(a)) is similar to that used for III-nitride LED's. It consists of a current spreading layer that covers the entire top surface of the device. This layer, which is typically a thin metal or a Transparent Conducting Oxide (TCO), is used to assist the current spreading in the more resistive p-GaN and lower the Ohmic resistance of the device. However, this layer does tend to absorb light, which directly decreases the short-circuit current, and hence, efficiency, of the solar cell.

Contacts for solar cells epitaxially grown on a sapphire substrate cannot be formed from the substrate side due to the insulating nature of sapphire. Therefore, and interdigitated contact scheme (Figure 5.11(b)), more popular in solar cells [118], is used to reduce the absorption loss. Such contacts require optimization of grid spacing as it is intended for light to enter the solar cell from the contact-metal side and not the sapphire side. Increasing grid spacing tends to minimize the fraction of light reflected by the grids and hence, maximize the light absorbed in the solar cell. However, increasing the grid spacing also contributes to the series resistance of the solar cell and reduces its efficiency.

The calculated optimal grid spacing for InGaN solar cells result into shading of about 50% of the top surface of the device, and hence is impractical. This is due to this high resistivity of the p-GaN top layer. Hence, the grid spacings for the actual InGaN solar cells are varied from 50 μm to 200 μm.

The third contacting scheme (Figure 5.11(c)) employs opaque p- and n-contacts the cover the entire surface of the solar cell to reduce the series resistance of the solar cell. Such contacts are applicable for flip-chip devices that are illuminated from the substrate side.

5.3.3 Device processing

A typical device processing sequence for an InGaN p-i-n solar cell is shown in Figure 5.12. A standard acetone – methanol – water rinse followed by N_2 blow-drying is used to clean the wafer before and between processing to rid the sample of any grease, dust or organic impurities.

First, a mesa pattern is deposited on the epitaxial p-i-n structure using photolithography to define the area of the solar cell. The thickness requirement of the photoresist is governed by the intended etch depth of InGaN. Usually a thick photoresist layer is deposited as the etch rate of the photoresist is approximately the same as that of InGaN. The photoresist is also cured at 120 °C for 30 minutes to harden it. Then the wafer is etched using chlorine plasma in an Inductively Coupled Plasma (ICP) tool to expose the n-layer (Figure 5.12(b)). ICP is preferred over Reaction Ion Etching (RIE) as it provides a better etch anisotropy; a higher degree of anisotropy is required to maintain vertical mesa walls to avoid short circuiting and increase resolution during fabrication. At the end of the etch, the sample is soaked in acetone for at least six hours and then the excess photoresist is stripped in an ultrasonic bath followed by the standard clean.

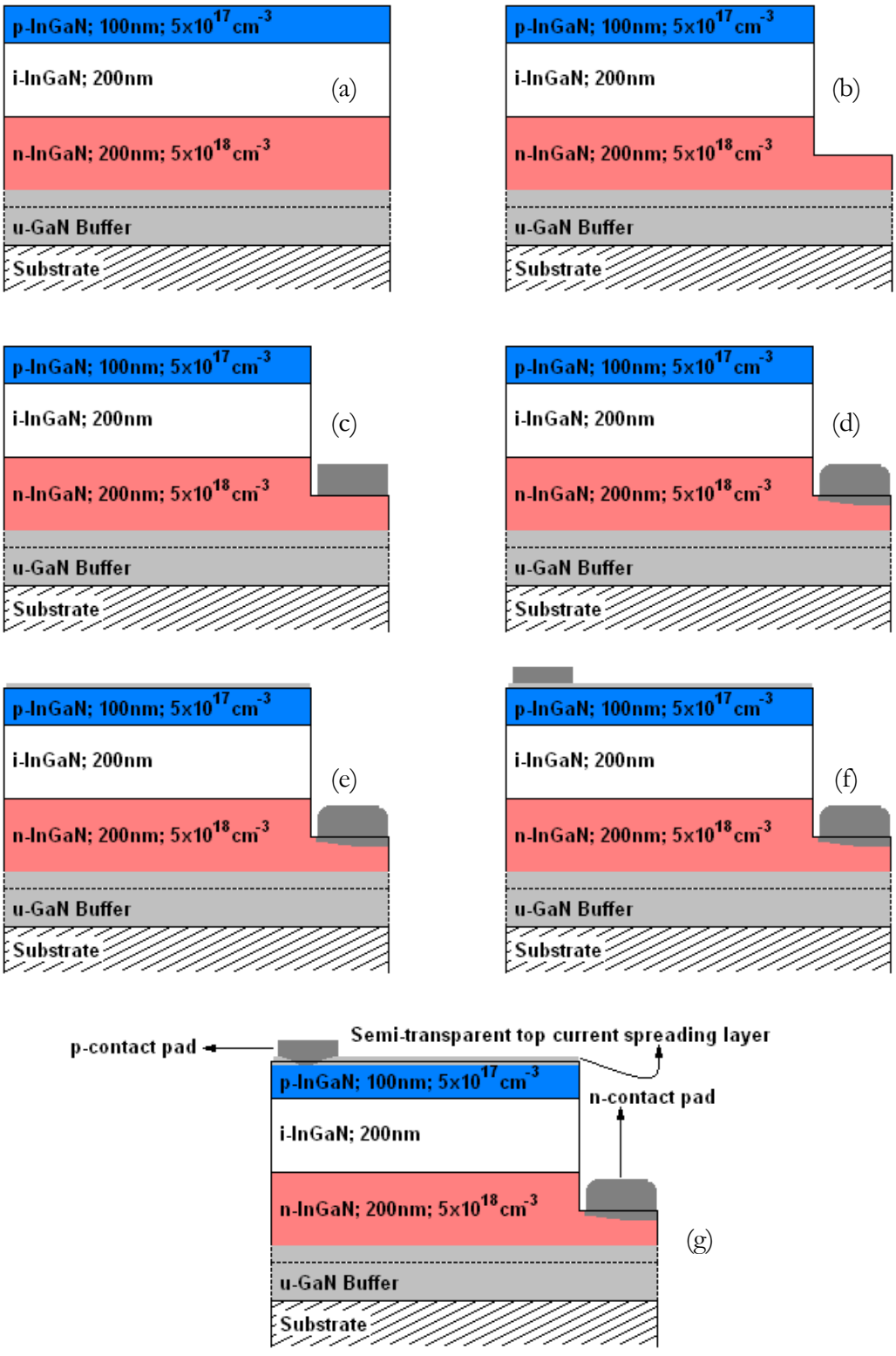

Figure 5.12: Typical fabrication process sequence for an (a) InGaN p-i-n solar cell involving (b) mesa etch, 9c) n-contact deposition, (d) n-contact anneal, (e) current spreading layer deposition, (f) p-contact deposition, and (g) p-contact anneal.

A second pattern is deposited via photolithography to contact the n-type layer. However, just before metallization, the wafer is treated in a 1:6 Buffered Oxide Etch (BOE):H_2O solution for 30 seconds at room temperature to strip off any oxides developed at the semiconductor surface after the epitaxial growth or ICP etch. Such chemical treatments have shown to yield superior quality Ohmic contacts [119][120]. An electron-beam metal deposition of 10 nm Ti – 30 nm Al – 10 nm Ti – 50 nm Au is carried out to contact the n-type layer (Figure 5.12 (c)). After metal liftoff, the contacts are annealed in a RTA for 1 minute at 575 °C in a N_2 ambient (Figure 5.12(d)) to improve the contact properties.

After the second photolithography step and a BOE treatment, a thin semi-transparent current spreading Ni-Au layer is deposited on p-GaN in the electron-beam evaporator (Figure 5.12(e)). Indium Tin Oxide (ITO) is also employed as the current spreading layer depending upon the design criteria of the solar cell; such designs will be discussed in the later chapters of the work.

After the third photolithography step to pattern windows for the p-contact, a 50 nm Ni – 50 nm Au deposition is carried out in the e-beam evaporator (Figure 5.12(f)). After liftoff, the sample is annealed in an O_2 ambient at 525 °C for minute. This is the optimized condition to oxidize Ni and yield a p-contact with Ohmic characteristics (Figure 5.12(g)).

Figure 5.13(a) shows the picture of a completely fabricated 2" InGaN solar cell wafer. Here, the device sizes of 1 mm x 1mm, 3 mm x 3 mm and 5 mm x 5mm are clearly visible. The details of the interdigitated contact can be seen in Figure 5.13(b). A detailed process flow for a typical p-i-n InGaN solar cell fabrication is provided in Appendix B. Slight variations are made in the fabrication procedure in terms of metallization schemes and order, which are discussed in the later chapters of the work.

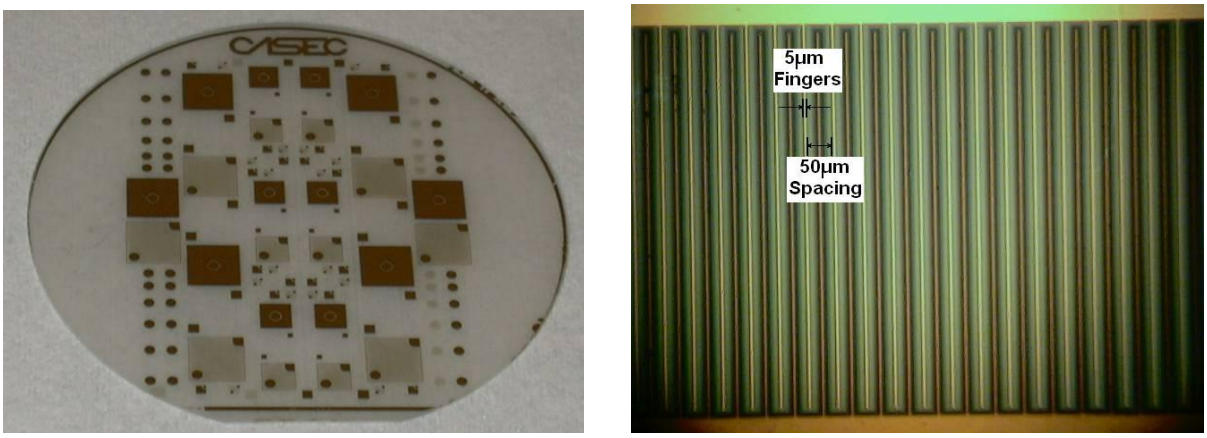

(a) (b)

Figure 5.13: (a) Macroscopic view of fabricated 2" InGaN solar cell wafer, and (b) microscopic view of grid contacts in a device with interdigitated grids.

5.4 SUMMARY

Individual tasks such as controlling InGaN crystallinity and phase separation, confirming high absorption coefficients, optimizing Mg-incorporation and activation conditions to obtain p-type InGaN, and streamlining the device contact and fabrication schemes are performed. InGaN calibration samples with indium compositions ranging from 0 to 35% are grown by MOCVD; while increasing the epitaxial growth rate and controlling the thickness of the epitaxy are identified as the direct and indirect methods, respectively, to control phase separation in the material. Moreover, high absorption coefficients of InGaN reduce the epitaxial thickness requirements for InGaN solar cells. Finally, an optimized fabrication scheme with variable contact configurations is developed to fabricate InGaN solar cells. The fabricated solar cells, with individually optimized components, are then tested; the next step of the development process is to comprehensively optimize the solar cell as a whole.

6. InGaN SOLAR CELL RESULTS

The latter stages of InGaN solar cell development involve simultaneous optimization of design as well as experimental, i.e. growth and fabrication, this comprehensive process is further simplified into two phases. The preliminary development phase is based on optimization of the InGaN material using a standard solar cell design. Here, the band gap of the InGaN is progressively lowered in the i-region of a p-i-n solar cell, while p- and n-junctions are limited to GaN. Fabrication techniques are also optimized during this process to primarily yield low resistance and high light transmissivity contacts. Once, the suitability of InGaN with a specific band gap for photovoltaic purpose is established, the development process moves into its second phase – design optimization. In this phase, the optimized InGaN is incorporated into advance solar cell designs and tested. These solar cell designs are iteratively optimized with material quality to extract maximum efficiency. Six generations of InGaN solar cells are developed in this manner yielding high open-circuit voltages and quantum efficiencies as discussed here.

6.1 PRELIMINARY INGAN SOLAR CELL RESULTS

6.1.1 Suitability of InGaN for photovoltaics

Preliminary solar cells are fabricated to test the suitability of the InGaN as a photovoltaic material. InGaN of band gaps 3 eV ([In] = 0.07) and 2 eV ([In] = 0.4) are

targeted as the test material. InGaN is incorporated into the i-region of the p-i-n solar cell as described in Section 3.3 - Preliminary InGaN solar cell design. Additionally, quantum-well solar cell structures incorporating $In_{0.4}Ga_{0.6}N$ as the quantum-well layers in p-i-n GaN solar cells are also fabricated. In addition to sub-band gap absorption, such structures ensure a high epitaxial quality of pseudomorphic thin $In_{0.4}Ga_{0.6}N$, which can possibly degrade at bulk thicknesses. Five $In_{0.4}Ga_{0.6}N$ quantum-wells of 1 nm thickness are separated by 13.8 nm wide GaN barriers as shown in the band diagram in Figure 6.1.

The devices are fabricated into mesa structures of size 320 μm x 320 μm as shown in Figure 6.2. 10 nm Ti – 30 nm Al – 10 nm Ti – 50 nm Au is used as the n-contact, while an oxidized 5 nm Ni- 5 nm Au top current spreading layer followed by a 50 nm Ni – 50 nm Au deposition is used to form the p-contact to the solar cell.

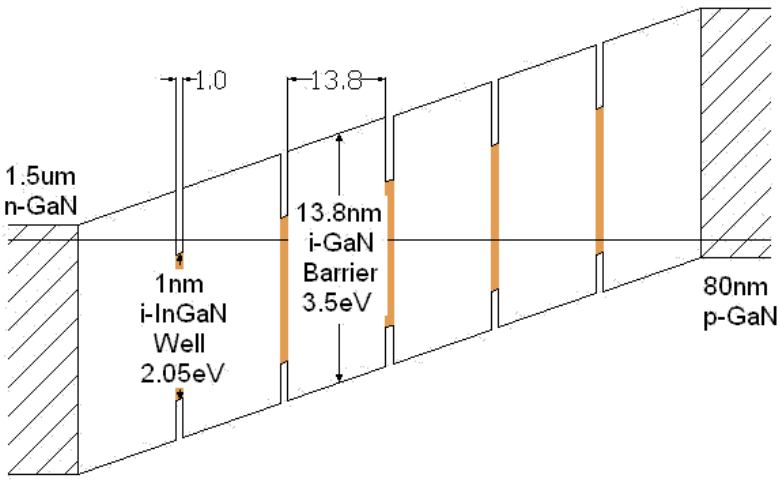

Figure 6.1: Band diagram of p-i-n GaN solar cell with In0.4Ga0.6N quantum wells.

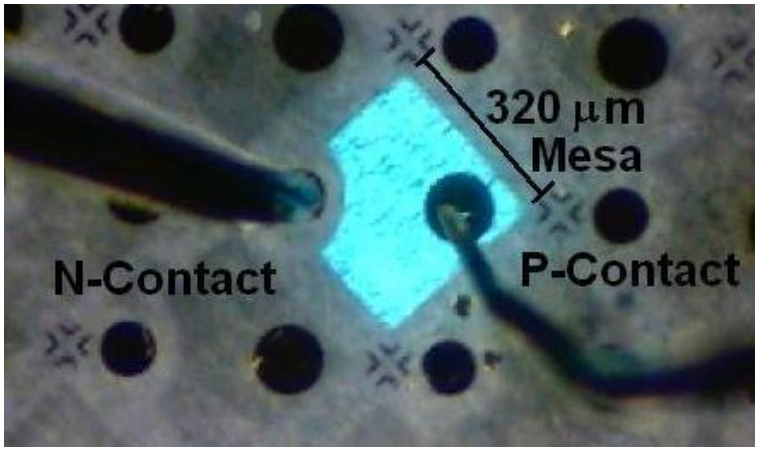

Figure 6.2: Fabricated preliminary InGaN solar cell.

The crystalline quality of the solar cells is compared using the XRD and PL data summarized in Figure 6.3. The XRD data of the $In_{0.07}Ga_{0.93}N$ solar cell (Figure 6.3(a)) indicates a broad range of indium composition ranging from 3% to 16% with maximum intensity at 7%. The strong peak at $\theta = 17.28^{\circ}$ indicates a good crystalline quality of GaN. The PL data for this device (Figure 6.3(b)) indicates two InGaN peaks – a broad peak centered at 510 nm, which corresponds to an indium composition of 27%, and a stronger narrow peak centered at 500 nm, which corresponds to an indium composition of 28%. These peaks marginally vary spatially over the epitaxial wafer. A GaN emission peak at 365 nm is also observed for the sample. However, no PL is observed at 400 nm wavelength, which corresponds to the targeted indium composition of 7%. The discrepancy in XRD and PL data indicates a low band gap recombination channel and hence, the presence of phase separation in the material.

The poor crystalline quality of InGaN in the bulk $In_{0.4}Ga_{0.6}N$ solar cell is evident from the weak XRD peak shown in Figure 6.3(c). However, the indium composition of the

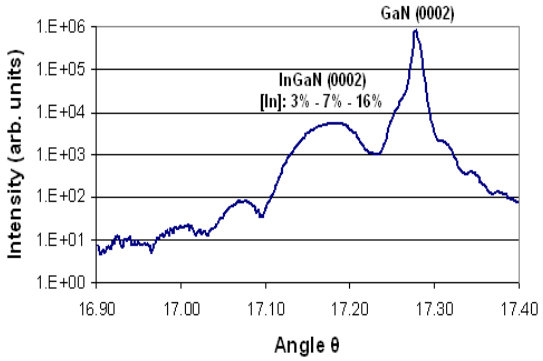

(a) $In_{0.07}Ga_{0.93}N$ p-i-n XRD

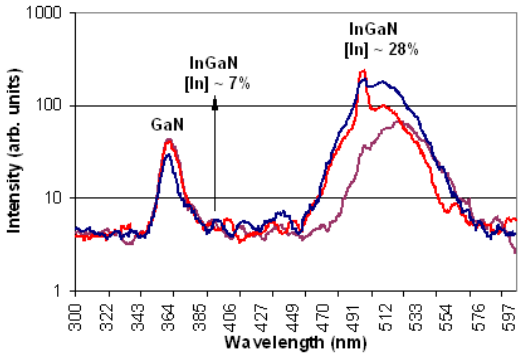

(b) $In_{0.07}Ga_{0.93}N$ p-i-n RT-PL

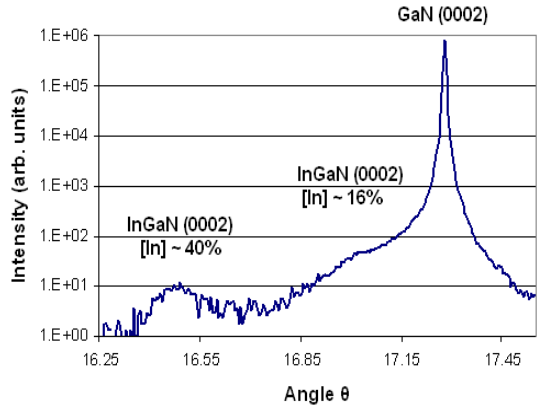

(c) $In_{0.4}Ga_{0.6}N$ p-i-n XRD

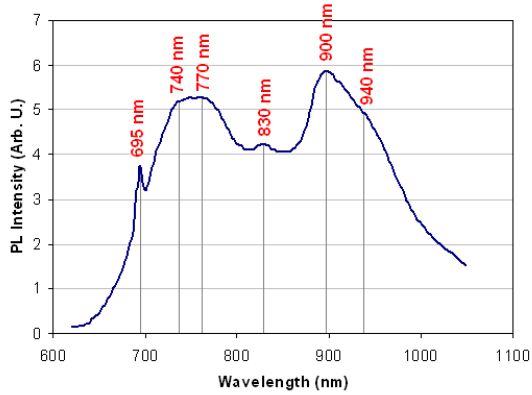

(d) $In_{0.4}Ga_{0.6}N$ p-i-n LT-PL

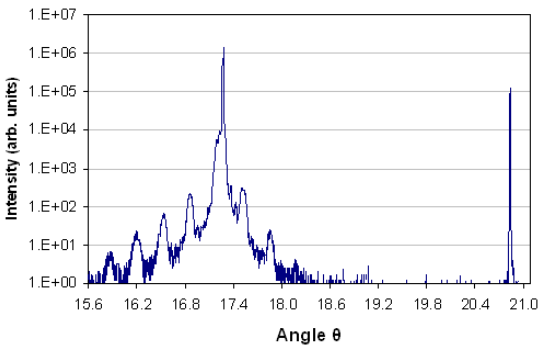

(e) $In_{0.4}Ga_{0.6}N$ QW XRD

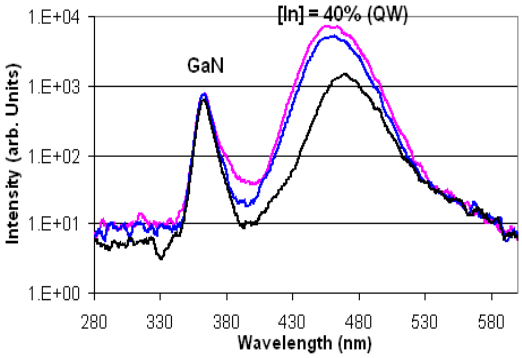

(f) $In_{0.4}Ga_{0.6}N$ QW RT-PL

Figure 6.3: (a) XRD and (b) PL of In0.07Ga0.93N p-i-n solar cell, (c) XRD and (d) PL of In0.4Ga0.6N p-i-n solar cell, and (e) XRD and (f) PL of In0.4Ga0.6N quantum-well solar cell.

material is confirmed at 40%. As no PL from InGaN is observed at room temperature for this sample, a low temperature (77 K) PL at longer wavelengths is performed to investigate this material (Figure 6.3(d)). Multiple recombination peaks at low wavelengths indicate a heavily defected bulk $In_{0.4}Ga_{0.6}N$.

The quantum-well structures are clearly visible in the XRD seen in Figure 6.3(e). The GaN peak is seen at θ=17.28°, while subsequent peaks correspond to the InGaN quantum-well material with 40% indium composition and its lower order harmonics. The thickness of the quantum-wells and barriers were confirmed at 1nm and 13.8nm respectively through further curve-fitting. Moreover, the distinct, close-to-ideal, peaks verify the growth of a good quality crystalline heterostructure. PL data indicates a strong InGaN peak at 460 nm (Figure 6.3(f)), which matches the theoretical value of a quantum-well emission of similar band gap and dimensions.

The fabricated test devices are tested for Current-Voltage (I-V) characteristics in three conditions: (1) in dark, (2) under white light, and (c) under UV illumination. Figure 6.4

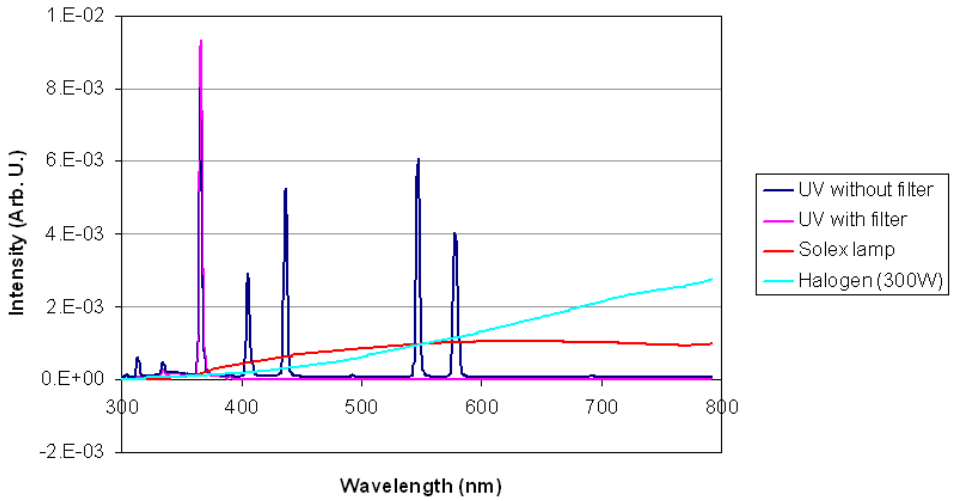

Figure 6.4: UV lamp source illumination compared to common light sources.

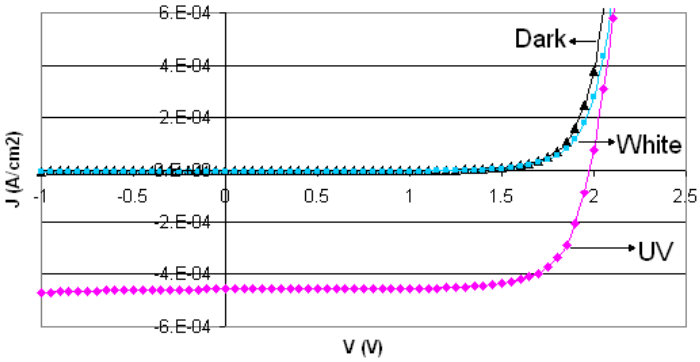

(a) $In_{0.07}Ga_{0.93}N$ p-i-n solar cell.

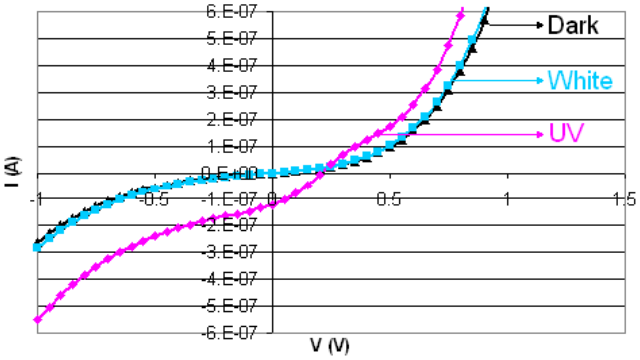

(b) $In_{0.4}Ga_{0.6}N$ p-i-n solar cell.

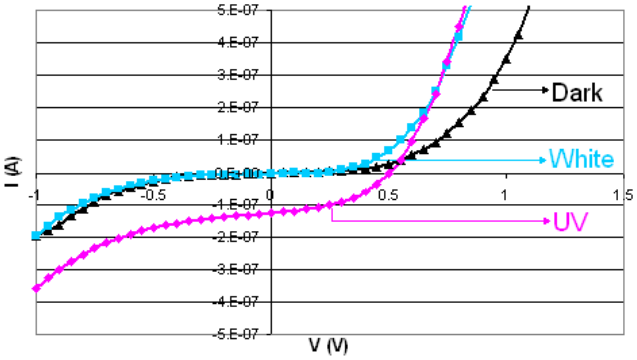

(c) $In_{0.4}Ga_{0.6}N$ QW solar cell.

Figure 6.5: I-V characteristics comparison of (a) In0.07Ga0.93N p-i-n solar cell, (b) In0.4Ga0.6N p-i-n solar cell, and (c) In0.4Ga0.6N quantum-well solar cell.

gives the spectrum of the UV illumination and compares it with the spectrum of other common illuminations used for solar cell testing. The spike in intensity at 365 nm indicates that this light has energy high enough to be absorbed by GaN and InGaN, and cause a photoresponse in the constituent solar cell.

The I-V characteristics of the test solar cells are summarized in Figure 6.5. The $In_{0.07}Ga_{0.93}N$ p-i-n solar cell does not respond to white light due to its high band gap, but it provides a V_{OC} of 2 V and FF of 75% under UV illumination. While the V_{OC}'s for solar cells are typically 0.4 eV less than the band gap potential of the material, the measured voltages for InGaN solar cells at 2 V are less than the expected values for a 3 eV material. However, the V_{OC}'s are in accordance with the recombination channel observed during PL measurements at 500 nm, which corresponds to a band gap of 2.5 eV. Moreover, a bright luminescence at 500 nm is also observed when the solar cell is forward biased (Figure 6.6) confirming the dominating behavior of this recombination channel.

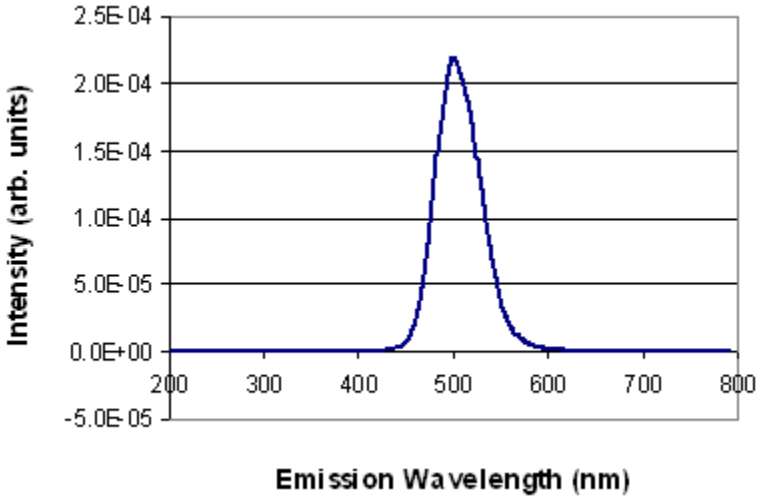

Figure 6.6: Photoemission spectrum from a biased In0.07Ga0.93N p-i-n solar cell.

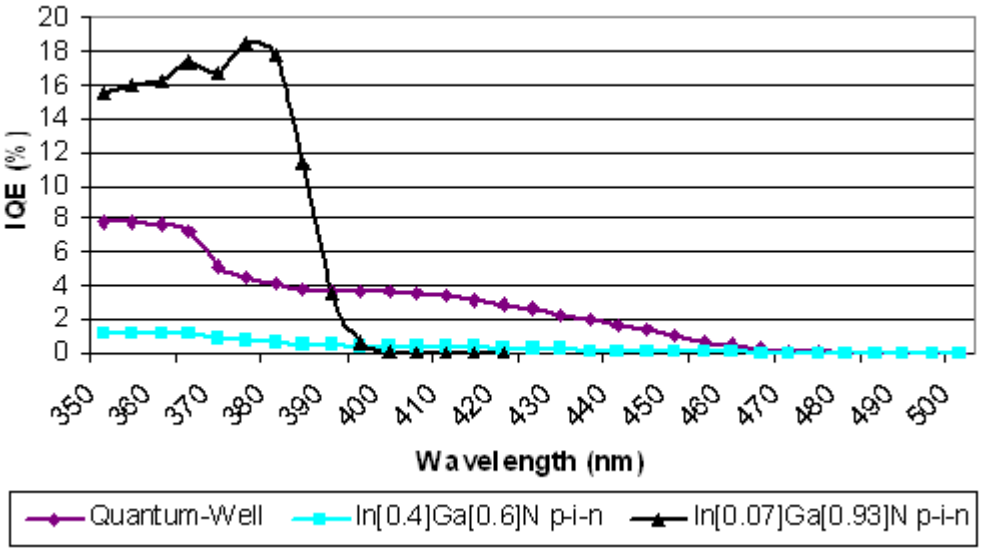

Figure 6.7: Reflection corrected quantum efficiencies of In0.07Ga0.93N p-i-n, In0.4Ga0.6N p-i-n, and In0.4Ga0.6N quantum well solar cells.

A very poor photoresponse is observed from the $In_{0.4}Ga_{0.6}N$ p-i-n solar cell (Figure 6.5(b)) owing to the heavily defective material. A Schottky barrier is also evident under UV illumination, which causes the photogenerated current to drop prior to the V_{OC} condition. The dark I-V curve of the $In_{0.4}Ga_{0.6}N$ QW solar cell is similar to that of the p-i-n device. However, this device provides a greater V_{OC} at 0.5 V compared to the p-i-n device.

The reflection-corrected Quantum Efficiency (QE) data for the solar cells summarized in Figure 6.7 concurs with the I-V measurements. The $In_{0.4}Ga_{0.6}N$ QW device not only provides a better QE of 8% at 365 nm (band edge of GaN) compared to the $In_{0.4}Ga_{0.6}N$ p-i-n device but also demonstrates 4% QE for photon energies less than the band gap of GaN. This sub-band gap QE is attributed to the absorption and collection from $In_{0.4}Ga_{0.6}N$ QW's. The band edge of the $In_{0.4}Ga_{0.6}N$ QW device is extrapolated at 2.7

eV (460 nm), which also corresponds to the transition between the first electron and firs hole levels in the QW. The $In_{0.07}Ga_{0.93}N$ p-i-n device measures a superior QE at 19% at its band edge.

Even though the QW device is not optimized as a solar cell, the better performance signifies the importance of material quality of the device. Moreover, the potential of InGaN as a photovoltaic material is established. The next step in GaN and InGaN solar cell development is to identify the major loss mechanisms and accordingly design subsequent generations of InGaN solar cells.

6.1.2 Identification of major loss mechanisms in InGaN solar cells

InGaN solar cells with low indium compositions, in the 4 – 5% range, are fabricated to identify the major loss mechanisms in such photovoltaic devices. Again, p-i-n devices with the test InGaN material sandwiched between p- and n-GaN junctions are fabricated for this purpose. The three contacting schemes used for the solar cells involve (a) top current

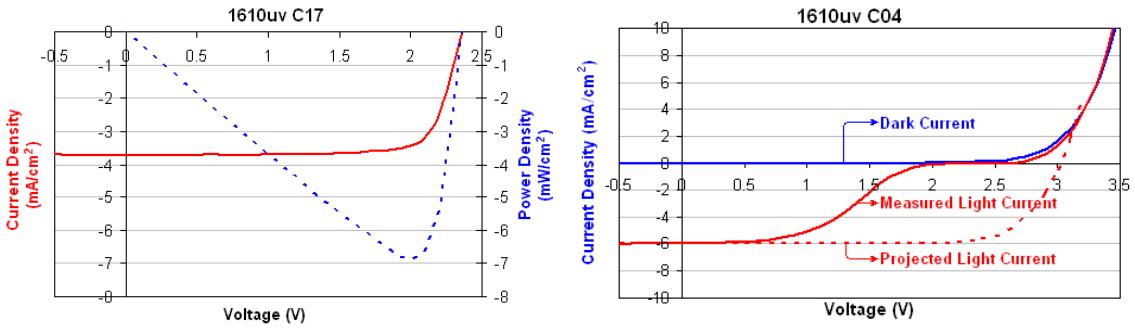

Table 6.1

(a) (b)

Figure 6.8: I-V characteristic of a GaN p-i-n solar cell with In0.05Ga0.95N as the i-region with (a) top current spreading layer, and (b) grid contacts.

spreading layer, (b) interdigitated grid contacts, and (c) solid opaque contacts as explained in Section 5.3.2 (Metal contact schemes), while the fabrication sequence described in Section 5.3.3 (Device processing) is used. The sizes of the fabricated devices are 1 mm x 1 mm, 3 mm x 3 mm, and 5 mm x 5 mm.

A sample I-V curve for the p-i-n solar cell with $In_{0.05}Ga_{0.95}N$ (band gap ~3.2 eV) involving a top current spreading layer is shown in Figure 6.8(a). Even though $In_{0.05}Ga_{0.95}N$ is incorporated as the i-region of the device, phase-separated InGaN with band gap of 2.8 eV dominates the V_{OC} of the device. These solar cells give a V_{OC} of around 2.4 V under UV illumination and a FF of 78%. Although the devices contacted using a grid pattern give higher V_{OC}'s, they encounter a Schottky barrier at the metal contact as shown in Figure 6.8(b), increasing the series resistance and decreasing the overall efficiency of the cell. Moreover, it is observed that the series resistance of solar cells decreases under white light compared to that under dark conditions, and further decrease under UV illumination. This dependence of series resistance is attributed to photogenerated-carriers in both, semiconductor as well as contact material.

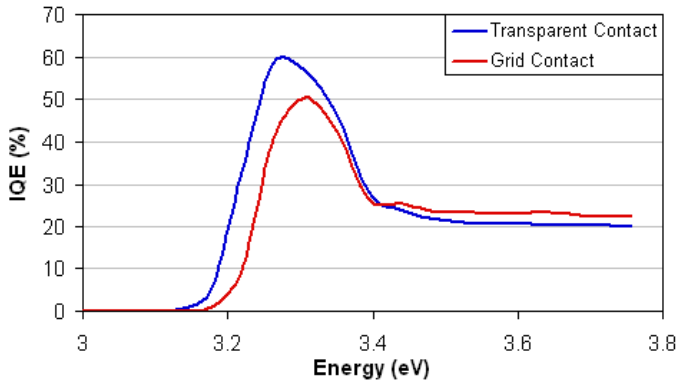

Figure 6.9: IQE of an In0.05Ga0.95N /GaN p-i-n solar cell with as the i-region.

The IQE measurements shown in Figure 6.9 indicate a collection efficiency of 60% for devices with top current spreading layers at the band edge. The sharp QE edge is consistent with the band gap indicated by XRD, PL and the absorption edge of the material. Even though the absorption of light by the p-type current-spreading metal layer is the major loss mechanism, such device still demonstrate a QE greater than that of devices with interdigitated grid contacts by an absolute 10%.

Phase separation in the material is identified as the main mechanism that dominates the V_{OC} of the solar cell, while the decrease in short-circuit current of the device is attributed to defects in the material. The Schottky barriers at the p-contact caused due to non-optimal interdigitated grid contact is a major cause for loss in QE of the p-i-n solar cells, and is the focus of fabrication for subsequent generation devices.

6.1.3 Demonstration of 2.5 eV p-type InGaN for solar cells

While InGaN with band gap as low as 2.5 eV is not used commercially due to associated technological challenges, such band gaps are essential for high-efficiency photovoltaic devices. A solar cell incorporating 2.5 eV p-type InGaN is developed to verify the suitability of InGaN at high indium compositions especially when doped with Mg.

As a first step, MOCVD epitaxy of InGaN is optimized for indium compositions around 30% as explained in Section 5.2. Next, this material is doped with Mg, and after optimizing the annealing conditions, p-type doping of 10^{18} cm^{-3} is determined using Hall measurements. A test device utilizing a 110 nm thick p-type $In_{0.28}Ga_{0.72}N$ is grown on an unintentionally doped n-type GaN template of thickness 2 μm. This epitaxy is fabricated into test solar cells as shown in Figure 6.10 utilizing the fabrication process described in Section 6.3.3.

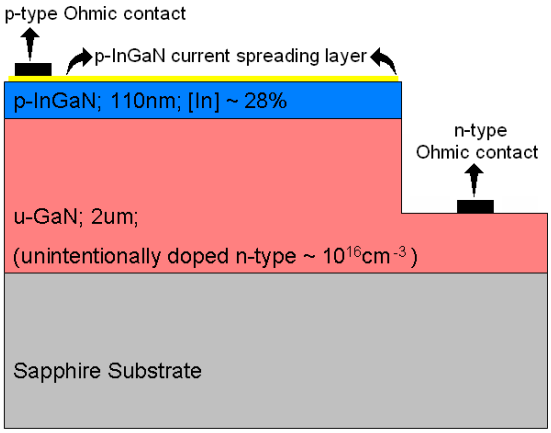

Figure 6.10: Fabricated 2.5 eV In0.28Ga0.72N solar cell.

The material and device are characterized for photovoltaic performance through I-V and IQE measurements as shown in Figure 6.11. The $In_{0.28}Ga_{0.72}N$ solar cells consistently demonstrate a V_{OC} of 2.1 V under an AM 1.5 spectrum enhanced with UV content (Figure 6.11(a)). This is the expected value of V_{OC}, which corresponds to the band gap of the material at 2.5 eV. However, the normalized QE graph (Figure 6.11(b)) indicates very low collection efficiency for photons absorbed in the InGaN region. PC1D simulations of such devices attribute this low collection efficiency to high front surface recombination and high resistivity of the underlying GaN template.

Thus, p-type InGaN at high indium compositions with band gap around 2.5 eV is developed and its suitability for photovoltaic applications is verified. Moreover, the significance of front surface passivation in such devices is established.

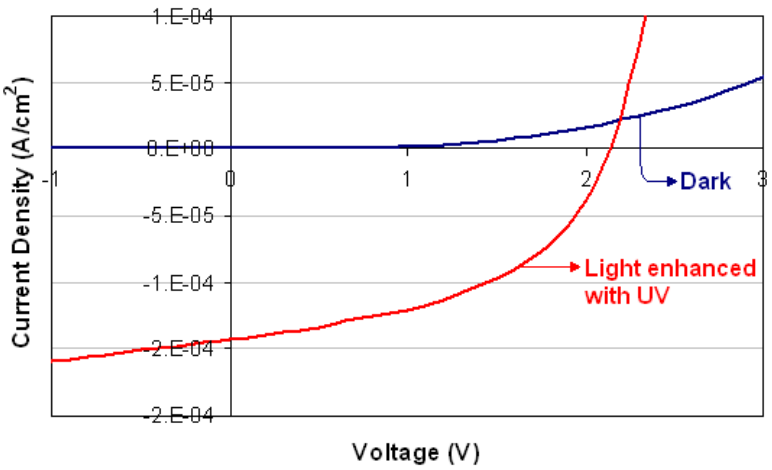

(a)

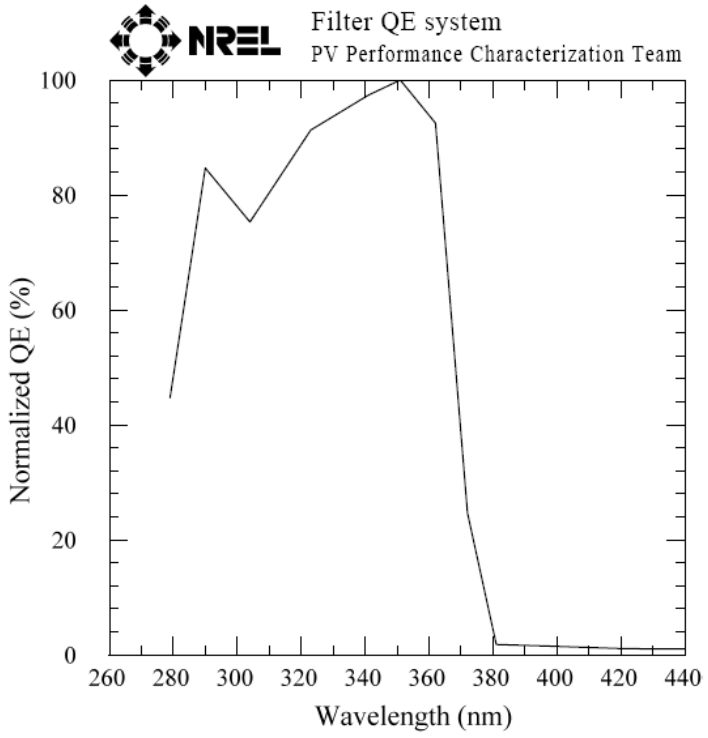

(b)

Figure 6.11: (a) I-V, and (b) QE measurement data of the 2.5 eV In0.28Ga0.72N solar cell.

6.2 ADVANCED INGAN SOLAR CELLS

Once the basic material behavior is established by characterizing standard InGaN/GaN heterojunction solar cells, the next step is to design homojunction InGaN solar cells to confirm the established principles. The band gap of InGaN is fixed at 2.9 eV to ensure reliable material quality in order to confidently verify performance variations dependent solely on design. Solar cells are then iteratively optimized based on experimental results. The development and analysis during this iterative process are summarized in the following subsections.

6.2.1 Evolution of InGaN solar cell design

The evolution of InGaN solar cell designs fabricated and tested is summarized in Figure 6.12. The solar cells are designed, grown by MOCVD, fabricated, characterized and analyzed before designing the next generation of devices.

The p-i-n device structure (Figure 6.12(a)) is taken as the starting point to design subsequent InGaN solar cells due to a detailed understanding obtained from preliminary experiments. The indium composition in the test devices is fixed at 12% (EG – 2.9 eV) to ensure successful p-type and n-type doping. Here, the p- and n-GaN regions are fixed at 100 nm and 500 nm thicknesses, respectively and doped at maximum concentrations without reaching a level of degeneracy. The thickness of the i-region is fixed at 200 nm.

As the i-InGaN region adds to the series resistance of the solar cell, this region is replaced by a p-n InGaN junction in second-generation solar cells as shown in Figure 6.12(b). In this case, the additional electric field generated by the InGaN p-n junction enhances the QE of the solar cell. Moreover, the p-GaN layer not only acts as a window layer for the underlying InGaN p-n junction, but the GaN junctions also induce front and

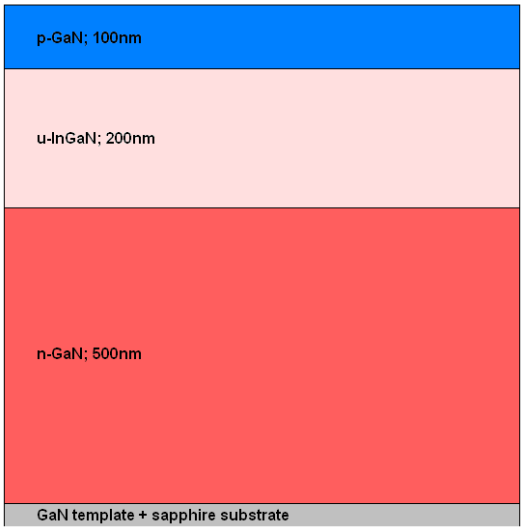

(a) Gen 1: p-i-n structure.

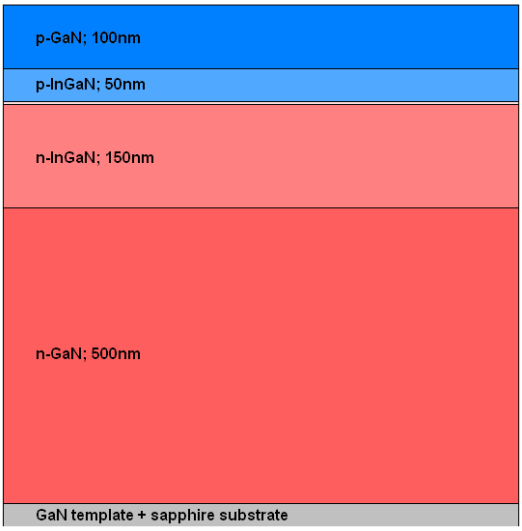

(b) Gen 2: i-InGaN replaced by p-n InGaN.

(c) Gen 3: Thickness of p-GaN reduced.

(d) Gen 4: p-GaN cap replaced by n-GaN.

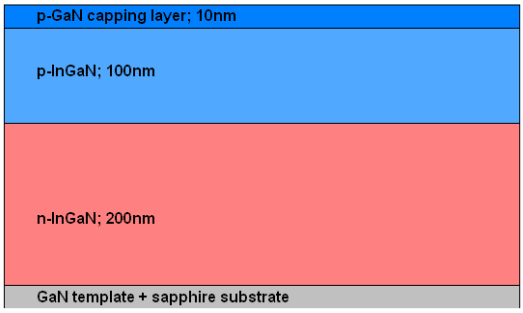

(e) Gen 5: Thickness of InGaN increased.

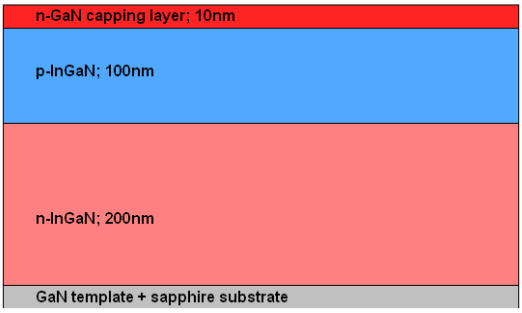

(f) Gen 6: Thickness of InGaN increased.

Figure 6.12: Generations of InGaN solar cell evolution.

back surface fields for this device. The thicknesses of p- and n-InGaN are set to 50 nm and 150 nm, respectively to maintain a net InGaN thickness of 200 nm.

The I-V curves for the second-generation InGaN devices show a substantial improvement in short-circuit current of the solar cell compared to the first-generation devices as shown in Figures 6.13(a) and (b). The increase in short-circuit current is supported by the increase in internal quantum efficiency of the second generation devices up to 50% as seen in Figure 6.14. It should be noted that this 50% internal quantum efficiency measurement did not take transmission of light through the sample into account. It is estimated that a 200 nm thick InGaN layer transmits at least 14% of light entering the layer; which amounts to a corrected internal quantum efficiency of at least 58%. However, there is a decrease in the open-circuit voltage due to reduction in quasi-fermi level energy difference caused by additional doping in the InGaN junctions and/or formation of phase-separated defects.

The third-generation InGaN devices are designed to minimize the voltage loss caused by the p-GaN window layer due to its high resistivity. Hence, the thickness of the p-GaN window layer is reduced from 100 nm to 10 m as shown in Figure 6.12(c). However, the 50 nm p-InGaN layer is not thick enough to provide charge to the depletion region, which results into an incomplete junction formation. Hence, these solar cells measure very low open-circuit voltages and quantum efficiencies.

The fourth-generation devices are designed to enhance the window layer by replacing the 10 nm p-GaN with n-GaN. The strained window layer forms a 2DEG at the n-GaN/p-InGaN interface as explained in Section 4.2.2 improving the lateral conduction in the material, while the n-GaN window enhances tunneling to reduce the top contact

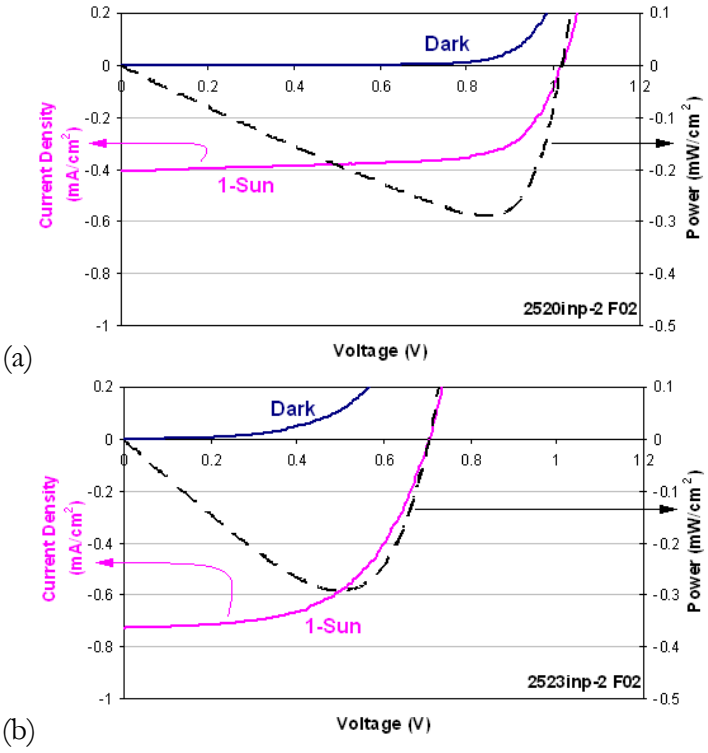

Figure 6.13: Sample I-V characteristics of (a) first-generation, and (b) second generation test solar cells.

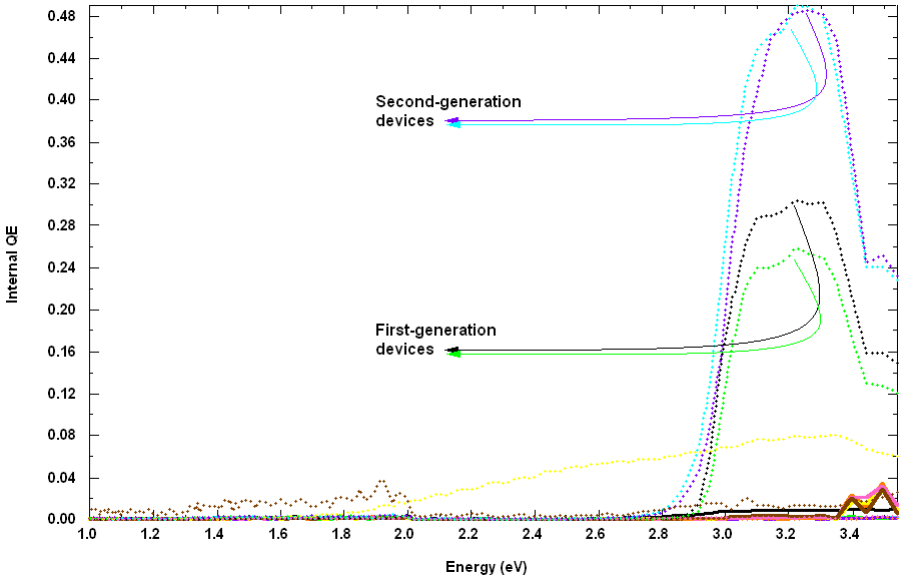

Figure 6.14: Internal quantum efficiency comparison of first and second-generation test solar cells.

resistance of the device. However, these devices also fail to provide substantial open-circuit voltage and quantum efficiency due to incomplete charge provision by the thin p-junctions.

The next generation solar cells are designed to overcome the limitations caused by the thin p-type InGaN junctions. Here, the thickness of InGaN p-n junction is increased to 300 nm, where the thickness of p- and n- InGaN are designed at 100 nm and 200 nm, respectively. The fifth and sixth-generation solar cells employ a 10 nm thick p- and n-GaN window layer, respectively. These devices yield a substantially higher performance compared to the fourth and fifth- generation devices.

Highest open-circuit voltages are obtained from the sixth-generation solar cells, which employ a thin n-GaN tunneling window layer. While the p-GaN window layers form a piezoelectrically-induced 2DEG that causes a trap for holes and hinder collection, the n-GaN window layers take advantage of this 2DEG by enhancing tunneling as shown in Figure 6.15. Moreover, the 2DEG, in conjunction with higher doping capability in n-GaN,

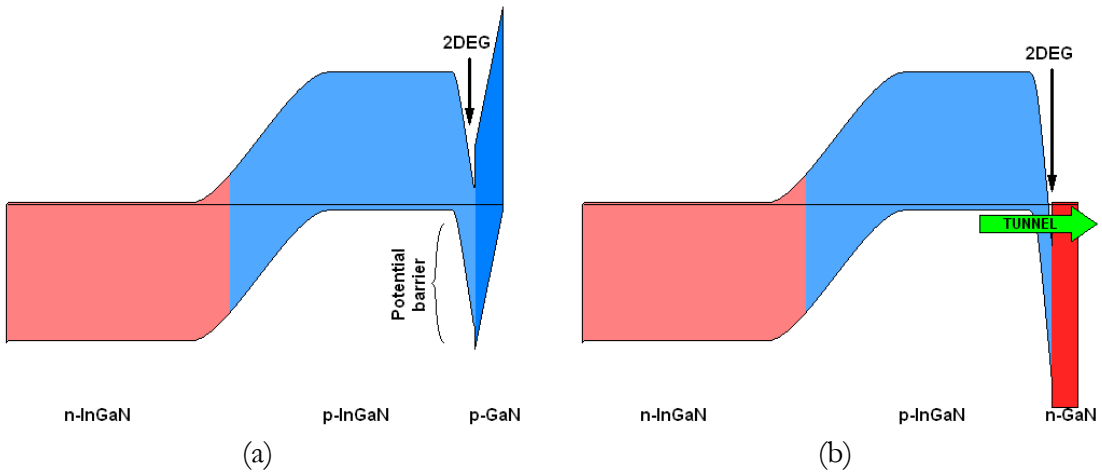

Figure 6.15: Schematic comparison of band diagrams of (a) fifth (p-GaN window), and (b) sixth-generation (n-GaN window) solar cells.

Table 6.2: Summary of InGaN test solar cell performance for consecutive generations.

Gen.	**Salient Features**	**V_{oc}**	**IQE**	**Observation**
1	Preliminary p-i-n design.	1.02 V	30%	Low V_{OC} and IQE.
2	i-InGaN replaced with InGaN p-n junction.	0.71 V	**50%**	Improved IQE but decrease in V_{OC}.
3	Thickness of p-GaN window reduced.	Poor	Poor	Insufficient p-junction thickness.
4	p-GaN window replaced by n-GaN window.	Poor	Poor	Insufficient p-junction thickness.
5	Thickness of InGaN junction increased from 200 nm to 300 nm. Window layer is p-GaN.	0.16 V	Poor	Piezoelectric barrier at top contact.
6	p-GaN window replaced by n-GaN window.	**2 V**	Poor	Substantial improvement in V_{OC} due to tunneling contact.

provides better lateral conduction, which relaxes the grid spacing requirement in the final solar cell structure.

Thus, using progressive design modifications, methods to increase both, quantum efficiency as well as open-circuit voltage, are established. A summary of device performance for the consecutive generations of test solar cells is presented in Table 6.1. The systematic variations observed in the various generations of InGaN solar cells can be used to further the efficiency of InGaN photovoltaic devices.

6.2.2 Optimization of n-GaN strained window layer

It is uncommon in solar cells to use an n-type window layer for a top p-type active junction on top. Moreover, typical contacting schemes in III-nitride LED's, laser diodes, photodetectors and solar cells, are optimized for p-type GaN and InGaN junctions or window layers. Hence, additional metallization schemes are now investigated to enhance tunneling and minimize contact resistance for strained n-GaN window layers. Two basic contacting schemes are investigated in order to enhance tunneling through the n-GaN layer. While Ni/Au, which is used as the top p-type contact metal for conventional InGaN devices, is used in the first metallization scheme, a second batch of devices employing Ti/Al/Ti/Au,

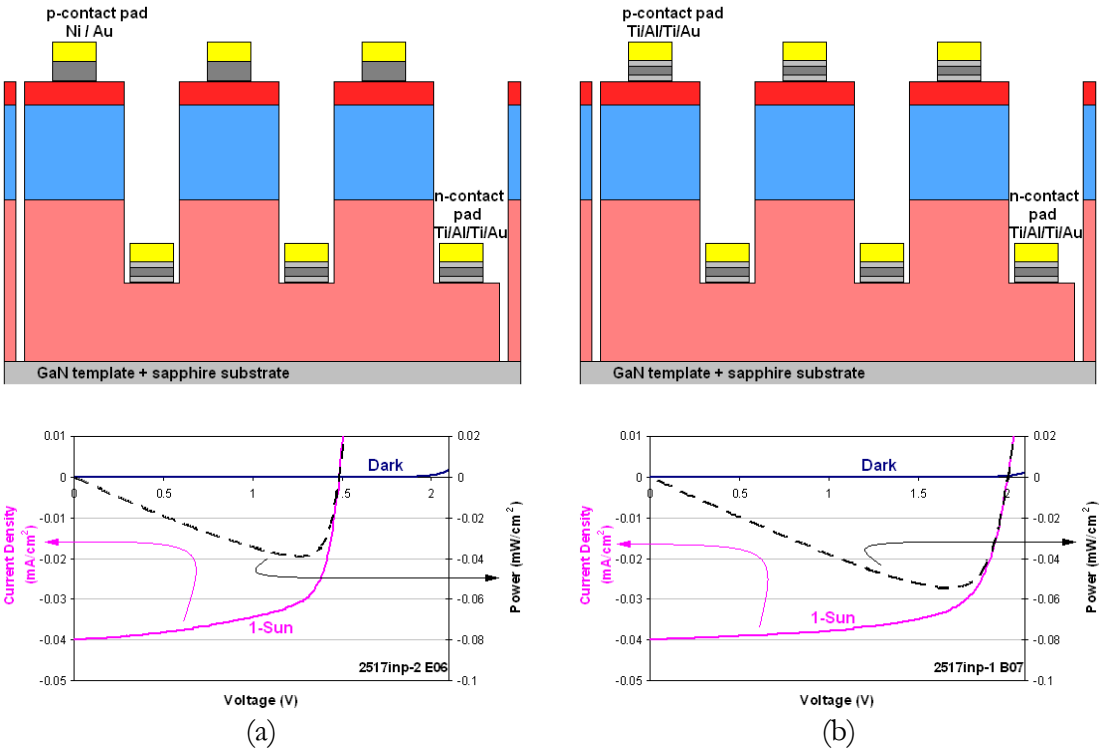

Figure 6.16: Comparison of I-V curves for sixth-generation test solar cells employing (a) Ni/Au, and (b) Ti/Al/Ti/Au as top contacts.

which is typically used to contact the bottom n-type material [121][122], as the top contact to n-GaN is fabricated. The two contacting schemes and corresponding sample I-V curves are shown in Figures 6.16(a) and (b). The superiority of the n-GaN tunneling window layer with Ti/Al/Ti/Au to contact is established with a measured open-circuit voltage of 2 V.

6.3 SUMMARY

Once the challenges in InGaN material and device design are identified and optimized independently, the next step is to develop InGaN solar cells by comprehensively optimize them. Preliminary InGaN solar cell development is based on optimizing the InGaN material by progressively increasing indium compositions to lower its band gap in a p-i-n heterostructure with GaN junctions. P-type InGaN with band gap as low as 2.5 eV ([In] = 28%) and carrier concentration of 10^{18} cm^{-3} is successfully tested for photovoltaic applications by incorporating in a p-n heterojunction solar cell and measuring an open-circuit voltage of 2.1 V. The next stage of InGaN solar cell development involves progressive modifications to the preceding solar cell design after simulations, growth by MOCVD, fabrication, characterization and analysis to improve the internal quantum efficiency and open circuit voltage. Second generation InGaN test solar cells demonstrate internal quantum efficiencies as high as 50% by incorporating a p-n InGaN homojunction between p- and n-GaN junctions. Sixth generation devices demonstrate open circuit voltages up to 2 V using a novel n-GaN strained window layer and Ti/Al/Ti/Au top contact, which forms a piezoelectrically-enhanced tunneling contact. The derived principles can further be integrated and optimized to enhance the performance of next generation InGaN solar cells.

7. CONCLUSION

7.1 OVERVIEW OF CONTRIBUTION IN INGAN PHOTOVOLTAICS

The present work achieves some of the fundamental milestones in the field of III-nitride photovoltaics. The novel III-nitride is one of the few material systems that theoretically offer the potential to achieve photovoltaic conversion efficiencies greater than 50%. While the III-nitrides are commercially employed in light emitting diodes, laser diodes and photodetectors, no substantial practical work was shown in the field of photovoltaics prior to this work due to fundamental challenges associated with it.

A fundamental challenge involved in the use of III-nitrides, including InGaN, is maintaining material crystallinity at higher indium compositions; it is imperative to incorporate indium in the III-nitrides to sufficiently lower its band gap for photovoltaic applications. This challenge is overcome by optimizing the MOCVD growth process, mainly gas flow rates, pressure and growth rate, to obtain InGaN with indium compositions up to 30% suitable for photovoltaic applications.

Another technological challenge involved at high indium compositions is to obtain p-type conductivity due to the low activation efficiency associated with Mg dopants. This challenge is overcome by controlling Mg incorporation during the growth process and optimization of dopant activation conditions.

Owing to the recent entry of this material in photovoltaics, no software is commercially available to simulate III-nitride solar cells. Moreover, available solar cell

simulation programs do not incorporate uncommon phenomena such as polarization, which can have substantial effect on III-nitride device behavior. The lack of an accurate simulation tool is overcome by modifying an existing solar cell simulation program, PC1D, from its source code to handle user defined subroutines to calculate polarization effects.

Among fundamental challenges involved in InGaN device fabrication is developing a low resistance Ohmic contact to p-type InGaN with high light transmittivity. This is a challenge because there is no readily available metal with work function high enough to form an Ohmic contact to p-type InGaN. Moreover, due to the high resistivity of the material, theoretical values for optimal grid spacing result up to 50% shading losses. This challenge is overcome using tunnel junctions, where not only is the tunneling aided by a piezoelectrically-induced 2DEG, but also the 2DEG aids lateral conduction of carriers relaxing the solar cell grid spacing constraint.

As the material quality, which includes factors such as defect density and phase separation, has a direct impact on the performance of the solar cell, it becomes imperative to minimize its effect. This challenge is met by studying the sensitivity of solar cell performance to material quality and designing robust InGaN solar cells by increasing internal junction and polarization fields and enhancing carrier transport in accordance to diffusion lengths.

Innovative methods applicable to the III-nitrides are also investigated in this work. Extremely difficult materials to grow, such as InGaN with 40% indium composition, which are heavily defected in their bulk state to be used in solar cells, can be incorporated in the form of superlattice to maintain their crystalline quality. Another counterintuitive method developed to contact p-InGaN is using a strained n-GaN window layer as explained earlier.

Table 7.1: Summary of contribution to InGaN photovoltaics in present work.

	Challenge	**Contribution**
1	Obtaining photovoltaic quality InGaN for high indium compositions.	Optimized MOCVD growth conditions for indium composition up to 30%.
2	Achieving p-type conductivity at high indium compositions.	Optimized Mg incorporation during growth and activation conditions to achieve p-type carrier concentrations up to 10^{18} cm^{-3} and 10^{19} cm^{-3} for indium compositions of 28% and 15%, respectively.
3	Lack of availability of simulation software for III-nitride solar cells and uncommon phenomena such as polarization.	Developed material files and modified source code of PC1D to incorporate III-nitrides and simulate polarization.
4	Develop Ohmic contacts to p-type InGaN.	Used band engineering by enhancing tunnel junction with piezoelectrically-induced 2DEG and improvised metallization scheme to obtain Ohmic contacts to p-InGaN.
5	Minimize sensitivity of solar cell performance due to material quality.	Developed robust solar cell design by enhancing junction fields and constructively utilizing polarization fields.
6.	Explore innovative methods to enhance device performance.	Established suitability of difficult-to-grow InGaN to be incorporated in superlattice. Designed counterintuitive strained n-GaN window layer for top p-InGaN junction.

The novel contribution in the present work is summarized in Table 7.1. Advances in this work have established InGaN as a successful photovoltaic material yielding consistent performance (Figure 7.1). Moreover, the understanding gathered here paves the path for the future of InGaN photovoltaics.

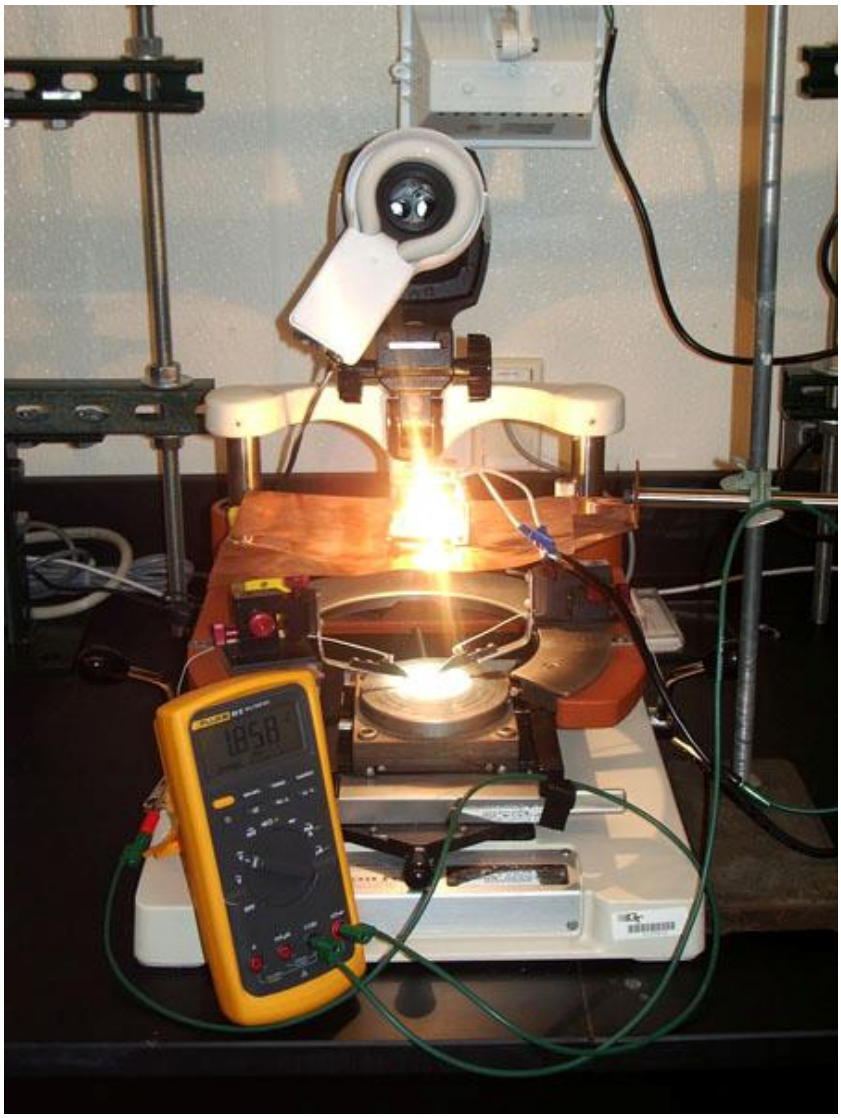

Figure 7.1: InGaN solar cell with VOC of 1.858 V measured using a multimeter under a 1-Sun simulator.

7.2 RECOMMENDATION FOR FURTHER WORK

7.2.1 Integration of present work

While the present work aims at enhancing individual aspects of InGaN solar cell performance such as open-circuit voltage and internal quantum efficiency, future work

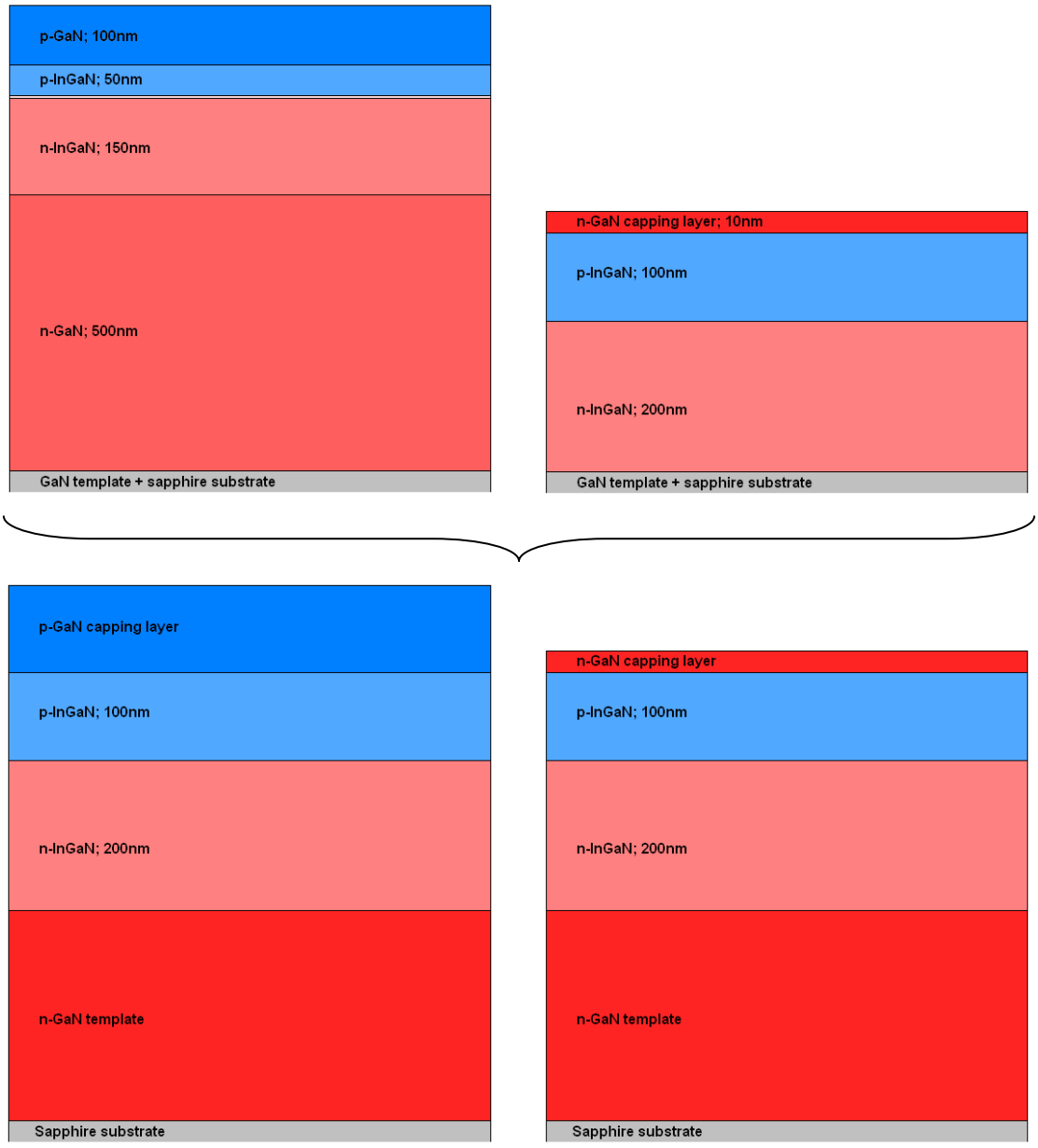

Figure 7.2: Integrated solar cell design to yield higher performance.

should involve integrating the established principles to improve the net efficiency of the solar cell. An example is illustrated in Figure 7.2, where the design of the solar cell with high quantum efficiency is integrated with that measuring high open-circuit voltage.

7.2.2 Optimize the top contacting scheme

The n-GaN strained tunneling window layer developed in this work may need further optimization in terms of thickness to minimize series resistance while maintaining the open-circuit voltage of the solar cell. This window layer may further be replaced by a short-period-superlattice structure to possibly reduce contact resistance and enhance lateral conductivity of the device.

7.2.3 Lower band gap of InGaN to increase absorption

The primary factor to increase the overall efficiency of the InGaN solar cell is to further lower the band gap of the material so that it absorbs a substantial fraction of the incident light. The solar cell can then be optimized by following the iterative development process involving design, growth, fabrication, characterization and analysis as explained in this work.

7.2.4 Improve convergence of the modified PC1D software

A polarization sub-routine is incorporated in the source code of PC1D in the present work. The strong polarization charge densities often cause substantial spikes in carrier concentrations as well as energy bands. The PC1D solver is not optimized for such

uncommon behavior of the material, and fails to converge the solution. Hence, in order to make PC1D more robust, it is strongly recommended to upgrade the convergence algorithm in PC1D to handle polarization.

7.3 SUMMARY

All the primary challenges for III-nitride photovoltaics have been identified and overcome. More importantly, the present work has identified methods to improve the open-circuit voltage as well as the quantum efficiency of InGaN solar cells in spite of material limitations. Additionally, a future course of action is suggested to take advantage of this work and effectively carry the research forward.

APPENDIX A: PC1D files for III-nitrides

	Material				
	GaN	**In0.05Ga0.95N**	**In0.2Ga0.8N**	**InN**	**AlN**
Band Structure					
Band Gap (eV)	3.42	3.215	2.642	0.65	6.2
Electron Affinity (eV)	4.1	4.24825	4.672	6.4	2
Nc/Nv Ratio	0.03876377	0.03783557	0.03486388	0.01642381	0.01907207
Intrinsic Concentration: 200 K (cm^{-3})	5.82E-25	2.16E-22	3.27E-15	2.58E+10	2.49E-59
Intrinsic Concentration: 300 K (cm^{-3})	2.35E-10	1.21E-08	7.21E-04	2.52E+13	4.57E-33
Intrinsic Concentration: 400 K (cm^{-3})	0.00536845	0.10229024	384.969503	8.94E+14	7.05E-20
Dielectric Constant					
Dielectric Constant	8.9	9.22	10.18	15.3	8.5
Mobility					
Electron Mobility (cm^2/Vs)	400 (Fixed)	400 (Fixed)	400 (Fixed)	400 (Fixed)	400 (Fixed)
Hole Mobility (cm^2/Vs)	10 (Fixed)	10 (Fixed)	10 (Fixed)	10 (Fixed)	10 (Fixed)
Optical Constants					
Refractive Index	2.29 (Fixed)	2.3205 (Fixed)	2.412 (Fixed)	2.9 (Fixed)	2.15 (Fixed)

Intrinsic Absorption	GaN.abs	In05Ga95N.abs	In20Ga80N.abs	InN.abs	(Disabled)
Free-Carrier Absorption	(Disabled)	(Disabled)	(Disabled)	(Disabled)	(Disabled)
Doping					
Background Doping (cm^{-3})	10^{16} (n-type)	10^{16} (n-type)	10^{16} (n-type)	10^{16} (n-type)	10^{16} (n-type)
Recombination Parameters					
Bulk Recombination: tau-n (µs)	2×10^{-3}	2×10^{-3}	2×10^{-3}	2×10^{-3}	2×10^{-3}
Bulk Recombination: tau-p (µs)	2×10^{-3}	2×10^{-3}	2×10^{-3}	2×10^{-3}	2×10^{-3}
Front Surface	Variable	Variable	Variable	Variable	Variable
Rear Surface	Variable	Variable	Variable	Variable	Variable
Band Gap Narrowing Model					
n-type: onset (cm^{-3})	1×10^{20}	1×10^{20}	1×10^{20}	1×10^{20}	1×10^{20}
n-type: slope (meV)	15	15	15	15	15
p-type: onset (cm^{-3})	1×10^{18}	1×10^{18}	1×10^{18}	1×10^{18}	1×10^{18}
p-type: slope (meV)	15	15	15	15	15
Recombination Coefficients					
Bulk Doping Influence: N-type onset (cm^{-3})	1×10^{20}	1×10^{20}	1×10^{20}	1×10^{20}	1×10^{20}
Bulk Doping Influence: N-type alpha	0	0	0	0	0
Bulk Doping Influence: P-type onset (cm^{-3})	1×10^{18}	1×10^{18}	1×10^{18}	1×10^{18}	1×10^{18}
Bulk Doping Influence: P-type alpha	0	0	0	0	0
Surface Doping Influence: N-type onset (cm^{-3})	1×10^{20}	1×10^{20}	1×10^{20}	1×10^{20}	1×10^{20}

Surface Doping Influence: N-type alpha	0	0	0	0	0
Surface Doping Influence: P-type onset (cm^{-3})	1×10^{18}	1×10^{18}	1×10^{18}	1×10^{18}	1×10^{18}
Surface Doping Influence: P-type alpha	0	0	0	0	0
Auger Coefficients: n-type (cm^6/s)	1.4×10^{-30}	1.4×10^{-30}	1.4×10^{-30}	1.4×10^{-30}	1.4×10^{-30}
Auger Coefficients: p-type (cm^6/s)	1.4×10^{-30}	1.4×10^{-30}	1.4×10^{-30}	1.4×10^{-30}	1.4×10^{-30}
Auger Coefficients: high-inject (cm^6/s)	1.4×10^{-30}	1.4×10^{-30}	1.4×10^{-30}	1.4×10^{-30}	1.4×10^{-30}
Band-to-Band (cm^3/s)	2.4×10^{-11}	2.31×10^{-11}	2.05×10^{-11}	6.6×10^{-11}	2.0×10^{-11}
Temperature Influence Exponent: Tau	-0.5	-0.5	-0.5	-0.5	-0.5
Temperature Influence Exponent: S	0.5	0.5	0.5	0.5	0.5
Hurkx Model	(Disabled)	(Disabled)	(Disabled)	(Disabled)	(Disabled)
Polarization Coefficients					
Spontaneous Polarization: P_{SP} (C/m^2)	-0.034	-0.03264	-0.02968	-0.042	-0.09
Piezoelectric Constant: e_{31} (C/m^2)	0.73	0.742	0.778	0.97	1.55
Piezoelectric Constant: e_{33} (C/m^2)	-0.49	-0.494	-0.506	-0.57	-0.58
Elastic Constant: c_{13} (Gpa)	103	102.45	100.8	92	108
Elastic Constant: c_{13} (Gpa)	405	395.95	368.8	224	373
Lattice Constant: a (Å)	3.189	3.2062	3.2578	3.533	3.112

GaN.abs		$In_{0.05}Ga_{0.95}N$.abs		$In_{0.2}Ga_{0.8}N$.abs		InN.abs	
200	172112	200	171100	200	163071	200	91954
202	171944	202	171040	202	163237	202	92283
203	171758	203	170967	203	163398	203	92616
205	171555	205	170879	205	163553	205	92952
207	171332	207	170777	207	163702	207	93291
208	171089	208	170659	208	163844	208	93635
210	170826	210	170525	210	163979	210	93982
212	170540	212	170374	212	164107	212	94332
214	170232	214	170204	214	164226	214	94687
216	169899	216	170016	216	164338	216	95046
218	169540	218	169807	218	164440	218	95408
219	169155	219	169578	219	164534	219	95775
221	168741	221	169326	221	164617	221	96146
223	168297	223	169051	223	164691	223	96521
225	167822	225	168752	225	164753	225	96900
228	167314	228	168427	228	164804	228	97284
230	166770	230	168074	230	164842	230	97672
232	166190	232	167692	232	164868	232	98064
234	165571	234	167281	234	164879	234	98461
236	164910	236	166837	236	164877	236	98863
238	164205	238	166359	238	164859	238	99270
241	163454	241	165845	241	164824	241	99681
243	162654	243	165293	243	164773	243	100098
246	161801	246	164701	246	164703	246	100520
248	160894	248	164066	248	164614	248	100946
251	159927	251	163385	251	164504	251	101378
253	158897	253	162657	253	164373	253	101815
256	157800	256	161877	256	164219	256	102258
258	156631	258	161043	258	164040	258	102707
261	155386	261	160151	261	163835	261	103161
264	154059	264	159197	264	163602	264	103620
267	152644	267	158176	267	163340	267	104086
270	151134	270	157085	270	163047	270	104558
273	149523	273	155918	273	162721	273	105036
276	147802	276	154670	276	162359	276	105520
279	145962	279	153335	279	161959	279	106010
282	143993	282	151906	282	161518	282	106507
285	141884	285	150375	285	161035	285	107011
288	139622	288	148736	288	160505	288	107521
292	137192	292	146977	292	159926	292	108038
295	134579	295	145090	295	159294	295	108563
299	131763	299	143063	299	158605	299	109094
302	128721	302	140882	302	157855	302	109633
306	125428	306	138534	306	157040	306	110179
310	121852	310	136001	310	156155	310	110733

314	117956	314	133265	314	155193	314	111295
318	113694	318	130301	318	154149	318	111865
322	109007	322	127085	322	153016	322	112442
326	103822	326	123584	326	151787	326	113028
331	98041	331	119761	331	150454	331	113623
335	91529	335	115568	335	149007	335	114226
340	84091	340	110948	340	147436	340	114837
344	75425	344	105827	344	145729	344	115458
349	65001	349	100107	349	143873	349	116088
354	51720	354	93653	354	141854	354	116727
359	32131	359	86275	359	139653	359	117375
365	1	365	77674	365	137253	365	118033
370	1	370	67343	370	134628	370	118700
376	1	376	54246	376	131754	376	119378
382	1	382	35344	382	128598	382	120066
388	1	388	1	388	125121	388	120763
394	1	394	1	394	121279	394	121472
400	1	400	1	400	117013	400	122190
407	1	407	1	407	112252	407	122920
413	1	413	1	413	106902	413	123660
420	1	420	1	420	100837	420	124411
428	1	428	1	428	93881	428	125172
435	1	435	1	435	85773	435	125945
443	1	443	1	443	76091	443	126729
451	1	451	1	451	64054	451	127524
459	1	459	1	459	47810	459	128330
468	1	468	1	468	18091	468	129147
477	1	477	1	477	1	477	129975
486	1	486	1	486	1	486	130813
496	1	496	1	496	1	496	131662
506	1	506	1	506	1	506	132521
517	1	517	1	517	1	517	133390
528	1	528	1	528	1	528	134268
539	1	539	1	539	1	539	135154
551	1	551	1	551	1	551	136048
564	1	564	1	564	1	564	136949
577	1	577	1	577	1	577	137855
590	1	590	1	590	1	590	138765
605	1	605	1	605	1	605	139677
620	1	620	1	620	1	620	140589
636	1	636	1	636	1	636	141499
653	1	653	1	653	1	653	142402
670	1	670	1	670	1	670	143296
689	1	689	1	689	1	689	144176
709	1	709	1	709	1	709	145035
729	1	729	1	729	1	729	145868
752	1	752	1	752	1	752	146667
775	1	775	1	775	1	775	147420

800	1	800	1	800	1	800	148117
827	1	827	1	827	1	827	148742
855	1	855	1	855	1	855	149277
886	1	886	1	886	1	886	149699
919	1	919	1	919	1	919	149979
954	1	954	1	954	1	954	150082
992	1	992	1	992	1	992	149962
1033	1	1033	1	1033	1	1033	149560
1078	1	1078	1	1078	1	1078	148800
1127	1	1127	1	1127	1	1127	147580
1181	1	1181	1	1181	1	1181	145766
1240	1	1240	1	1240	1	1240	143169
1305	1	1305	1	1305	1	1305	139525
1378	1	1378	1	1378	1	1378	134444
1459	1	1459	1	1459	1	1459	127324
1550	1	1550	1	1550	1	1550	117158
1653	1	1653	1	1653	1	1653	102036
1771	1	1771	1	1771	1	1771	77304
1908	1	1908	1	1908	1	1908	1
2067	0	2067	0	2067	0	2067	0

APPENDIX B: Fabrication procedure for InGaN/GaN solar cells

The following fabrication recipe is developed for a typical InGaN/GaN homojunction/heterojunction p-n/p-i-n solar cell shown in Figure 5.12.

Apparatus

1) **Facilities:**
   - Cleanroom with basic facilities
   - Wet bench (part of the cleanroom)
2) **Materials:**
   - Relevant mask sets
   - Cleanroom supplies: tweezers, wipes, etc.
3) **Chemicals:**
   - Cleaning: Acetone, Methanol, DI Water
   - N_2 (to blow dry)
   - Photoresist: Shipley® S1813, S1827
   - Developer: Shipley® MF-319
   - Buffered Oxide Etch (BOE)
4) **Tools:**
   - **RTA/RTP:** AET addax RX RTP
     - Temperature requirement: up to 800°C
     - Gases: N_2, O_2, air
   - **Mask Aligner:** Karl Suss MA6
     - Should accommodate: Wafer size 2”
     - Should accommodate: Mask size 4”
     - Minimum resolution: 0.5 - 1µm
     - Typical exposure wavelength – 405nm
   - **Etcher:** Plasma-Therm Inductively Coupled Plasma (ICP) Etcher
     - Should etch III-Nitrides (Cl_2 diluted in Ar)
     - Should incorporate appropriate wafer size
     - Etch rate of photoresists used for masking should be known for the process
     - Etch depths: 0.5 - 3µm
     - Gases: Cl_2, Ar, N_2
   - **E-Beam Evaporator:** CVC Electron Beam Evaporator
     - Metals: Ni, Au, Ti, Al
   - **Profilometer:** Tencor KLA profilometer

Process

1) **High temperature anneal - RTA:** to activate Mg acceptor in p-GaN.
    - Anneal temperature: 800°C
    - Anneal time: 4 minutes
    - Anneal ambient: N_2

2) **Isolation – photolithography:** to transfer isolation pattern on wafer.
    - Photoresist: Positive → Microposit® S1827
    - Spin: speed 3000RPM, time 50s, ramp rate 100RPM/s → 3µm thickness
    - Soft-bake: 3min @ 100°C on hot plate
    - Mask aligner: Karl Suss MA6
    - Mask: Isolation mask
    - Expose: 22sec @ 405nm ($21mW/cm^2$ x 22sec = $460mJ/cm^2$)
    - Develop: Microposit® MF-319 developer for 15 - 20sec (or as soon as pattern is visible.) (Mild agitation required.)
    - IMMEDIATELY remove and rinse in DI water
    - Dry with N_2

3) **Isolation etch – ICP/RIE etcher:** to isolate each device on the wafer. The wafer is etched up to the substrate.
    - Cure: 30min @ 120°C in oven
    - Check thickness of photoresist layer using profilometer → thickness of this layer should be greater than the depth to be etched.
    - Etch: sample up to substrate (~2.5µm)
    - Strip photoresist using acetone and ultrasonic bath for ~15min
    - Clean: Acetone → Methanol → DI Water → N_2
    - Check depth of etched trench using profilometer.

4) **Mesa – photolithography:** to transfer mesa pattern on wafer. The wafer is etched 100nm deep into the n-layer.
    - Photoresist: Positive → Microposit® S1813
    - Spin: speed 4000RPM, time 30s, ramp rate 500RPM/s → 1.3µm thickness
    - Soft-bake: 3min @ 100°C on hot plate
    - Mask aligner: Karl Suss MA6
    - Mask: Isolation mask
    - Expose: 10sec @ 405nm ($21mW/cm^2$ x 10sec = $210mJ/cm^2$)
    - Develop: Microposit® MF-319 developer for 15 - 20sec (or as soon as pattern is visible.) (Mild agitation required.)
    - IMMEDIATELY remove and rinse in DI water.
    - Dry with N_2

5) **Mesa etch:** to form p-GaN mesas on wafer. The wafer is etched 100nm deep into the n-layer.
    - Cure: 30min @ 120°C in oven

- Check thickness of photoresist layer → thickness of this layer should be greater than the depth to be etched.
- Etch: sample up to substrate (~2.5µm)
- Strip photoresist using acetone and ultrasonic bath for ~15min
- Clean: Acetone → Methanol → DI Water → N_2
- Check depth of etched trench using profilometer.

6) **N-Ohmic contact mask – photolithography:** to transfer n-Ohmic contact pattern on wafer for lift off.
   - Photoresist: Positive → Microposit® S1813
   - Spin: speed 4000RPM, time 30s, ramp rate 500RPM/s → 1.3µm thickness
   - Soft-bake: 3min @ 100°C on hot plate
   - Mask aligner: Karl Suss MA6
   - Mask: Isolation mask
   - Expose: 10sec @ 405nm (21mW/cm^2 x 10sec = 210mJ/cm^2)
   - Develop: Microposit® MF-319 developer for 15 - 20sec (or as soon as pattern is visible.) (Mild agitation required.)
   - IMMEDIATELY remove and rinse in DI water.
   - Dry with N_2

7) **N-Ohmic contact deposition – E-beam:** to deposit n-Ohmic contact metal
   - Surface oxide removal: Immerse in BOE:H_2O (1:6) solution for 30 seconds. (Mild agitation optional.)
   - Deposit: 10nm Ti → 20nm Al → 50nm Pt (OR Ti, Pd, Cr) → 20nm Au
   - Strip photoresist with excess metal using acetone and ultrasonic bath for ~15min.
   - Clean: Acetone → Methanol → DI Water → N_2
   - Check thickness of metal thickness using profilometer.

8) **N-Ohmic contact anneal - RTA:** Recipe - GANSC_N
   - Anneal temperature: 600°C
   - Anneal time: 1 minutes
   - Anneal ambient: N_2

9) **P-current spreading layer mask – photolithography:** to transfer p-current spreading layer pattern on wafer for lift off.
   - Photoresist: Positive → Microposit® S1813
   - Spin: speed 4000RPM, time 30s, ramp rate 500RPM/s → 1.3µm thickness
   - Soft-bake: 3min @ 100°C on hot plate
   - Mask aligner: Karl Suss MA6
   - Mask: Isolation mask
   - Expose: 10sec @ 405nm (21mW/cm^2 x 10sec = 210mJ/cm^2)
   - Develop: Microposit® MF-319 developer for 15 - 20sec (or as soon as pattern is visible.) (Mild agitation required.)
   - IMMEDIATELY remove and rinse in DI water.

- Dry with N_2

10) **P-current spreading layer deposition – E-beam:** to deposit p-current spreading layer metal.
    - Surface oxide removal: Immerse in BOE:H_2O (1:6) solution for 30 seconds. (Mild agitation optional.)
    - Deposit: 5nm Ni → 5nm Au
    - Strip photoresist with excess metal using acetone and ultrasonic bath for ~15min.
    - Clean: Acetone → Methanol → DI Water → N_2
    - Check thickness of metal thickness using profilometer.

11) **P-current spreading layer anneal:** Recipe - GANSC_P
    - Anneal temperature: 530°C
    - Anneal time: 1 minutes
    - Anneal ambient: O_2

12) **Contact pad mask – photolithography:** to transfer contact pad pattern on the wafer for lift-off.
    - Photoresist: Positive → Microposit® S1813
    - Spin: speed 4000RPM, time 30s, ramp rate 500RPM/s → 1.3µm thickness
    - Soft-bake: 3min @ 100°C on hot plate
    - Mask aligner: Karl Suss MA6
    - Mask: Isolation mask
    - Expose: 10sec @ 405nm (21mW/cm^2 x 10sec = 210mJ/cm^2)
    - Develop: Microposit® MF-319 developer for 15 - 20sec (or as soon as pattern is visible.) (Mild agitation required.)
    - IMMEDIATELY remove and rinse in DI water.
    - Dry with N_2

13) **Contact pad deposition – E-beam:** to deposit contact pad metal.
    - 100nm Ti → 300nm Au
    - Strip photoresist with excess metal using acetone and ultrasonic bath for ~15min
    - Clean: Acetone → Methanol → DI Water → N_2
    - Check thickness of metal thickness using profilometer

14) **Contact pad anneal – RTA:** Recipe - GANSC_P
    - Anneal temperature: 500°C
    - Anneal time: 1 minutes
    - Anneal ambient: N_2

BIBLIOGRAPHY

[1] R. Alley et al., "Climate Change 2007: The Physical Science Basis Summary for Policymakers," Contribution of Working Group I to the Fourth Assessment Report of the Intergovernmental Panel on Climate Change, Paris, February 2007.

[2] "Global Warming, the Ozone Layer, and Acid Rain," an original document written by the West Wales ECO Center, 2006 (URL: http://www.ecocentre.org.uk/global-warming.html).

[3] J. H. Wood, G. R. Long, D. F. Morehouse, "Long-Term World Oil Supply Scenarios," from archives of the Energy Information Administration (EIA), August 2004 (URL: http://tonto.eia.doe.gov/FTPROOT/petroleum/itwos04.pdf).

[4] J. Goldemberg, T. B. Johansson, World Energy Assessment Overview, 2004 Update, (United Nations Development Programme, New York, 2004) (URL: www.undp.org/energy/weaover2004.htm).

[5] MarketbuzzTM 2007: Annual World Solar Photovoltaic Industry Report, March 19, 2007 (URL: http://www.solarbuzz.com/Marketbuzz2007-intro.htm).

[6] Basic Research Needs for Solar Energy Utilization (U.S. Department of Energy, Washington, DC, 2005) (URL: www.er.doe.gov/bes/reports/abstracts.html#SEU).

[7] REN21, "Renewables Global Status Report 2006 Update" (Paris: REN21 Secretariat and Washington, DC:Worldwatch Institute), 2006 (URL: http://www.ren21.net/globalstatusreport/download/RE_GSR_2006_Update.pdf).

[8] A survey by Solarbuzz LLC based on around 80-90 companies retailing solar electric products compared with US Government Statistics on US Electric Utility average Revenue per Kilowatt hour by Sector, October 2007 (URL: http://www.solarbuzz.com/SolarPrices.htm).

[9] Martin A. Green, "Third Generation Photovoltaics: Advanced Solar Electricity Generation," (Springer-Verlag, Berlin, 2003).

[10] L. Kazmerski, K. Zweibel, "Best Research Cell Efficiencies," National Renewable Energy Laboratory information database, July 2005 (URL: http://www.nrel.gov/pv/thin_film/docs/bestresearchcellefficienciesall.ppt).

[11] R. R. King, D. C. Law, K. M. Edmondson, C. M. Fetzer, G. S. Kinsey, H. Yoon, R. A. Sherif, N. H. Karam, "40% efficient metamorphic GaInP/GaInAs/Ge multijunction solar cells," Appl. Phys. Lett., vol. 90, p. 183516, 2007.

[12] R. R. King, R. A. Sherif, D. C. Law, J. T. Yen, M. Haddad, Z. M. Fetzer, K. M. Edmondson, G. S. Kinsey, H. Yoon, M. Joshi, S. Mesropian, H. L. Cotal, D. D. Krut, J. H. Ermer, N. H. Karam, "New horizons in III-V multijunction terrestrial concentrator cell research," Proc. of 21st European PV Solar Energy Conference, Dresden, Germany, September 2006.

[13] A. Barnett, D. Kirkpatrick, C. Honsberg, D. Moore, M. Wanlass, K. Emery, R. Schwartz, D. Carlson, S. Bowden, D. Aiken, A. Gray, S. Kurtz, L. Kazmerski, T. Moriarty, M. Steiner, J. Gray, T. Davenport, R. Buelow, L. Takacs, N. Shatz, J. Bortz, O. Jani, K. Goossen, F. Kiamilev, A. Doolittle, I. Ferguson, B. Unger, G. Schmidt, E. Christensen, D. Salzman, "Milestones toward 50% efficient solar cell modules," Proc. of 22nd European PV Solar Energy Conference, Milan, Italy, September 2007.

[14] F. Bernardini, and V. Fiorentini, "Nonlinear Macroscopic Polarization in III-V Nitride Alloys", Phys. Rev. B, 64, 8 (2001), p. 085207/1.

[15] V. Fiorentini F. Bernardini, "Spontaneous versus Piezoelectric Polarization in III-V Nitrides: Conceptual Aspects and Practical Consequences", Phys. Stat. Sol. B, 216 (1999), p. 391.

[16] I. Ho, and G. B. Stringfellow, "Solid phase Immiscibility in GaInN," Appl. Phys. Lett., vol. 69, p. 2701, 1996.

[17] S. Chichibu, T. Azuhata, T. Sota, and S. Nakamura, "Luminescence from Localized States in InGaN Epilayers," Appl. Phys. Lett., vol. 70, p. 2822, 1997.

[18] J.-K. Ho, C.-S. Jong, C. C. Chiu, C.-N. Huang, K.-K. Shih, L.-C. Chen, F.-R. Chen, J.-J. Kai "Low-resistance Ohmic contacts to p-type GaN achieved by the oxidation of Ni/Au films," J. Appl. Phys., vol. 86, n. 8, p. 4491 (1999).

[19] H. W. Jang, S. Y. Kim, J.-L. Lee, "Mechanism for Ohmic contact formation of oxidized Ni/Au on p-type GaN," J. Appl. Phys., vol. 94, p. 1748, 2003.

[20] P. A. Basore and D. A. Clugston, PC1D Version 5.9, Sydney, Australia: Univ. of New South Wales, 2003.

[21] SiLENSe 3.42 (Simulator of Light Emitters based on Nitride Semiconductors), Semiconductor Technology Research, Inc., Richmond, VA, USA (URL: http://www.semitech.us/products/SiLENSe/).

[22] H. P. Maruska, and J. J. Tietjen, "The preparation and properties of vapor-deposited single-crystal-line GaN," Appl. Phys. Lett., vol. 15, p. 327, 1969.

[23] P. Perlin, T. Suski, H. Teisseyre, M. Leszczynski, I. Grzegory, J. Jun, S. Porowski, P. Bogusławski, J. Bernholc, J. C. Chervin, A. Polian, and T. D. Moustakas, " Towards the identification of the dominant donor in GaN," Phys. Rev. Lett., vol. 75, p. 296, 1995.

[24] H. Morkoç, S. Strite, G. B. Gao, M. E. Lin, B. Sverdlov, and M. Burns, J. Appl. Phys., vol. 76, p. 1363, 1994.

[25] S. C. Jain, M. Willander, J. narayan, and R. Van Overstraeten, J. Appl. Phys., vol. 87, p. 965, 2000.

[26] S. J. Pearton, J. C. Zolper, R. J. Shul, and F. Ren, J. Appl. Phys., vol. 86, p. 1, 1999.

[27] F. A. Ponce, B. S. Krusor, J. S. Major, Jr., W. E. Plano, and D. F. Welch, Appl. Phys. Lett., vol. 67, p. 410, 1995.

[28] S. Nakamura, S. Pearton and G. Fasol, "The blue laser diode, 2 ed.," (Springer-Verlag, Berlin, 2000).

[29] W. Shockley, H. Queisser, "Detailed Balance Limit of Efficiency of p-n Junction Solar Cells," J. Appl. Phys., vol. 32, 3, p. 510, 1961.

[30] Devos, "Endoreversible Thermodynamics of Solar Energy Conversion," (Oxford University Press, Oxford, 1990).

[31] Martí, G. L. Araújo, "Limiting Efficiencies for Photovoltaic Energy Conversions in Multigap Systems," Solar Energy Materials and Solar Cells, vol. 43, p. 203, 1996.

[32] J. Zhao, A. Wang, M. A. Green, F. Ferrazza, "Novel 19.8% Efficient 'Honeycomb' Textured Multicrystalline and 24.4% Monocrystalline Silicon Solar Cells," Appl. Phys. Lett., vol. 73, p. 1991–1993, 1998.

[33] M. A. Green, "Solar Cells: Operating Principles, Technology and System Applications," (UNSW, Sydney, 1998).

[34] C. B. Honsberg, J. E. Cotter, K. R. McIntosh, S. C. Pritchard, B. S. Richards, S. R. Wenham, "Design Strategies for Commercial Solar Cells using the Buried Contact Technology," IEEE Transactions Electron. Dev., vol. 46, p. 1984, 1999.

[35] E. D. Jackson, "Areas for Improvement of the Semiconductor Solar Energy Conductor," Transactions of the Conference on Use of Solar Energy – The Scientific Base, vol. 5, p. 122, 1955.

[36] E. D. Jackson, US Patent 2,949,498, August 16, 1960.

[37] K.W.J. Barnham, G. Duggan, "A new approach to high-efficiency multi-band-gap solar cells," J. Appl. Phys., 67 (1990), p. 3490.

[38] K. Barnham, B. Braun, J. Nelson, M. Paxman, C. Button, J. Roberts, and C. Foxon, "Short-circuit Current and Energy Efficiency Enhancement in a Low-dimension Structure Photovoltaic Device," Appl. Phys. Lett., vol. 59, p. 135, 1991.

[39] A. Luque, and A. Marti, "Increasing the Efficiency of Ideal Solar Cells by Photon Induced Transitions at Intermediate Levels," Phys. Rev. Lett., vol. 78, p. 5014, 1997.

[40] R. T. Ross, and A. J. Nozik, "Efficiency of Hot-carrier Solar Energy Converters," J. Appl. Phys., vol. 53, p. 3813, 1982.

[41] R. D. Schaller and V. I. Klimov, "High Efficiency Carrier Multiplication in PbSe Nanocrystals: Implications for Solar Energy Conversion", Phys. Rev. Lett., vol. 92, p. 186601, 2001.

[42] R. J. Ellingson, M. C. Beard, J. C. Johnson, P. Yu, O. I. Micic, A.. J. Nozik, A. Shabaev and A. L. Efros, "Highly Efficient Multiple Exciton Generation in Colloidal PbSe and PbS Quantum Dots", Nano. Lett. vol. 5, p. 865, 2005.

[43] C. Honsberg, O. Jani, A. Doolittle, E. Trybus, G. Namkoong, I. Ferguson, D. Nicol, and A. Payne, "InGaN – A New Solar Cell Material," Proceedings of the 19th European Photovoltaic Science and Engineering Conference, Paris, France, June 7-11, 2004, p. 15-20.

[44] R. P. Gale, R. W. McClelland, D. B. Dingle, J. V. Gormley, R. M. Burgess, N. P. Kim, R. A. Mickelsen, B. F. Stanbery, "High-Efficiency GaAs/CuInSe2 and AlGaAs/CuInSe2 Thin-Film Tandem Solar Cells," Proc. 21st IEEE Photovoltaic Specialists Conf., Kissimimee, May 1990; p. 53–57.

[45] V. Yu. Davydov, A. A. Klochikhin, R. P. Seisyan, V. V. Emtsev, S. V. Ivanov, F. Bechstedt, J. Furthmuller, H. Harima, A. V. Mudryi, J. Aderhold, O. Semchinova, J. Graul, "Absorption and Emission of Hexagonal InN. Evidence of Narrow Fundamental Band Gap," Phys. Stat. Sol. B, vol. 229, 3, p. R1-R3, 2002.

[46] T. Matsuoka, H. Okamoto, M. Nakao, H. Harima, and E. Kurimoto, "Optical Bandgap Energy of Wurtzite InN", Appl. Phys. Lett., 81, 7, p. 1246-1248, 2002.

[47] J. Wu et al., "Temperature Dependence of the Fundamental Band Gap of InN", J. Appl. Phys., vol. 94, 7, p. 4457-4460, 2003.

[48] Y. Nanishi, Y. Saito and T. Yamaguchi, "R-F Molecular Beam Epitaxy Growth and Properties of InN and Related Alloys", Jpn. J. Appl. Phys., vol. 42, 5A, p. 2549-2559, 2003.

[49] L.E. Shilkrot, D.J. Srolovitz, J. Tersoff, Phys. Rev. B, vol. 62, p. 8397, 2000.

[50] A. A. Chernov, Modern Crystallography III, Crystal Growth (Springer-Verlag, Berlin, Heidelberg, New York, Tokyo, 1984), Chapters 1, 2.

[51] T. V. Shubina, S. V. Ivanov, V. N. Jmerik, D. D. Solnyshkov, V. A. Vekshin, P. S. Kop'ev, "Mie resonances, infrared emission, and the band gap of InN," Phys. Rev. Lett., vol. 92, p. 117407, 2004.

[52] A. G. Bhuiyan, K. Sugita, K. Kasashima, A. Hashimoto, A. Yamamoto, V. Y. Davydov, "Single-crystalline InN films with an absorption edge between 0.7 and 2 eV grown using different techniques and evidence of the actual band gap energy," Appl. Phys. Lett., vol. 83, p. 4788, 2003.

[53] V. A. Elyukhin, S. A. Nikishin, "Internal Strain Energy of AX3B1-X3N Ternary Solid Solutions of Cubic Modification," Semicond. Sci. Technol., vol. 11, p. 917-920, 1996.

[54] I. H. Ho, G. B. Stringfellow, "Incomplete Solubility in Nitride Alloys," Mater. Res. Soc. Symp. Proc., vol. 449, p. 871-880, 1997.

[55] S. Strite, and H. Morkoç, "GaN, AlN, and InN: A Review," J. Vac. Sci. Technol. B, vol. 10, p. 1237, 1992.

[56] S. Yamasaki, A. Asami, N. Shibata, M. Koike, K. Manabe, T. Tanaka, H. Amano, and I. Akasaki, "P-type conduction in Mg-doped Ga0.91In0.09N grown by metalorganic vapor phase epitaxy," Appl. Phys. Lett., vol. 66, p. 1112, 1995.

[57] K. Kumakura, T. Makimoto, N. Kobayashi, "Activation energy and electrical activity of Mg in Mg-doped InxGa¬1-xN (x < 0.2)," Jpn. J. Appl. Phys., vol. 39, p. L337, 2000.

[58] T. C. Wen, W. I. Lee, J. K. Sheu, G. C. Chi, "Characterization of p-type InxGa1-xN grown by metalorganic chemical vapor deposition," Solid State Elect., vol. 45, p. 427, 2001.

[59] K. Kumakura, T. Makimoto, and N. Kobayashi, "High hole concentrations in Mg-doped InGaN grown by MOVPE," J. Cryst. Growth, vol. 221, p. 267, 2000.

[60] T. Mori, T. Kozawa, T. Ohwaki, Y. Taga, S. Nagai, S. Yamasaki, S.Asami, N. Shibata, and M. Koike, "Schottky barriers and contact resistances on p-type GaN," Appl. Phys. Lett., vol. 69, p. 3537, 1996.

[61] L. L. Smith, R. F. Davis, M. J. Kim, R. W. Carpenter, and Y. Huang, "Microstructure, electrical properties, and thermal stability of Au-based Ohmic contacts to p-GaN," J. Mater. Res., vol. 12, p. 2249, 1997.

[62] K. V. Vassilevski, M. G. Rastegaeva, A. I. Babanin, I. P. Nikitina, and V. A. Dmitriev, "Ti/Ni Ohmic contacts to n-type GaN," Mater. Sci. Eng. B, vol. B43, p. 292, 1997.

[63] Y. Yamaoka, Y. Kaneko, S. Nakagawa, and N. Yamada, "Low resistance Ohmic contacts to p-type GaN," Proceedings of the Second International Conference on Nitride Semiconductors, Tokushima, Japan, 27–31 October 1997, p. P1–19.

[64] D. J. King, L. Zhang, J. C. Ramer, S. D. Hersee, and L. F. Lester, "Temperature behavior of Pt/Au Ohmic contacts to p-GaN," Mater. Res. Soc. Symp. Proc., vol. 468, p. 421, 1997.

[65] T. Kim, J. Khim, S. Chae, and T. Kim, "Low resistance contacts to p-type GaN," Mater. Res. Soc. Symp. Proc., vol. 468, p. 427, 1997.

[66] J. T. Trexler, S. J. Pearton, P. H. Holloway, M. G. Mier, K. R. Evans, and R. F. Karlicek, "Comparison of Ni/Au, Pd/Au, and Cr/Au metallizations for Ohmic contacts to p-GaN," Mater. Res. Soc. Symp. Proc. 449, 1091 (1997).

[67] J. K. Kim, J.-L. Lee, J. W. Lee, H. E. Shin, Y. J. Park, and T. Kim, "Low resistance Pd/Au Ohmic contacts to p-type GaN using surface treatment," Appl. Phys. Lett., vol. 73, p. 2953, 1998.

[68] T. Kim, M. C. Yoo, and T. Kim, "Cr/Ni/Au Ohmic contacts to the moderately doped p-and n-GaN," Mater. Res. Soc. Symp. Proc. 449, 1061 (1997).

[69] J.-S. Jang, H.-G. Kim, K.-H. Park, C.-S. Um, I.-K. Han, S.-H. Kim, H.-K. Jang, and S.-J. Park, Mater. Res. Soc. Symp. Proc. 482, 1053 (1998).

[70] J.-S. Jang, I.-S. Chang, T.-Y. Seong, and S.-J. Park, Proceedings of the Second International Symposium on Blue Laser and Light Emitting Diodes, Chiba, Japan, 29 September–2 October 1998, p. Tu-P33.

[71] J.-S. Jang, I.-S. Chang, H.-K. Kim, T.-Y. Seong, S. Lee, and S.-J. Park, "Low-resistance Pt/Ni/Au Ohmic contacts to p-type GaN," Appl. Phys. Lett. 74, 70 (1999).

[72] J. K. Kim, J.-L. Lee, J. W. Lee, H. E. Shin, Y. J. Park, and T. Kim, "Low resistance Pd/Au Ohmic contacts to p-type GaN using surface treatment," Appl. Phys. Lett., vol. 73, p. 2953, 1998.

[73] J.-S. Jang, S.-J. Park, T.-Y. Seong, "Formation of low resistance Pt Ohmic contacts to p-type GaN using two-step surface treatment," J. Vac. Sci. Technol. B, vol. 17, p. 2667, 1999.

[74] T. Margalith, O. Buchinsky, D. A. Cohen, A. C. Abare, M. Hansen, S. P. DenBaars, L. A. Coldren, "Indium tin oxide contacts to gallium nitride optoelectronic devices," Appl. Phys. Lett., vol. 74, p. 3930, 1999.

[75] Y. C. Lin, S. J.Chang, Y. K. Su, T. Y. Tsai, C. S. Chang, S. C. Shei, C. W. Kuo, S. C. Chen, "InGaN/GaN light emitting diodes with Ni/Au, Ni/ITO and ITO p-type contacts," Solid-State Electronics, vol. 47, p. 849, 2003.

[76] M. E. Lin, F. Y. Huang, and H. Morkoç, "Nonalloyed Ohmic Contacts on GaN using InN/GaN Short-Period Superlattices," Appl. Phys. Lett., vol. 64, p. 2557, 1997.

[77] J. K. Sheu, J. M. Tsai, S. C. shei, W. C. Lai, T. C. Wen,C. H. Kou, Y. K. Su, S. H. chang, G. C. Chi, "Low operation voltage of InGaN/GaN light-emitting diodes with Si-doped In[0.3]Ga[0.7]N/GaN short period superlattice tunneling contact layer," IEEE Electron. Dev. Lett., vol. 22, p. 460, 2001.

[78] Y.-L. Li, E. F. Schubert, J. W. Graff, A. Osinsky, W. F. Schaff, "Low-resistance Ohmic contacts to p-type GaN," Appl. Phys. Lett., vol. 76, p. 2728, 2000.

[79] M. Z. Shvarts, O. I. Chosta, I. V. Kochnev, V. M. Lantratov, and V. M. Andreev, "Radiation resistant AlGaAs/GaAs concentrator solar cells with internal Bragg reflector," Sol. Energy Mater. Sol. Cells, vol. 68, p. 105, 2001.

[80] D. C. Johnson, I. Ballard, K.W. J. Barnham, D. B. Bishnell, J. P. Connolly, M. C. Lynch, T. N. D. Tibbits, N. J. Ekins-Daukes, M. Mazzer, R. Airey, G. Hill, and J. S. Roberts, "Advances in Bragg stack quantum well solar cells," Sol. Energy Mater. Sol. Cells, vol. 87, p. 169, 2005.

[81] D.-X. Wang, I. T. Ferguson, J. A. Buck, "GaN-based distributed Bragg reflector for high-brightness LED and solid-state lighting," Applied Optics, vol. 46, p. 4763, 2007.

[82] G. E. Jellison, Jr., F. A. Modine, P. Doshi, A. Rohatgi, "Spectroscopic ellipsometry characterization of thin-film silicon nitride," Thin Solid Films, vol. 313-314, p. 193, 1988.

[83] S. R. Chitre, "A high volume cost efficient production macrostructuring process," Proc. 13th IEEE Photovoltaic Specialists Conf., Washington, D.C., June 1978, p. 152-154.

[84] H. B. Serreze, "Optimizing solar cell performance by simultaneous consideration of grid pattern design and interconnect configurations," Proc. 13th IEEE Photovoltaic Specialists Conf., Washington, D.C., June 1978, p. 609-614.

[85] A. Flat, and A. G. Milnes, "Optimization of multi-layer front contact grid patterns for soar cells," Solar Energy, vol. 23, p. 289, 1979.

[86] H. Mäckel, and R. Lüdermann, "Detailed study of the composition of hydrogenated SiN_X layers for high-quality silicon surface passivation, J. Appl. Phys., vol. 92, p. 2602, 2002.

[87] J.-S. Jang, S.-J. Park, and T.-Y. Seong, "Effects of surface treatment on the electrical properties of Ohmic contacts to (In)GaN for high performance optical devices," Phys. Stat. Sol. (a), vol. 194, p. 576, 2002.

[88] O. von Roos, "A simple theory of back surface field (BSF) solar cells," J. Appl. Phys., vol. 49, p. 3503, 1978.

[89] B. L. Sopori, K. M. Johes, X. Deng, R. Matson, M. Al-Jassim, S. Tsuo, A. Doolittle, A. Rohatgi, "Hydrogen in silicon: diffusion and defect passivation," Proc. 22nd IEEE Photovoltaic Specialists Conf., Las Vegas, NV, October 1991, p. 833-841.

[90] Z. Yang, Z. Xu, "A theoretical study of electronic and optical properties in wurtzite GaN," J. Phys.: Condens. Matter, vol. 8, p. 8303, 1996.

[91] J. F. Muth, J. H. Lee, I. K. Shmagin, R. M. Kolbas, H. C. Casey, Jr., B. P. Keller, U. K. Misra, S. P. DenBaars, "Absorption coefficient, energy gap, exciton binding energy, and recombination lifetime of GaN obtained from transmission measurements," Appl. Phys. Lett., vol. 71, p. 2572, 1997.

[92] G. Yu, G. Wang, H. Ishikawa, M. Umeno, T. Egawa, J. Watanabe, T. Jimbo, "Optical properties of wurtzite structure GaN on sapphire around fundamental absorption edge (0.87-4.77 eV) by spectroscopic ellipsometry and the optical transmission method," Appl. Phys. Lett, vol. 70, p. 3209, 1997.

[93] Z. Z. Bandic, P. M. Bridger, E. C. Piquette and T. C. McGill, "Minority Carrier Diffusion Length and Lifetime in GaN", Appl. Phys. Lett., vol. 72, 24, p. 3166, 1998.

[94] M. E. Levinshtein, S. L. Rumyanstev and M. S. Shur, "Properties of Advanced Semiconductor Materials: GaN, AlN, InN, BN, SiC, SiGe", John Wiley & Sons, Inc., New York, 2001.

[95] D. T. Rover, P. A. Basore, G. M. Thorson, "Solar cell modeling on personal computers," Proc. 18th IEEE PV Specialist Conf., Las Vegas, NV, October 1985, p. 703.

[96] R. D. King-Smith, D. Vanderbilt, "Theory of polarization of crystalline solids," Phys. Rev. B, vol. 47, p. 1651, 1993.

[97] R. Resta, "Macroscopic polarization in crystalline dielectrics: the geometric phase approach," Rev. Mod. Phys., vol. 66, p. 899, 1994.

[98] F. Bernardini, V. Fiorentini, D. Vanderbilt, "Spontaneous polarization and piezoelectric constants of III-V nitrides," Phys. Rev. B, vol. 56, p. R10 024, 1997.

[99] H. Morkoç, R. Cingolani, and B. Gill, "Polarization effects in nitride semiconductors and device structures," Mat. Res. Innovat., vol. 3, p. 97, 1999.

[100] O. Ambacher, R. Dimitrov, M. Stutzmann, B. E. Foutz, M. J. Murphy, J. A. Smart, J. R. Shealy, N. G. Weimann, K. Chu, M. Chumbes, B. Green, A. J. Sierakowski, W. J. Schaff, L. F. Eastman, "Role of spontaneous and piezoelectric polarization induced effects in group-III nitride based heterostructures and devices," Phys. Stat. Sol. B, vol. 216, p. 381, 1999.

[101] F. D. Sala, A. Di Carlo, P. Lugli, F. Bernardini, V. Fiorentini, R. Scholz, "Free-carrier screening of polarization fields in wurtzite GaN/InGaN laser structures," Appl. Phys. Lett., vol. 74, p. 2002, 1999.

[102] P. Lefebvre, A. Morel, M. Gallart, T. Taliercio, J. Allègre, B. Gil, H. Mathieu, B. Damilano, N. Grandjean, J. Massies, "High internal electric field in a graded-width InGaN/GaN quantum well: Accurate determination by time-resolved photoluminescence spectroscopy," Appl. Phys. Lett., vol. 78, p. 1252, 2001.

[103] R. Langer, J. Simon, V. Ortiz, N. T. Pelekanos, A. Barski, R. André, M. Godlewski, "Giant electric fields in unstrained GaN single quantum well," Appl. Phys. Lett., vol. 74, p. 3827, 1999.

[104] F. Bernardini, V. Fiorentini, "Polarization fields in nitride nanostructures: 10 points to think about," App. Surface Science, vol. 166, p. 23, 2000.

[105] J. C. Freeman, "Basic equations for the modeling of Gallium Nitride (GaN) High Electron Mobility Transistors (HEMT)," NASA/TM – 2003-211983.

[106] O. Ambacher, J. Smart, J. R. Shealy, N. G. Weimann, K. Chu, M. Murphy,W. J. Schaff, L. F. Eastman, R. Dimitrov, L. Wittmer, M. Stutzmann, W.Rieger, and J. Hilsnbeck, "Two-dimensional electron gases induced by spontaneous and piezoelectric polarization charges in N- and Ga-face AlGaN/GaN heterostructures," J. Appl. Phys. 85 (1999), p. 3222.

[107] O. Ambacher, J. Majewski, C. Miskys, A. Link, M. Hermann, M. Eickhoff, M. Stutzmann, F. Bernerdini, V. Fiorentini, V. Tilak, B. Schaff, L. F. Eastman, "Pyroelectric properties of Al(In)GaN/GaN hetero- and quantum well structures," J. Phys.: Condens. Matter, vol. 14, p. 3399, 2002.

[108] C. Mattiussi, "The finite volume, finite element, and finite difference methods as numerical methods for physical field problems," Advances in Imaging and Electron Physics, vol. 113, p. 1, 2000.

[109] C. T. Kelly, "Solving nonlinear equations with Newton's method," Society for Industrial and Applied Mathematics (SIAM), Philadelphia, 2003.

[110] M. A. Green, "Silicon solar cells: Advance principles and practices," (Bridge, Sydney, 1995).

[111] G. S. Kamath, J. Ewan, R. C. Knechtli, "Large-area high-efficiency (AlGa)As – GaAs solar cells," IEEE Trans. Electron. Dev., vol. 24, p. 473, 1977.

[112] H. Lu, M. Thothathiri, Z. Wu, and I. Bhat, "Study of indium droplets formation on the InxGa1-x films by single crystal X-ray diffraction," J. Electron. Mater., vol. 26, p. 281, 1997.

[113] S. Nakamura, "Growth of InxGa1-xN Compound Semiconductors and High-Power InGaN/AlGaN Double Heterostructure Violet-Light-Emitting Diodes," Micr. J., vol. 25, p. 651, 1994.

[114] H. C. Casey Jr., D. d. Sell, and K. W. Wecht, "Concentration dependence of the absorption coefficient for n- and p-type GaAs between 1.3 and 1.6 eV," J. Appl. Phys., vol. 46, p. 250, 1975.

[115] E. D. Palik, "Handbook of optical constants of solids," Academic press, San Diego, 1985.

[116] Y. Nakano, and T. Jimbo, "Electrical characterization of acceptor levels in Mg-doped GaN," J. Appl. Phys., vol. 92, p. 5590, 2002.

[117] S. Yamasaki, S. Asami, N. shibata, M. Koike, K. Manabe, T. Tanaka, H. Amano, and I. Akasaki, "p-type conduction in Mg-doped Ga0.91In0.09N grown by metalorganic vapor-phase epitaxy," Appl. Phys. Lett., vol. 66, p. 1112, 1995.

[118] M. D. Lammert, and R. H. Schwartz, "The interdigitated back contact solar cell: A silicon solar cell for use in concentrated sunlight," IEEE Trans. Electron Dev., vol. 24, p. 337, 1977.

[119] J. –S. Jang, S. –J. Park, and T. –Y. Seong, "Effects of surface treatment on the electrical properties of Ohmic contacts to (In)GaN for high performance optical devices," Phys. Stat. Sol. (a), vol. 194, p. 576, 2002.

[120] F. González-Posada, J. A. Bardwell, S. Moisa, S. Haffouz, H. Tang, A. F. Brana, and E. Muñoz, "Surface cleaning and preparation in AlGaN/GaN-based HEMT processing as assessed by X-ray photoelectron spectroscopy," Appl. Surface Sci., vol. 253, p. 6185, 2007.

[121] D.-F. Wang, F. Shiwei, C. Lu, A. Motayed, M. Jah, S. N. Mohammad, K. A. Johes, and L. Salamanco-Riba, "Low-resistance Ti/Al/Ti/Au multilayer Ohmic contact to n-GaN," J. Appl. Phys., vol. 89, p. 6214, 2001.

[122] A. Vertiatchikh, E. Kaminsky, J. Teetsov, K. Robinson, "Structural properties of alloyed Ti/Al/Ti/Au and Ti/Al/Ti/Au ohmic contacts to AlGaN/GaN," Solid State Electron., vol. 50, p. 1425, 2006.

PUBLICATION LIST

[1] **O. Jani**, and C. Honsberg, "Absorption and Transport via Tunneling in Quantum-Well Solar Cells," Proceedings of the 14th International Photovoltaic Science and Engineering Conference, Bangkok, Thailand, Jan 26-30, 2004, p. 119-121.

[2] **Invited:** C. Honsberg, **O. Jani**, A. Doolittle, E. Trybus, G. Namkoong, I. Ferguson, D. Nicol, and A. Payne, "InGaN – A New Solar Cell Material," Proceedings of the 19th European Photovoltaic Science and Engineering Conference, Paris, France, June 7-11, 2004, p. 15-20.

[3] C. Honsberg, **O. Jani**, A. Doolittle, E. Trybus, and I. Ferguson, "InGaN Solar Cells," Proceedings of the US Department of Energy Solar Energy Technologies Program Review, Denver, Colorado, Oct 25-28, 2004, p. 87-88.

[4] **Invited: O. Jani**, C. Honsberg, A. Asghar, D. Nicol, I. Ferguson, A. Doolittle, and S. Kurtz, "Characterization and Analysis of InGaN Photovoltaic Devices," Proceedings of the 31st IEEE Photovoltaic Specialists Conference, Orlando, Florida , Jan 3-7, 2005, p. 37-42.

[5] C. Honsberg, **O. Jani**, E. Trybus, A. Doolittle, and I. Ferguson, "Novel High-Efficiency PV Devices based on III-V Nitride Material System," Proceedings of the US Department of Energy Solar Energy Technologies Program Review, Denver, Colorado, Nov 7-10, 2005.

[6] **Invited: O. Jani**, C. Honsberg, Y. Huang, J. O. Song, I. Ferguson, G. Namkoong, E. Trybus, A. Doolittle, and S. Kurtz, "Design, Growth, Fabrication and Characterization of High-Band Gap InGaN/GaN Solar Cells," Proceedings of the 4th IEEE World Conference on Photovoltaic Energy Conversion, Waikoloa, Hawaii, May 7-12, 2006.

[7] N. Faleev, C. Honsberg, **O. Jani**, and I. Ferguson, "Crystalline Perfection of AlN and GaN Epitaxial Layers and the Main Features of Structural Transformation of Crystalline Defects," Proceedings of the 1st International Symposium for Growth of III-Nitrides, Linköping, Sweden, June 4-7, 2006.

[8] **O. Jani**, and C. Honsberg, "Absorption and Transport via Tunneling in Quantum-Well Solar Cells," Solar Energy Materials and Solar Cells, vol. 90, p. 3464 – 3470, 2006.

[9] N. Faleev, C. Honsberg, **O. Jani**, and I. Ferguson, "Crystalline perfection of GaN and AlN epitaxial layers and the main features of structural transformation of crystalline defects," Journal of Crystal Growth, vol. 300, p. 246 – 250, 2007.

[10] **O. Jani**, I. Ferguson, C. Honsberg, and S. Kurtz, "Design and Characterization of GaN/InGaN Solar Cells," Applied Physics Letters, vol. 91, p. 132117, 2007.

[11] Yong Huang, **Omkar Jani**, Eun Hyun Park, and Ian Ferguson, "Influence of growth conditions on phase separation of InGaN bulk material grown by MOCVD," Proceedings of the Material Research Society Symposium, p. 0955-I07-20, 2007.

[12] **O. Jani**, H. Yu, E. Trybus, B. Jampana, I. Ferguson, A. Doolittle, and C. Honsberg, "Effect of phase separation on performance of III-V nitride solar cells," Proceedings of the 22nd European Photovoltaic Solar Energy Conference, Milan, Italy, 3-7 September 2007.

[13] M. Mehta, **O. Jani**, C. Honsberg, B. Jampana, I. Ferguson, and A. Doolittle, "Modifying PC1D to model spontaneous and piezoelectric polarization in III-V nitride solar cells," Proceedings of the 22nd European Photovoltaic Solar Energy Conference, Milan, Italy, 3-7 September 2007.

[14] Allen Barnett, Douglas Kirkpatrick, Christiana Honsberg, Duncan Moore, Mark Wanlass, Keith Emery, Richard Schwartz, Dave Carlson, Stuart Bowden, Dan Aiken, Allen Gray, Sarah Kurtz, Larry Kazmerski, Tom Moriarty, Myles Steiner, Jeffery Gray, Tom Davenport, Roger Buelow, Laszlo Takacs, Narkis Shatz, John Bortz, **Omkar Jani**, Keith Goossen, Fouad Kiamilev, Alan Doolittle, Ian Ferguson, Blair Unger, Greg Schmidt, Eric Christensen, and David Salzman, "Milestones toward 50% efficient solar cell modules, Proceedings of the 22nd European Photovoltaic Solar Energy Conference, Milan, Italy, 3-7 September 2007.

[15] E. Trybus, **O. Jani**, S. Burnham, J. Bai, D. S. Citrin, I. Ferguson, W. A. Doolittle, C. Honsberg and M. Steiner, "Characteristics of InGaN Designed for Photovoltaic Applications", 7th International Conference of Nitride Semiconductors (ICNS-7), Las Vegas, NV, USA, September 16-21, 2007.

[16] Balakrishnam R Jampana, **Omkar K Jani**, Hongbo Yu, Ian T Ferguson, Brian E McCandless, Steven S Hegedus, Robert L Opila and Christiana B Honsberg, "Nitride-based Schottky-barrier photovoltaic devices," Proceedings of the Material Research Society Symposium; to be published.

[17] **O. Jani**, B. Jampana, M. Mehta, H. Yu, I. Ferguson, R. Opila, C. Honsberg, "Optimization of GaN window layer for InGaN solar cells using polarization effects," Submitted to the 33rd IEEE Photovoltaic Specialists Conference, San Diego, California, May 11 – 16, 2008.

[18] N. Faleev, **O. Jani**, A. Pancholi, I. Ferguson, V. Stoleru, C. Honsberg, "High quality InGaN for photovoltaic applications: Type and spatial distribution of crystalline defects and "phase" separation," Submitted to the 33rd IEEE Photovoltaic Specialists Conference, San Diego, California, May 11 – 16, 2008.

[19] **Patent**: The resulting work is an integral part of the USPTO Patent application titled "**High Efficiency Solar Cell**," filed by Allen Barnett et al.

[20] **Patent**: Currently being filed on "**Optimal GaN window layers for InGaN solar cells**."